This document contains the master thesis and the master proposal thesis of Philipp Dijkstal.

Author: Philipp Dijkstal
CERN supervisor: G. Iadarola
Date: September 2016 – October 2017

Electron cloud buildup studies for the LHC

Master-Thesis von Philipp Dijkstal
Tag der Einreichung:

1. Gutachten: Prof. Dr. Oliver Boine-Frankenheim
2. Gutachten: Prof. Dr. Rüdiger Schmidt

TECHNISCHE UNIVERSITÄT DARMSTADT

Fachbereich Physik
Externe Master-Thesis
Institut TEMF / CERN

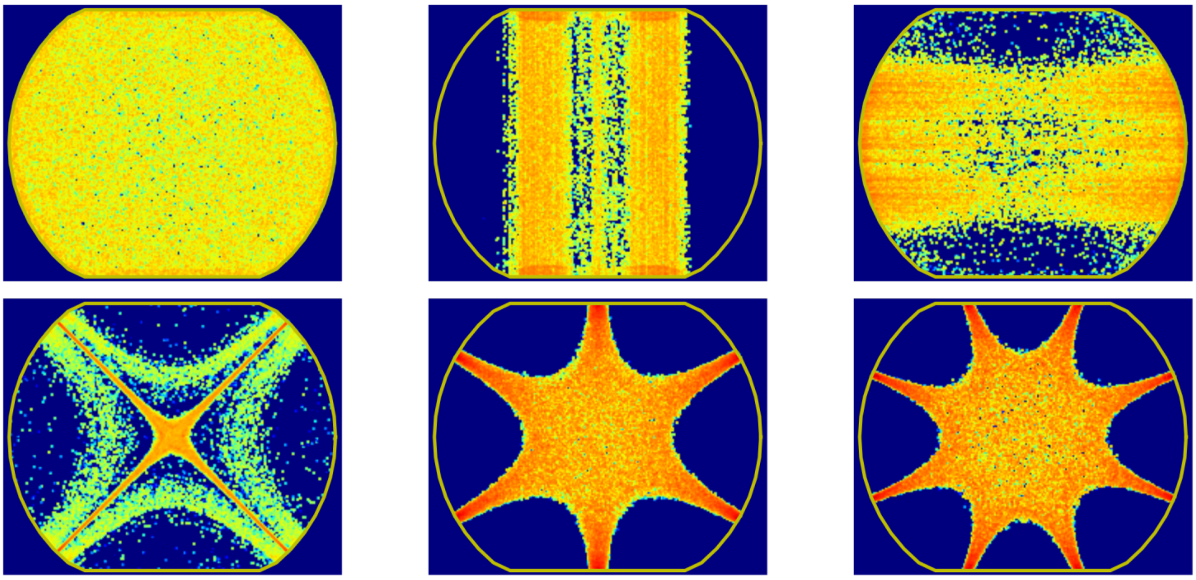

Electron cloud buildup studies for the LHC

Vorgelegte Master-Thesis von Philipp Dijkstal

1. Gutachten: Prof. Dr. Oliver Boine-Frankenheim
2. Gutachten: Prof. Dr. Rüdiger Schmidt

Tag der Einreichung:

Erklärung zur Master-Thesis

Hiermit versichere ich, die vorliegende Master-Thesis ohne Hilfe Dritter nur mit den angegebenen Quellen und Hilfsmitteln angefertigt zu haben. Alle Stellen, die aus Quellen entnommen wurden, sind als solche kenntlich gemacht. Diese Arbeit hat in gleicher oder ähnlicher Form noch keiner Prüfungsbehörde vorgelegen.

Darmstadt, den October 16, 2017

(Philipp Dijkstal)

Abstract

Electron clouds can develop in accelerators operating with positively charged particles. The consequences of e-cloud related effects are very important for the operation of the Large Hadron Collider (LHC) at CERN, and for the design of future accelerators including the LHC luminosity upgrade (HL-LHC). High electron densities are generated by an interaction between the beam and the confining chamber. Primary electrons, that can be generated through various mechanisms, are accelerated by the beam and impinge on the chamber walls, thereby extracting more electrons from the material. Furthermore they also deposit their kinetic energy in the process, which has to be compensated by the cooling system. Especially in cryogenic environments, as it is the case for a large part of the LHC, high heat loads can pose a serious problem. In order to improve the understanding of the electron cloud, simulation studies are performed with the code PyECLOUD, developed at CERN.

The work of the first half of the project is described in the master proposal thesis. Among other tasks, a recomputation of measured heat loads at the LHC was performed for all fills and all cryogenic cells at the LHC since 2015. Higher order magnets, such as sextupoles and octupoles, are part of every cryogenic cell at the LHC. However it has not been possible to model higher order magnetic fields within PyECLOUD prior to this work. Consequently, the software has been extended and simulations of sextupoles and octupoles were performed for the first time. The results are thoroughly compared to those from quadrupole simulations. Similar properties of the e-cloud in sextupoles and quadrupoles can be observed. The modelled electron cloud in the octupoles turned out to be less strong.

Furthermore, the modelling of build-up simulations with photoelectron seeding has been studied. Results from laboratory measurements of LHC beam screen surface materials are available. The literature has been reviewed and two sets of simulation input parameters were obtained. One set is a conservative estimate, where high photoelectron yields per photon are assumed, corresponding to measurements published for clean, "as-received" samples of copper. The other is a more realistic estimate, taking into account the conditioning of the chamber surfaces by continuous synchrotron radiation from the beam. Simulation results for drift spaces and dipolar magnetic fields are very sensitive to the photoemission parameters. Quadrupoles and higher order magnets on the other hand are barely affected by the presence of photoelectrons. Finally, the modelling of photoemission seeding in PyECLOUD has been extended to study the effects of a delayed time structure of photoelectron generation, of different initial photoelectron energy spectra and of modified spatial distributions of emitted photoelectrons.

Contents

The electron cloud studies that are presented in this report were applied to the Large Hadron Collider (LHC). The layout, basic modes of operation, and the long-term schedule are briefly outlined. The recalculation of measured electron cloud induced heat loads on the LHC beam screens was a major part of the master thesis proposal that precedes this report [1], and is recapitulated here. The concept of the modeling of electron cloud is introduced, and the simulation software PyECLOUD is described.

1.1 The Large Hadron Collider (LHC)

The Large Hadron Collider (LHC) is capable of accelerating two counter-rotating beams of protons or lead ions. These are collided head-on at four points in the ring, where each event produces various decay products that can be identified in surrounding detectors. This data is used to verify or eliminate fundamental physical theories. One example is the Higgs boson, an elementary particle whose existence could be confirmed in 2012 from data collected at the CMS and ATLAS detectors [2, 3].

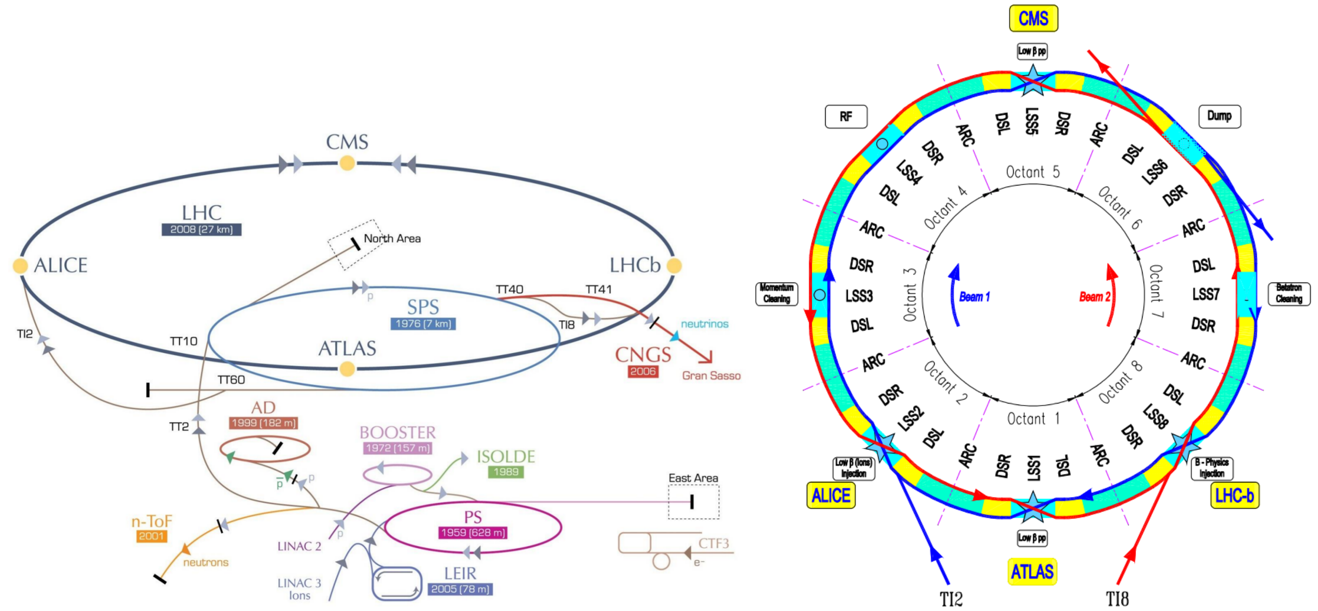

Figure 1.1: Left: the accelerator complex at CERN including some signature experiments and detectors [4]. Right: the basic layout of the LHC [5].

The layout of the LHC is shown in Fig. 1.1 (right), its circumference is about 26.7 km. The machine is divided in eight octants, each containing a long straight section (LSS), two dispersion suppressor (DS) sections and two half arcs. Due to the high beam rigidity, the main magnets of the LHC are superconducting which allows for vastly increased field strengths compared to conventional magnets. The combined length of the dipoles uses about 65% of the total machine circumference [5, 6].

The LHC is supplied with protons by a chain of injectors that consists of Linac 2, the Booster, the Proton Synchrotron (PS) and the Super Proton-Synchrotron (SPS) (see Fig. 1.1 left). If lead ions are accelerated instead, they take a different path where Linac 2 and the Booster are replaced by Linac 3 and the Low Energy Ion Ring (LEIR).

The main phases of a typical fill for proton physics, where beams are put into collision for the LHC experiments, are explained in the following. An overview is provided in Fig. 1.2, where the energy, the total beam intensities, the bunch length and the average heat load on the cryogenic cells of each arc are shown. A proton fill begins right after the previous beam has left the accelerator, meaning that the superconducting magnets have to be ramped down first. Multiple injections of trains from the SPS are necessary to fill the much larger LHC. Afterwards, the machine is ready to ramp the beam energy from injection (450 GeV) to top energy (6.5 TeV). The beam size at the interaction regions in the LHC is decreased (squeezed) to increase the collision rate. The machine parameters are adjusted to optimize the performance, before the

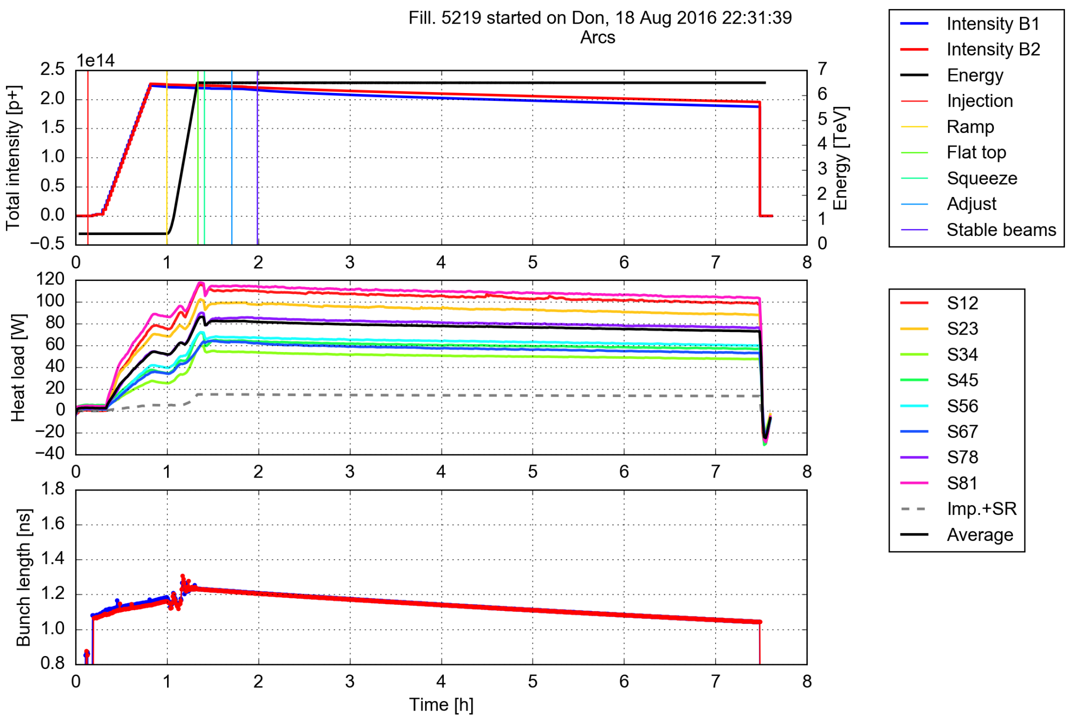

Figure 1.2: In the upper plot, the energy and the total beam intensities are shown during a typical fill in the LHC. It is also indicated when the beam mode changes. The middle plot features the average heat loads on the cells of the cryogenic system in the eight arcs of the LHC. The sources of heat load besides the electron cloud are impedance and synchrotron radiation. At the bottom, the average bunch length is shown.

"stable beams" condition is declared and the experiments begin data collection. The intensity starts to decrease notably afterwards, mainly because of collisions at interaction points. This is also called the luminosity burn-off. Furthermore, the energy spread of the beam decreases since the protons with higher energy emit more synchrotron radiation than those with less energy. Since bunch length and energy spread are linked through the synchrotron motion, the former also decreases in the process (see Fig. 1.2). The machine is meant to operate for several hours in this way, until the intensity becomes too low and a planned dump takes place. Sometimes however, the beam has to be dumped early for machine safety reasons.

A short overview of the basic beam properties relevant for electron clouds is provided here. Most fills for proton physics in 2016 contained between 2040 and 2220 bunches, with up to $1.2{\cdot}10^{11}$ protons per bunch. A bunch spacing of 25 ns has been the main operational mode since 2015. The filling pattern is formed in the LHC injector complex, especially the PS and the SPS, and is occasionally changed to optimize the machine performance. It consists of batches of consecutively filled bunch slots separated by empty slots, see Fig. 1.3. The batches are separated by gaps of 225 ns, corresponding to the rise time of the SPS injection kicker. Several batches form a train, and consecutive trains are interrupted by at least 800 ns of empty slots due to the LHC injection kicker rise time. An abort gap of at least 3 μs has to be present at one point in the filling pattern, to enable an extraction at high energy towards the beam dump [7].

The long-term operational schedule of the LHC is divided into runs and long shutdowns (LS), each of which lasts between two and four consecutive years [9]. The beam operations take place during the runs, while the LS are reserved for maintenance and upgrades of the LHC and the injector complex. Figure 1.4 shows the time plan for the following years, which includes also the high luminosity upgrade of the LHC (HL-LHC). Afterwards, starting with run 4 in 2026, the LHC is meant to operate with bunch intensities of up to $2.2{\cdot}10^{11}$ p/bunch, much higher than the current limit of $1.5{\cdot}10^{11}$ p/bunch [8].

1.2 Modeling of secondary electron emission

The number of electrons in a beam pipe can increase rapidly through secondary electron emission, also known as multipacting. The basic concept of the electron cloud in an accelerator is sketched in Fig. 1.5. Free electrons in the chamber gain kinetic energy when they are accelerated by the beam, enough to extract more electrons after impacting on confin-

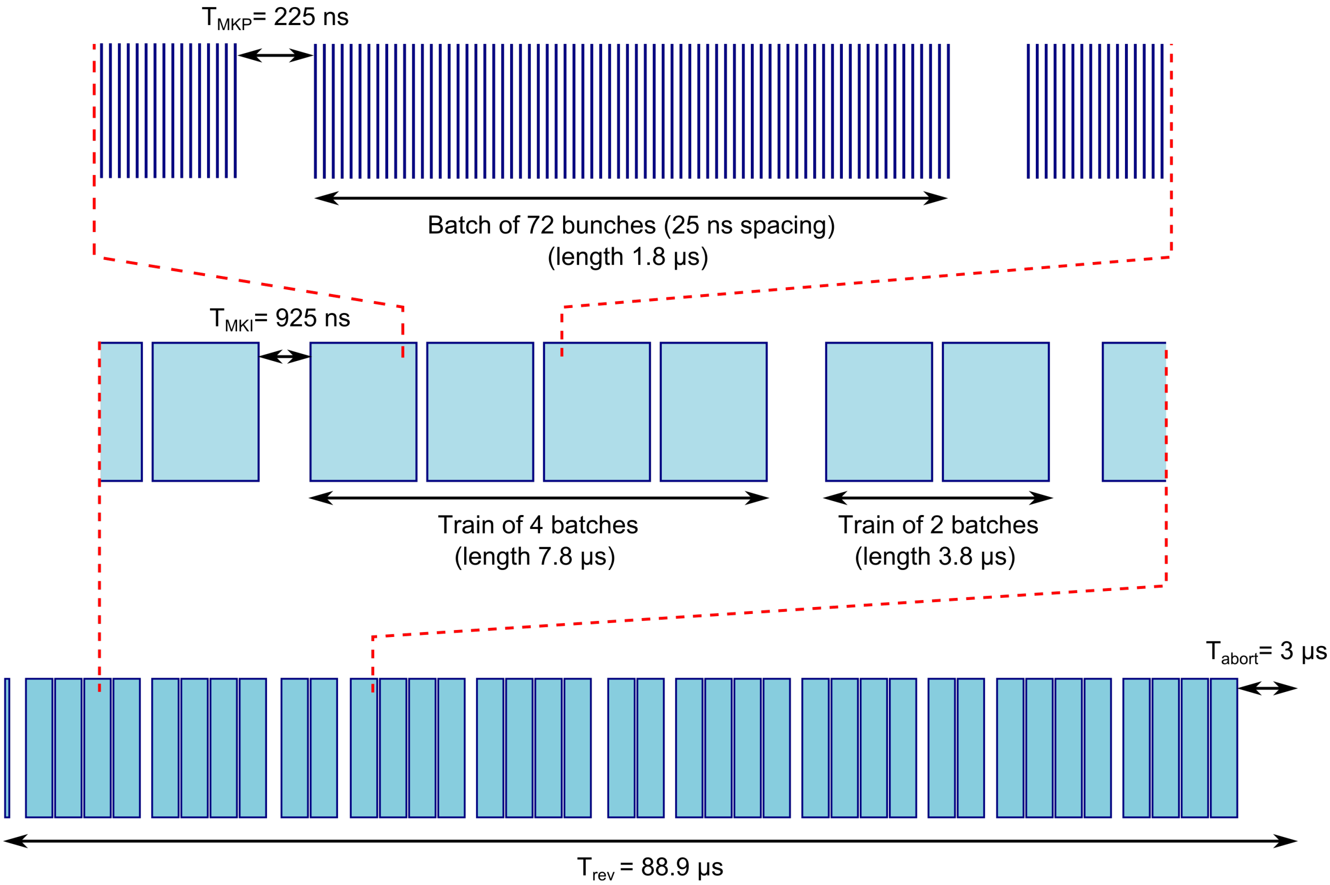

Figure 1.3: The LHC filling pattern consists of several trains, these in turn consist of several batches of consecutively filled bunch slots. The filling pattern has an important influence on the observed and simulated electron cloud effects [7].

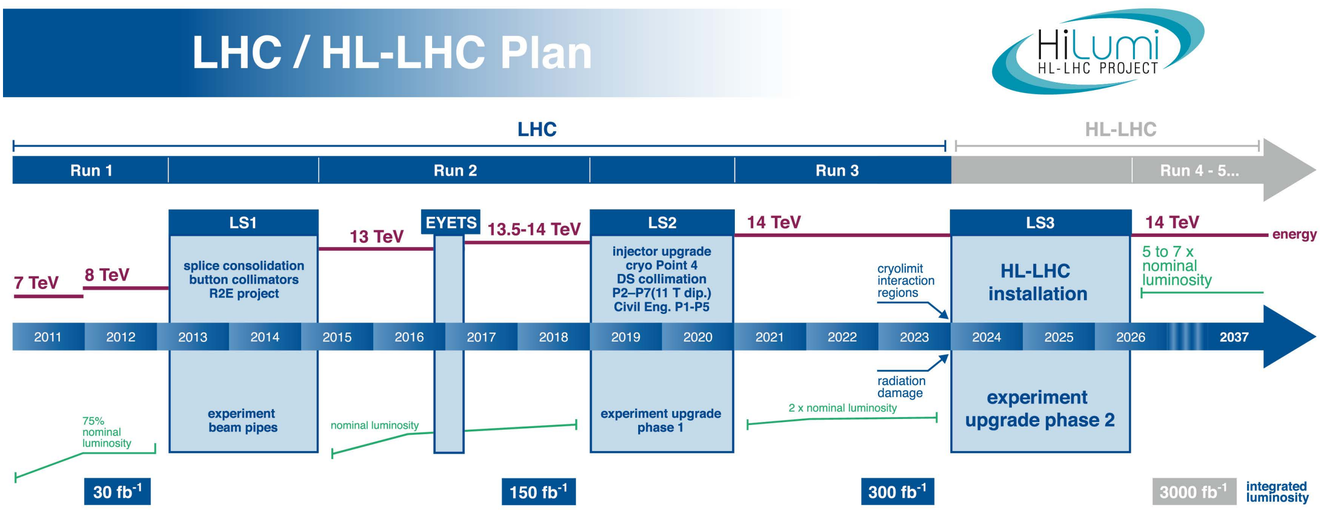

Figure 1.4: The schedule of the LHC operations since 2011 is outlined here, including the planned high luminosity upgrade. Some abbreviations used in this figure are Long Shutdown (LS) and Extended Year-End Technical Stop (EYETS). At the bottom, the expectations on the beam luminosity are noted in fb^{-1}. This is are a measure for the number of collisions in the detectors and therefore also the performance of the LHC from the point of view of the physics experiments. The collision energy in red is the sum of the energies of both beams [8].

ing surfaces. This process eventually reaches an equilibrium state when the space charge forces, created by the electrons already present, become large enough to mitigate further growth of the electron cloud.

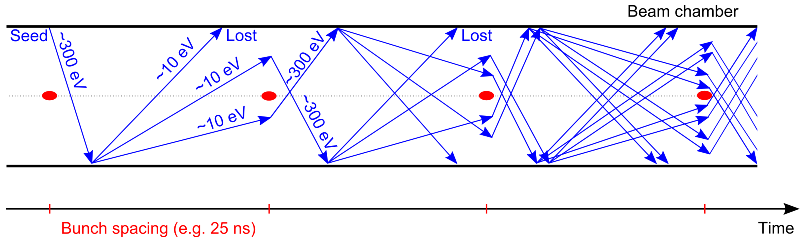

Figure 1.5: This sketch visualizes how a small number of electrons can trigger an avalanche effect. After they are accelerated by the positively charged beam, they hit the beam chamber, causing more electrons to emerge. The density eventually grows high enough to warrant the name "electron cloud" [7].

The process of secondary electron emission is subject of ongoing research at CERN and other labs. The CERN electron cloud team uses a model based on experimental data for copper [7, 10, 11, 12, 13, 14]. The surfaces of the beam chambers at the LHC are made of this material.

The secondary emission yield (SEY) δ is defined as the ratio between the electron current to the chamber surface and the emitted current. It depends on the energy of the impinging electrons E and their angle of incidence θ_i:

$$\delta(E,\theta_i) = \frac{I_{\text{Emit}}}{I_{\text{imp}}(E,\theta_i)} = \delta_{\text{true}}(E,\theta_i) + \delta_{\text{elas}}(E) \tag{1.1}$$

The emitted current, and therefore also $\delta(E,\theta_i)$, can be divided into parts formed by true secondary electrons and elastically scattered electrons. The latter are modelled in the following way, without a θ_i dependence:

$$\delta_{\text{elas}}(E) = R_0 \left(\frac{\sqrt{E} - \sqrt{E+E_0}}{\sqrt{E} + \sqrt{E+E_0}} \right)^2 \tag{1.2}$$

The two parameters R_0 and E_0 are set to 0.7 and 150 eV respectively in case of a copper surface. However there are conflicting opinions on the shape of the low energy part of this relation. Some authors say $\delta_{\text{elas}}(E \to 0)$ should approach 0, others state it should approach 1. The value 0.7 for R_0 is a compromise following this disagreement (see [15, 16] and references therein).

The yield of true secondary electrons depends on the shape parameter, s and on value of the incident energy resulting in the most secondary electrons, E_{max}:

$$\delta_{\text{true}}(E,\theta_i) = \delta'_{\text{max}}(\theta_i) \frac{s \frac{E}{E'_{\text{max}}(\theta_i)}}{s - 1 + \left(\frac{E}{E'_{\text{max}}(\theta_i)}\right)^s} \tag{1.3}$$

$$\delta'_{\text{max}}(\theta_i) = \delta_{\text{max}}\, e^{\frac{1-\cos\theta_i}{2}} \tag{1.4}$$

$$E'_{\text{max}}(\theta_i) = E_{\text{max}}\,(0.3 + 0.7\cos\theta_i) \tag{1.5}$$

High angles of incidence significantly increase the emission of true secondaries [10, 17, 18]. The angular dependence is motivated by the increased time that electrons spend close to the surface in case they penetrate the material with a large angle of incidence, enhancing their probability to create secondary electrons. Figure 5.4 in the appendix visualizes the exponential factor in Eq. 1.4.

The functions $\delta_{\text{true}}(E,\theta_i)$ and $\delta_{\text{elas}}(E)$ are shown in Fig. 1.6. In this model the elastic scattering only happens for incident energies below about 35 eV. The parameter δ_{max} depends on the chemical properties of the beam screen surface and is affected by electron bombardment, i.e. by the e-cloud itself (beam-induced conditioning) [19]. For this reason this parameter is scanned in almost all simulation studies and often called "the SEY parameter".

E_{max} and s on the other hand have been fixed at 1.35 and 330 eV for most simulations.

The energy of the emitted secondaries follows a log-normal distribution specified by μ and σ, normally determined as 1.08 and 1.66 [7, 20]:

$$\frac{\mathrm{d}n_{\text{true}}}{\mathrm{d}E} = \frac{1}{E\sigma\sqrt{2\pi}} e^{-\frac{(ln(E)-\mu)^2}{2\sigma^2}} \tag{1.6}$$

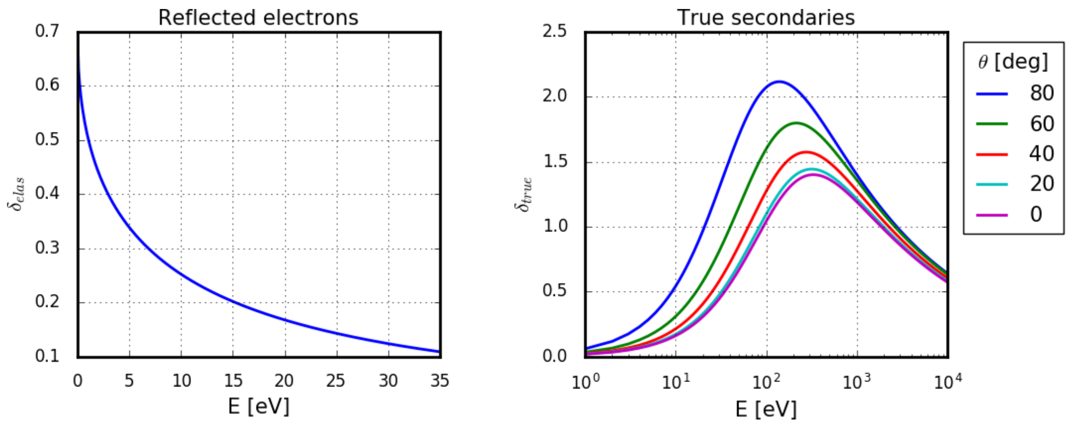

Figure 1.6: The true and reflected secondary electron yields (Eq. 1.2 and 1.3). Both depend on the energy of the impinging electron, and δ_{true} also depends on the angle of incidence θ_i.

Other, similar distributions could also be fitted to the underlying experimental data [21].

In the available literature on secondary electron emission, there is a broad consensus that the angle of emitted secondary electrons θ_e (measured relative to the surface normal) follows a $\cos\theta$ distribution, independent of the energy or incident angle of the impinging electrons. This is supported by measurements [22, 23, 24] and Monte-Carlo simulations [25]. Some authors draw a distinction between true secondary electrons and backscattered (rediffused) electrons and state that the latter follow a different angular distribution [26]. Others write that also the backscattered electrons follow a $\cos\theta$ distribution [24, 27]. In PyECLOUD, a $\cos\theta$ distribution is used to generate the angles of macroparticles from secondary emission as well as photoemission. On the other hand, the chamber wall is a mirror to the reflected photoelectrons ($\theta_e = \theta_i$).

As part of the studies featured in the master thesis proposal [1], the model parameters E_{max}, s, μ, σ, and the angular dependence of $\delta'_{\text{max}}(\theta_i)$ have been systematically varied. PyECLOUD simulations were performed and it was shown that the predicted heat loads and other results strongly react on even small changes of these parameters. In subsequent discussions it was suggested to also investigate the angles of incidence of impinging electrons in simulations. This information has now been added to the PyECLOUD simulation output, and a follow-up is provided in the appendix (Sec. 5.2).

1.3 The electron cloud simulation software PyECLOUD

PyECLOUD is a code that simulates the EC buildup in a thin slice around a certain section of a particle accelerator. Electrons are grouped in macro-particles (MP), in order to achieve a reasonable computational burden. The program is thoroughly described in [7], a summary of the principal features is provided here. Figure 1.7 shows a flowchart of the main loop in the simulation.

1. The simulation begins with electrons from a seeding process, where residual gas ionization and photoemission by synchrotron radiation are implemented. If one or both of them are enabled, new MPs are generated during each time step. Alternatively, an initial distribution of primary electrons can be specified without considering a seeding mechanism. This is a valid approximation in case there is multipacting and the electrons generated by the seeding process would soon become irrelevant compared to the large number of secondaries.
2. The rigid beam approximated is used, meaning that the beam charge distribution remains unaffected by the EC for the duration of the simulation. The electric fields generated by the beam charge are therefore calculated only once during the initialization stage. The beam charge distribution takes the following form

$$\rho(x,y,s,t) = \lambda(s-ct)\rho_\perp(x,y), \tag{1.7}$$

   where the transverse beam profile $\rho_\perp$ is assumed to be Gaussian. The longitudinal profile λ is either specified or also generated with a Gaussian form. The bunch lengths and bunch intensities can either be identical for all bunches, or specified individually. It is therefore possible to generate a beam profile from an FBCT (Fast Beam Current Transformer) measurement.
3. A Particle in Cell (PIC) algorithm is used to obtain the space charge forces of the electron cloud. The macro-particles are projected on a grid, and the electrostatic potential is calculated. The electric field corresponding to the space charge is then calculated as the gradient of the potential.

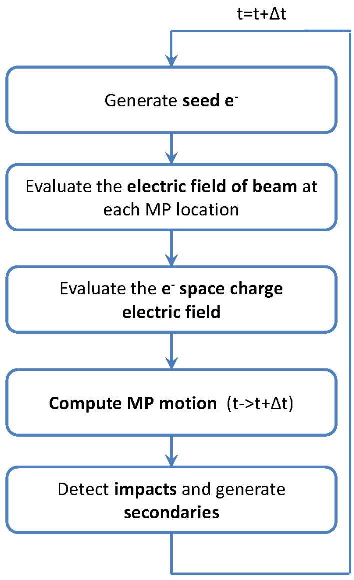

Figure 1.7: A flowchart of the PyECLOUD main loop [7].

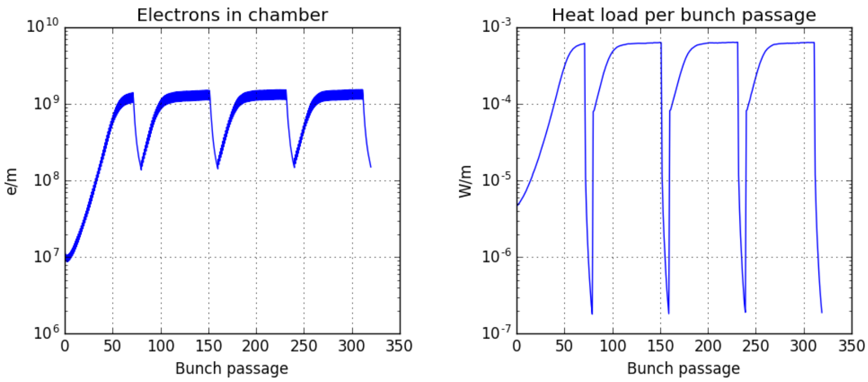

Figure 1.8: One train of protons (288 bunches) is simulated within a strong dipolar field. Left: the total number of electrons in the beam chamber. Right: The heat load per bunch passage, scaled with the revolution frequency of the LHC.

4. The MPs are tracked in the chamber while they are exposed to the electromagnetic forces from the confining magnet, the beam and the electrons themselves. The Lorentz force determines the movement of the particles.

$$\mathbf{F} = q\left(\mathbf{E} + \mathbf{v} \times \mathbf{B}\right) \tag{1.8}$$

   While several methods are implemented in PyECLOUD, the standard choice is the Boris algorithm [28]. Even though the Boris algorithm is not symplectic, it conserves the phase space volume and there is a global bound on the energy error [29]. Due to the importance of high accuracy in this part of the code, the tracking of the MPs is usually performed in several substeps. This part of the software has been modified in order to enable simulations of higher order magnets. This is described in Sec. 2.2.

5. When macro-particles impact on the chamber walls, it is decided which fractions of the electrons are treated as elastically reflected, are absorbed or create true secondary electrons. The size of the MP (the number of electrons it represents) may grow in the process. Once per bunch passage, a dedicated procedure may split up MPs that are too large and remove MPs that are too small. These minimum and maximum sizes are dynamic themselves, and depend on user setting as well as the current state of the simulation. If the total number of MPs exceeds a threshold defined by the user, the set of MPs is regenerated. This means that all electrons are rearranged to a new, smaller set of MPs, which decreases the computational burden of the following time steps [7].

6. During each time step, various kinds of information is stored. A complete list is part of the reference manual [30].

A part of the output from a typical PyECLOUD simulation is shown as an example in Fig. 1.8. The electron cloud generated by one train of proton bunches within a dipole of the LHC at 6.5 TeV beam energy is simulated. The 4 σ bunch length was set to 1.2 ns, and the bunch intensity to 1.1 $\cdot 10^{11}$ particles per bunch (nominal beam parameters). The train consists of 4 batches of 72 bunches each, separated by 8 empty slots. The parameter $\delta_{\max}$ is scanned, while the others (R_0, $E_{\max}$ etc.) are set as described in Sec. 1.2. The chamber is populated with an uniform initial distribution of 10^7 electrons, and no further seeding mechanism is enabled. The total number of electrons and the heat load per time step are shown in Fig. 1.8. Example plots for other types of output are part of the reference manual [30].

Over the course of this work, a misconception has been identified in the implementation of the $\cos\theta$ distribution for the emission angles of secondary electrons [31]. Section 5.1 in the appendix further elaborates this point and explains the necessary changes in the code and the consequences on simulation results.

The superconducting magnets at the LHC are cooled with liquid helium at 1.9 K and 1.3 bar, a state where helium is superfluid and possesses an excellent thermal conductivity [5, 32]. However, the thermodynamic cost of refrigeration at this low temperatures is large. There are different effects through which energy is transferred from the beam to the surrounding chamber. The most relevant are synchrotron radiation, the resistive wall effect (impedance) and the electron cloud. The cryogenic system is designed to intercept beam-induced heat loads at temperatures higher than 1.9 K to obtain of a more efficient cooling wherever possible. This is realized using a beam screen (BS), depicted in Fig. 1.9, that is thermally isolated from the liquid helium and is cooled with weakly supercritical helium at a temperature between 4 K and 20 K and a pressure of about 3 bar. The thermodynamic cost is thereby reduced by a factor of 8 with respect to 1.9 K isothermal cooling. The BS is made of steel with a surface of co-laminated copper [33]. Its pumping slots, necessary to uphold a good vacuum inside, are covered with shields that intercept electrons before they can reach the cold bore. Without this design feature, the effectiveness of the beam screen as an absorber of heat load would be significantly reduced [5, 34].

The majority of the beam screens at the LHC are installed within strong dipolar magnetic fields. At high beam energies, photons from synchrotron radiation constantly hit the side of the BS. Photoelectrons emitted at this point are confined there by the magnetic field and cannot move to the center of the pipe where the beam is located. Therefore, this part of the BS surface has a sawtooth structure (Fig. 1.9 right). Its purpose is to avoid a grazing impact of the photons to ensure a smaller probability of reflection and consequently reduce the number of photoelectrons elsewhere in the chamber [35, 36].

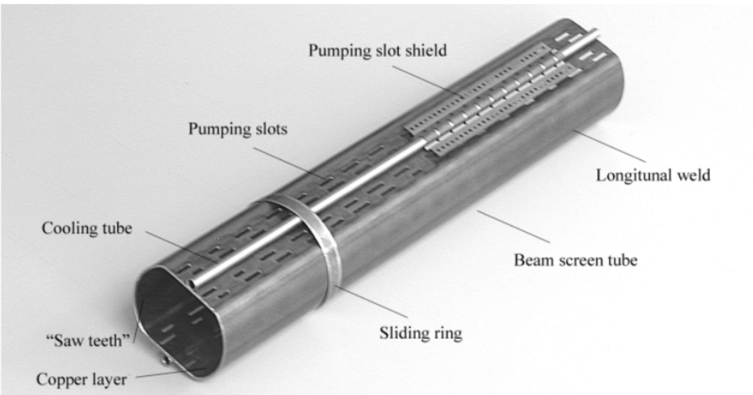

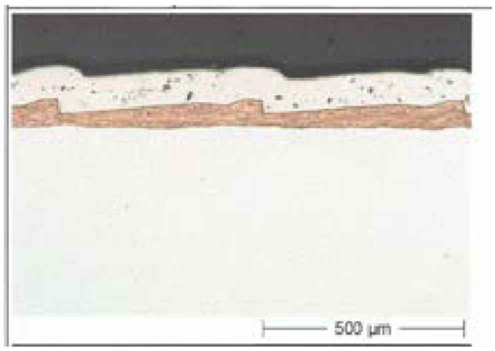

Figure 1.9: Left: the beam screen used at the LHC [5]. Right: a sawtooth structure present on the side where the synchrotron radiation first impacts, in order to have a low reflection probability of photons [16].

Despite the relatively efficient cooling of the beam screen, cryogenic plants are working to high capacity when the accelerator is operating at nominal beam parameters. This is shown in Fig. 1.10, where the e-cloud contribution to the measured heat load reached 150 W for the average cryogenic cell (length 53 m) in arc 12 during some fills.

Each LHC arc is subdivided into 52 cryogenic cells of 53 m. Because two cryogenic cells correspond to a FODO cell in terms of beam optics, these are often called half-cells. A sketch of the magnetic devices in one typical cell is depicted in Fig. 2.1 in Sec. 2.

The total heat load that is deposited on the beam screen is calculated separately for each cell. The procedure is based on an enthalpy balance of the cooling circuit and uses the measured temperature and pressure of the helium before and after it passes the cooling tubes attached to the beam screen. These values are stored in a logging database at CERN and are conveniently accessible. During the work on the master thesis proposal [1], a recomputation of the heat loads was implemented, and the necessary assumptions and simplifications were explained. The heat loads were recomputed for all cryogenic cells and all fills that occurred during run 2, starting in 2015. A database was created that combines beam parameters and heat loads [37, 38]. The heating that arises from impedance and synchrotron radiation is modeled with formulas that depend on beam parameters such as beam energy, intensity or bunch length [37, 39, 40, 41]. The remainder is attributed to the electron cloud.

Figure 1.10 shows the heat loads of all fills since 2015 that have reached the "stable beams" mode.

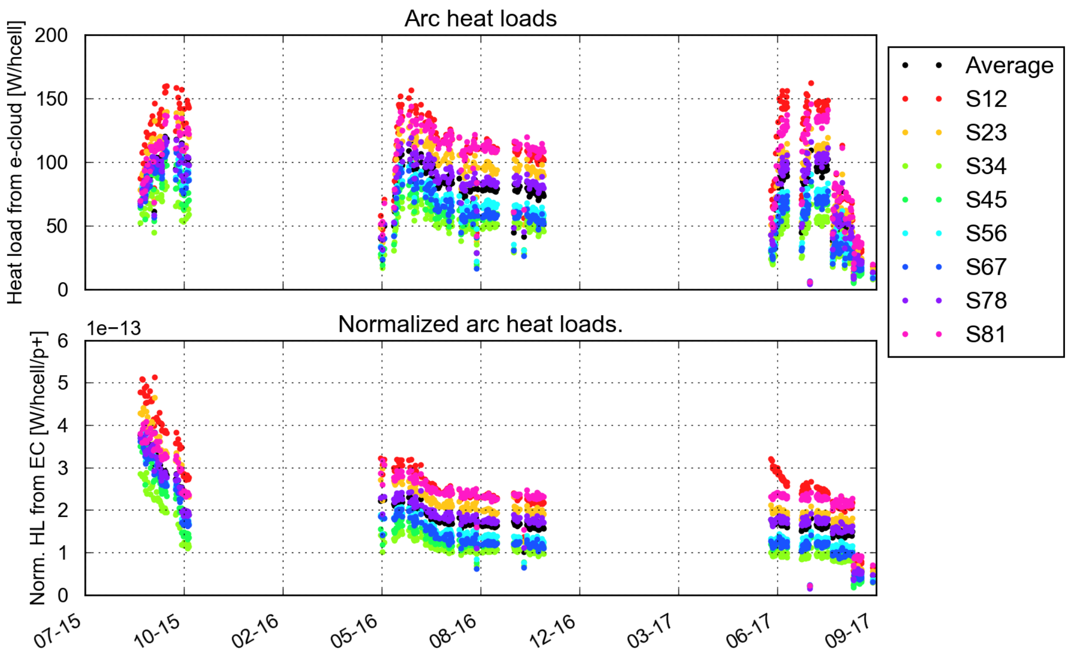

Figure 1.10: Top: the average heat loads in the cryogenic cells of the LHC arcs are shown here for all fills that reached the "stable beams" mode. Bottom: the absolute heat load was normalized by the total beam intensity in order to better compare fills with different beam parameters. The values (one point per fill) were recorded when the beam mode "stop squeeze" was announced. The modelled contributions from synchrotron radiation and impedance have been subtracted to arrive at values that correspond to the heat load caused by electron cloud only. The naming convention of the arcs is such that arc S12 is connecting Point 1 and Point 2 of the accelerator (see also Fig. 1.1). The fills on the right part of the graphs, starting in 09-17, were performed with the 8b+4e bunch pattern, which strongly reduces the e-cloud formation.

1.5 Motivation

It is a priority at CERN to understand the behavior of the electron cloud in the LHC and other machines. For the nominal parameters of the LHC beams, the cryogenic plants at some of the arcs operate at around 75% of their maximum cooling capacity. This is shown in Fig. 1.2, where average heat loads of up to 120 W per cryogenic cell are measured in some arcs, while the performance limit of the cooling circuits is known to be 160 W. Moreover, it is important to predict heat loads for the future operation of the LHC should beam parameters change, especially after the high luminosity upgrade. Future accelerators operating with positively charged particles are likely to also suffer from electron cloud phenomena such as heat loads or beam degradation.

Electron cloud effects have therefore been studied at CERN for many years. In contrast to previous studies of buildup simulations for the LHC [7], the heat load data that has been accumulated during run 2 is now available. Especially the measured heat loads on the cryogenic system can provide insight, as they are primarily caused by electron clouds. This is even more significant because e-cloud effects are much stronger at a bunch spacing of 25 ns, the default configuration of run 2 that is also going to be used for the HL-LHC [8]. During the preceding run 1, 50 ns were used for the most part instead.

The master thesis proposal [1] reports on the work that has been performed during the first six months of this project. Progress could be made especially in terms of data accumulation and data analysis. The heat loads for all cryogenic cells during run 2 (2015-present) were recalculated. The results were stored in a database, which has been very useful as an analysis tool [37, 38]. Another application of the measured heat loads are comparisons to electron cloud simulation results. The second half of the project is consequently focussed on build-up simulation studies of the cryogenic cells of the present LHC. The magnetic elements that are part of the cryogenic cells are described in Sec. 2.1. They contain also higher order magnets such as sextupoles and octupoles. The PyECLOUD code did not support these devices, and therefore had to be extended (Sec. 2.2).

Another part of this work is about simulations with photoemission seeding. Since synchrotron radiation scales with the beam intensity as well as the beam energy, this seeding mechanism will also be highly relevant for future machines that surpass the LHC in these aspects. Examples are, besides the already mentioned HL-LHC, FCC-hh [42] and FCCee [43], both of which are currently in the design phase. Seeding by electrons generated from photoemission was already implemented in PyECLOUD prior to this work [7]. Deciding on which model parameters to use is however not obvious. Results from various measurement campaigns of beam screen materials have been published in the late 90s and early 2000s. A literature review is thus necessary to obtain reasonable parameters.

In order to compare heat load measurements of the LHC cryogenic cells to predictions from simulations, a model of the average cryogenic cell is created. It has also been used in the studies on photoemission, presented in Sec. 3. Magnetic field configurations of devices other than regular dipoles and quadrupoles could not be simulated in PyECLOUD prior to this work. The code has been changed and it is now possible to specify arbitrarily high multipole moments as well as skew and compound magnets. PyECLOUD simulations of sextupoles and octupoles could be performed for the first time. Results from these studies are shown in comparison to the quadrupole device.

2.1 Model of the average cryogenic cell in the LHC arcs

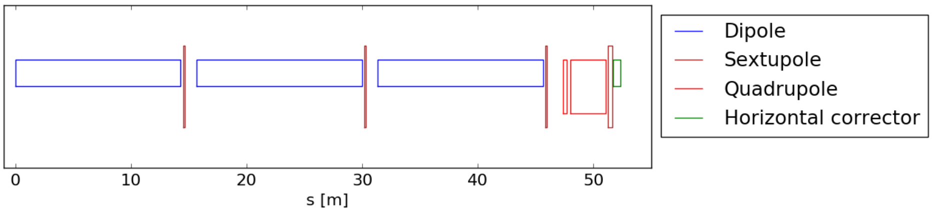

Figure 2.1: All cryogenic cells in the LHC arcs contain three main dipoles and one main quadrupole, interleaved by corrector magnets in different configurations. In this plot, one of the most common types of cells is sketched, showing only the magnetic elements.

The information of all magnetic elements in an accelerator (their position, lengths and field strengths), is essential for simulations of beam dynamics. One of the codes used at CERN for beam optics design is MAD-X [44]. The input files for the simulation of the full LHC ring with this code are available, and the data necessary for the model of the average cell has been extracted.

The magnetic lengths of all magnetic devices of the same type within the arcs of the LHC are summed up, and divided by the total number of cells. The remainder that is necessary to obtain a cell length of 53.45 m [5] is attributed to drift space. Table 2.1 shows the resulting lengths and magnet types.

Magnet	**Length of magnet** [m]	**Average length per half cell** [m]	**Magnetic field**
Drift	-	5.79	-
Main Bend (MB)	14.30	42.90	7.7 T
Horizontal corrector (MCBH)	0.65	0.32	2.7 T
Vertical corrector (MCBV)	0.65	0.32	2.3 T
Main quadrupole (MQ)	3.10	3.27	$1.7{\cdot}10^2$ T/m
Sextupole (MS)	0.37	0.35	$1.5{\cdot}10^3$ T/m^2
Sextupole (MS2)	0.37	0.35	$-2.6{\cdot}10^3$ T/m^2
Octupole (MO)	0.32	0.15	$5.8{\cdot}10^4$ T/m^3

Table 2.1: Magnetic field strengths and gradients at 6.5 TeV beam energy that were used in the simulations for this study.

The average magnetic length of a single magnet is given in the first column. As a simplification, short corrector magnets of the same type are considered only for the evaluation of the length, even though their actual fields are different. For example, a quadrupolar corrector magnet with a length of 32 cm is installed in more than half of the cryogenic cells, which here simply increases the average main quadrupole length. An exception are the dipolar corrector magnets, since they are long enough to warrant a special treatment (on average 32 cm per cell). A large difference is observed between horizontal and vertical dipole corrector magnets, due to the asymmetry of the beam screen and the uneven distribution of photoelectrons from synchrotron radiation. The field strengths in Tab. 2.1 are typical values used at the LHC.

The multipole expansion of the magnetic field is treated in standard textbooks on particle accelerators such as [46], or lecture notes [45]. In Cartesian coordinates, one way to express the magnetic fields is the following (from [45]):

$$B_y + iB_x = \sum_{n=1}^{\infty}(\tilde{b}_n - i\tilde{a}_n)(x+iy)^{n-1} \tag{2.1}$$

where B_y and B_x are the magnetic field components in vertical and horizontal directions, and $\tilde{a}_n$ and $\tilde{b}_n$ are real constants. By redefining the constants ($\tilde{b}_{n+1} = n!b_n$, etc), this can be written in terms of the normal (b_n) and skew (b'_n) field derivatives:

$$B_y + iB_x = \sum_{n=0}^{\infty}\frac{1}{n!}(b_n + ib'_n)(x+iy)^n \tag{2.2}$$

$$b_n = \left.\frac{\partial^n B_y}{\partial x^n}\right|_{(x,y)=(0,0)} \tag{2.3}$$

$$b'_n = \left.\frac{\partial^n B_x}{\partial x^n}\right|_{(x,y)=(0,0)} \tag{2.4}$$

It is now shown that Eq 2.3 holds. Equation 2.4 can be obtained in a similar way.

$$B_y = \Re\left(\sum_{m=0}^{\infty}\frac{1}{m!}(b_m + ib'_m)(x+iy)^m\right) \tag{2.5}$$

$$\frac{\partial^n B_y}{\partial x^n} = \Re\left(\sum_{m=n}^{\infty}\frac{1}{(m-n)!}(b_m + ib'_m)(x+iy)^{m-n}\right) \tag{2.6}$$

$$\left.\frac{\partial^n B_y}{\partial x^n}\right|_{(x,y)=(0,0)} = \Re\left(\sum_{m=n}^{\infty}\frac{1}{(m-n)!}(b_m + ib'_m)\delta_{mn}\right) \tag{2.7}$$

$$= \Re\left(b_n + ib'_n\right) = b_n \tag{2.8}$$

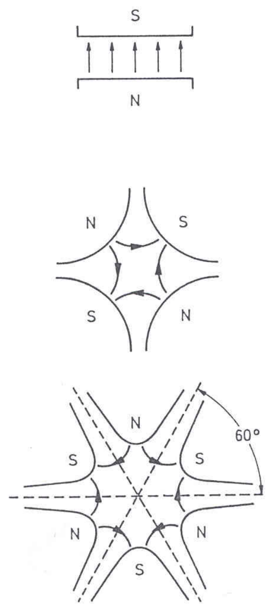

Figure 2.2: The magnetic field lines within dipoles, quadrupoles and sextupoles [45].

Multipoles of orders higher than quadrupoles (n=1) could not be implemented in PyECLOUD versions prior to 6.2. This functionality has been added in order to perform the studies presented in the following sections.

The Boris algorithm [28] is used to track the macroparticles in the code. These are exposed to electric forces from the beam and the other macroparticles (space-charge), and to magnetic forces from the magnet that confines the beam chamber. The magnetic field (B_x, B_y) has to be calculated at the position of each macroparticle. A significant amount of the computational time is spent in this part of the code. Therefore it is written in C instead of Python.

The implementation of Eq. 2.1 is shown below. The user specifies b_n and b'_n as the normal and skew magnetic field strengths in form of an array. One example would be $b_n = [0., 12.]$, which corresponds to a quadrupolar field with $12\frac{\mathrm{T}}{\mathrm{m}}$. The factor $\frac{1}{n!}$ is applied during the initialization process of the simulation, the arrays are then passed to the C function under the names 'B_field' and 'B_skew'. The part $(x+iy)^n$ is built incrementally, which means it can be reused in case of a compound magnet. A significant speedup could be obtained by using two floats instead of one complex data type for the expressions $(B_y + iB_x)$ and $(x+iy)$.

The variables 'rexy' and 'imxy' correspond to the real and imaginary parts of ($(x+iy)^n$). 'xn1p' and 'yn1p' are the coordinates of the macroparticle. 'Bx_n' and 'By_n' correspond to B_x and B_y.

```
rexy = 1.; // Real part of (x+iy)^n
imxy = 0.; // Imaginary part of (x+iy)^n
By_n = B_field[0]; // Dipole covered here
Bx_n = B_skew[0];
for(order = 1; order < N_multipoles; order++){
    rexy_0 = rexy;
    rexy = rexy_0*xn1p - imxy*yn1p; // explicit complex arithmetics
    imxy = imxy*xn1p + rexy_0*yn1p;

    By_n += (B_field[order]*rexy - B_skew[order]*imxy); // explicit complex arithmetics
    Bx_n += (B_field[order]*imxy + B_skew[order]*rexy);
}
```

This part of the code is verified with a testing procedure. The macroparticle module of PyECLOUD is initialized and populated with equally spaced macroparticles, with their velocities pointing in z direction. One step of the Boris algorithm is then applied. After the tracking, the coordinates of the particles are shifted and they also have a velocity component in transverse direction, from which the acceleration is approximated using $\mathbf{a} = \Delta\mathbf{v}/\Delta t$. Using Newton's law $\mathbf{F} = m \cdot \mathbf{a}$, the Lorentz force that led to the particle movement is calculated. The Lorentz equation 1.8 is then solved for B:

$$B_x = \frac{F_y}{qv_z} = \frac{ma_y}{qv_z} = \frac{m\Delta v_y}{qv_z\Delta t} \tag{2.9}$$

$$B_y = -\frac{F_x}{qv_z} = -\frac{ma_x}{qv_z} = -\frac{m\Delta v_x}{qv_z\Delta t} \tag{2.10}$$

This procedure has been applied to dipoles, quadrupoles, sextupoles and octupoles. Their field gradients were set to 1 T, 1 T/m, 2 T/m^2, and 6 T/m^3, respectively. In this way the field B_y is always 1 T for $y = 0$, $x = 1$ m. B_x along the y axis and B_y along the x axis are shown in Fig. 2.3. The field lines are shown in Fig. 2.4.

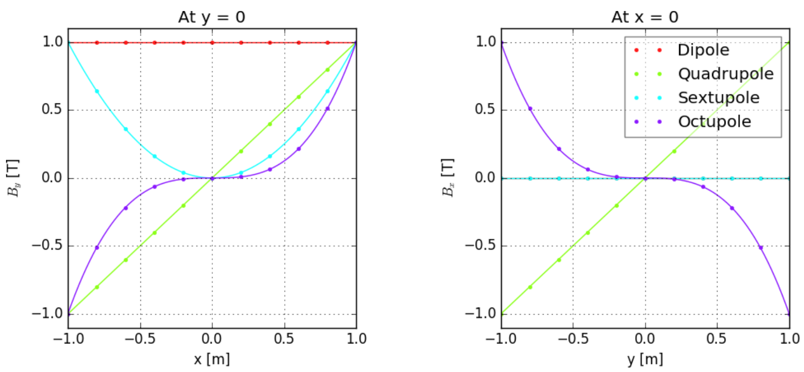

Figure 2.3: A test script that is part of the code is used to generate these plots. The magnetic fields are calculated at discrete positions using Eq. 2.9 and Eq. 2.10. A good agreement with the expected values is reached.

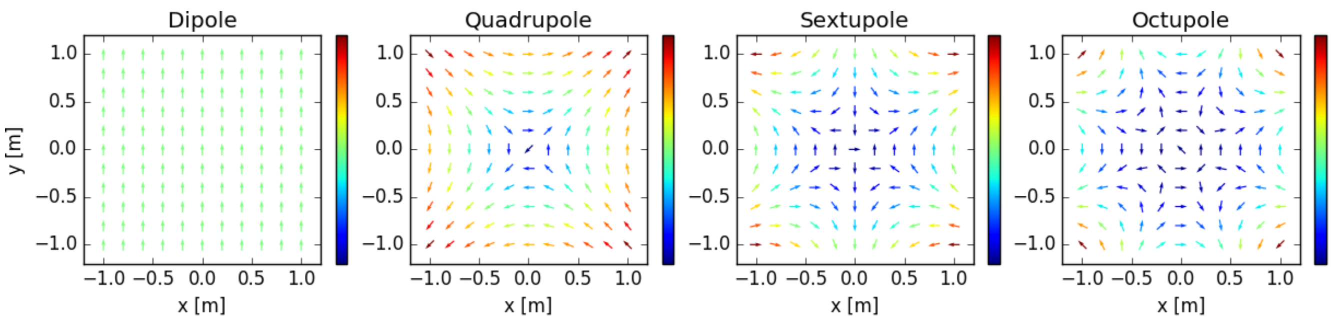

Figure 2.4: These field maps were also generated with a test script and validate the correct alignment (Fig. 2.2). The color of the arrows indicates the strength of the field.

The field strengths of magnetic elements are often expressed as normalized coefficients, usually denoted k_n. They are obtained by normalizing the field strengths with the beam rigidity $B\rho$, a factor that is proportional to the beam momentum p [46]. The constant e is the elementary charge.

$$k_n = \frac{1}{B\rho} \frac{\partial^n B_y}{\partial x^n}\bigg|_{(x,y)=(0,0)} \tag{2.11}$$

$$k'_n = \frac{1}{B\rho} \frac{\partial^n B_x}{\partial x^n}\bigg|_{(x,y)=(0,0)} \tag{2.12}$$

$$B\rho = \frac{p}{e} \tag{2.13}$$

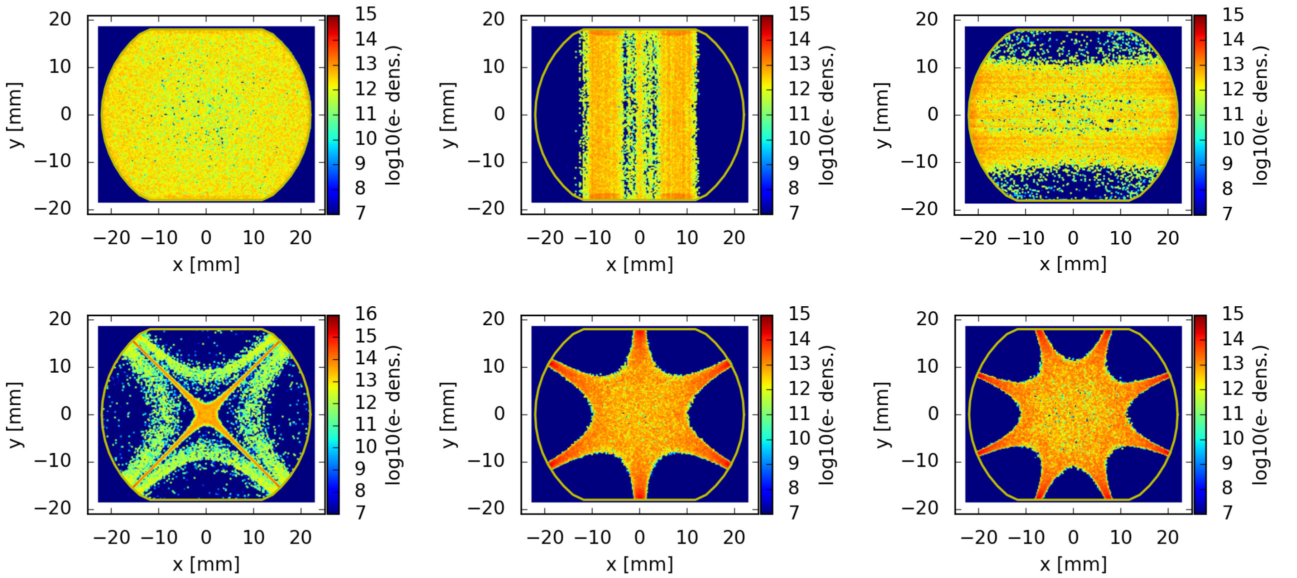

Figure 2.5: The electron density distributions within drifts, dipoles, vertical dipolar correctors, quadrupoles, sextupoles and octupoles as obtained from typical PyECLOUD simulations.

Simulation studies of sextupoles and octupoles are presented here for the first time. Snapshots of the electron distributions in various elements are shown in Fig. 2.5. They are compared to results from quadrupole simulations, a device which has been extensively studied before [1, 7].

Simulations were performed with different magnetic field strengths, bunch intensities and δ_{max} parameters. Figure 2.6 shows different results from the simulations. First of all, the heat loads for different values of the magnetic field gradients and δ_{max} are shown. The gradients were scanned with logarithmic spacing between different values. It becomes clear that in most cases, higher field strengths lead to an increased electron cloud. One exception is the quadrupole, where a maximum is observed for medium gradients of 36 T/m. For very low magnetic fields, the devices behave similar to drifts (depicted in Fig. 3.6), as expected. The octupole is only affected by multipacting at high fields strengths.

Furthermore, the central electron densities are shown. These are defined as the number of electrons in a sphere of radius 1 mm, normalized by the volume. Quadrupoles and sextupoles are very similar in this aspect. This could be relevant for studies of electron cloud induced instabilities, where the central density is of greatest importance.

The shape of the total deposited energy on the chamber surface, projected to the x-coordinate, is consistent with the 2D density plots in Fig. 2.5. Energy is only deposited at a few localized spots, where the field lines cross the surfaces.

The energy histogram of impacting electrons is interesting, since it allows to draw conclusions on whether electrons become trapped in the magnetic field similar to a magnetic bottle. Trapped electrons can remain in the chamber without impacting for a longer time and get accelerated by multiple subsequent proton bunches. In dipoles, where this effect is impossible, as the field strength is approximately constant everywhere in the chamber, impacts with an energy higher than 1 keV are very rare [47] (at least for bunch intensities around $1.1 \cdot 10^{11}$ p/bunch). This effect is observed in the case of quadrupolar fields, where a sharp maximum of occurring impacting energies does not exist, although low impact energies are still the most probable. The e-cloud in sextupoles does again behave in a similar way, although the slope is steeper which means trapping is less likely. This trend is continued with the octupole, where the average impact energies are even smaller.

The dependence of the heat loads on beam intensity is shown in Fig. 2.7. For different devices and δ_{max}, the depicted curves have a very different shape. It appears that there is always one bunch intensity where the electron cloud formation is strongest. This can be explained with the shape of the secondary electron yield $\delta_{\text{true}}(E)$ (Eq. 1.3). At the right beam intensity, most electrons end up with a kinetic energy that favors secondary electron emission. In the secondary emission model presented in Sec. 1.2, E_{max} is the electron energy that yields the most secondaries upon impacts. The simulations here were performed with an E_{max} parameter of 330 eV.

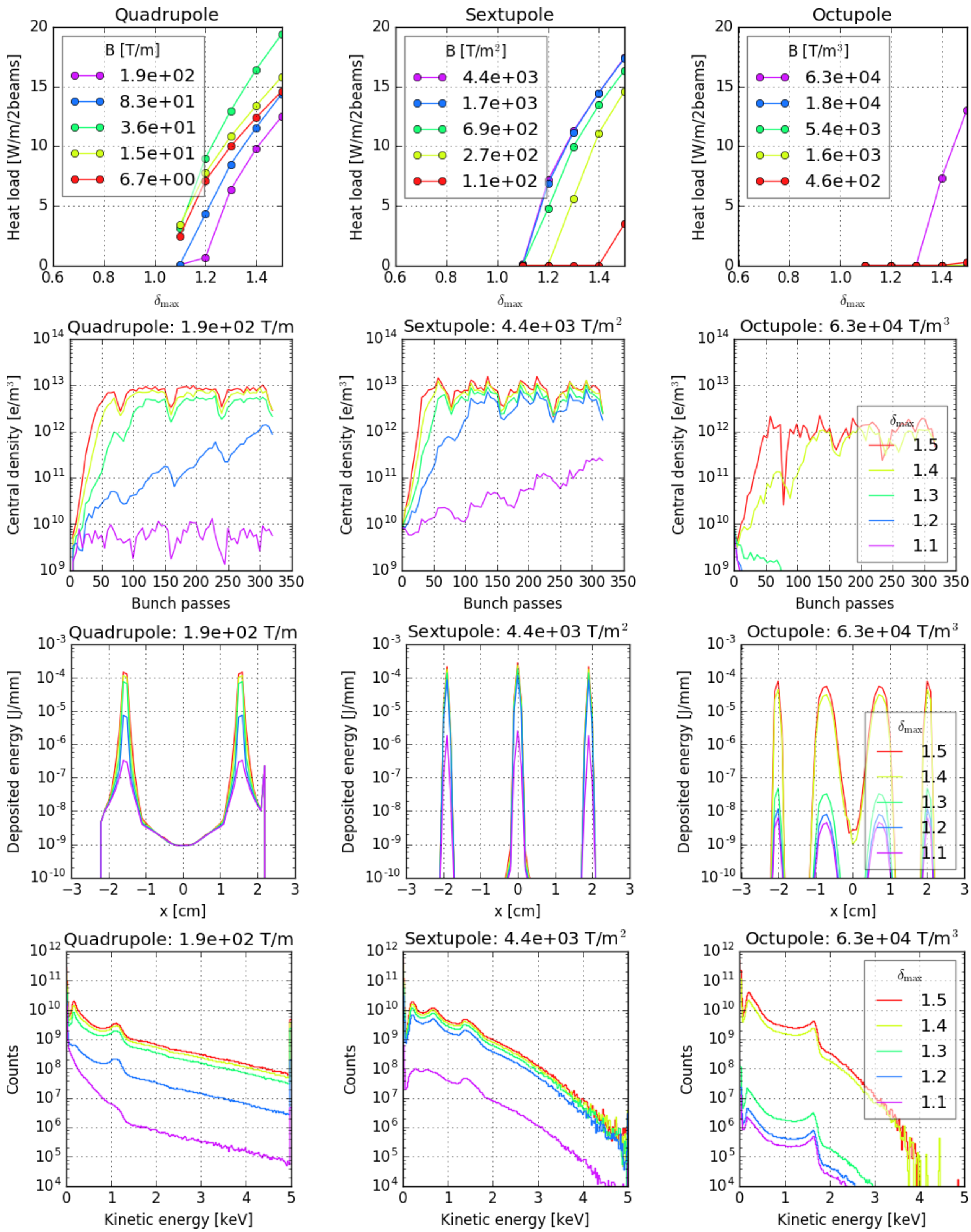

Figure 2.6: Results from simulations of higher order magnets are compared to quadrupoles. The bunch intensities in all simulations depicted here were set to $1.1{\cdot}10^{11}$ p/bunch.
1st row: the heat loads at different magnetic field gradients.
2nd row: the central electron density close to the beam.
3rd row: histograms of deposited energy along the x-axis of the chamber.
4th row: histograms of the kinetic energies of impacting electrons.

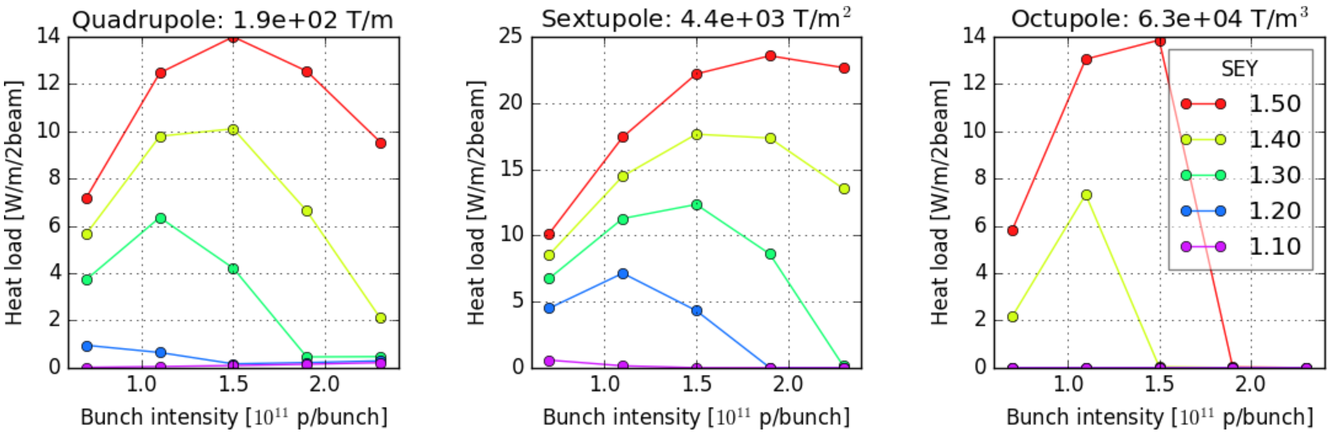

Figure 2.7: The scaling of the heat loads with beam intensity is shown here for the highest possible field strengths for each device.

In summary, the properties of sextupole simulations are very similar to those of quadrupoles, especially considering the most relevant results, namely total deposited heat loads and the electron density in proximity to the beam. The octupole on the other hand is more similar to the drift spaces in case the magnetic field is relatively low, since there is no multipacting in the absence of photoemission seeding (see also Sec. 3.4). Only for the highest magnetic fields that were simulated, the behaviour is closer a quadrupole.

The number of photons that are capable of producing photoelectrons is calculated from basic electro-dynamic equations in the following pages. The beam screen at the LHC has a copper surface (see also Fig. 1.9 in Sec. 1.4). The photoelectric properties of this material have been measured at CERN and other laboratories in the late 90s and early 2000s [48, 49, 50, 51]. The results are summarized and compared in this report. Input parameters for PyECLOUD build-up simulations are determined starting from this information. These were used in simulations of the magnetic elements that are part of the cryogenic cells of the LHC arcs, such as dipoles, quadrupoles and drift spaces. The estimated heat loads are compared to measurements at the LHC, and the overall importance of photoelectron seeding is discussed.

3.1 High energy photons from synchrotron radiation

The amount of photons generated by a charged particle (protons in the case of the LHC) on a circular trajectory is derived in the following. This problem is solved analytically following the treatment explained in [52].

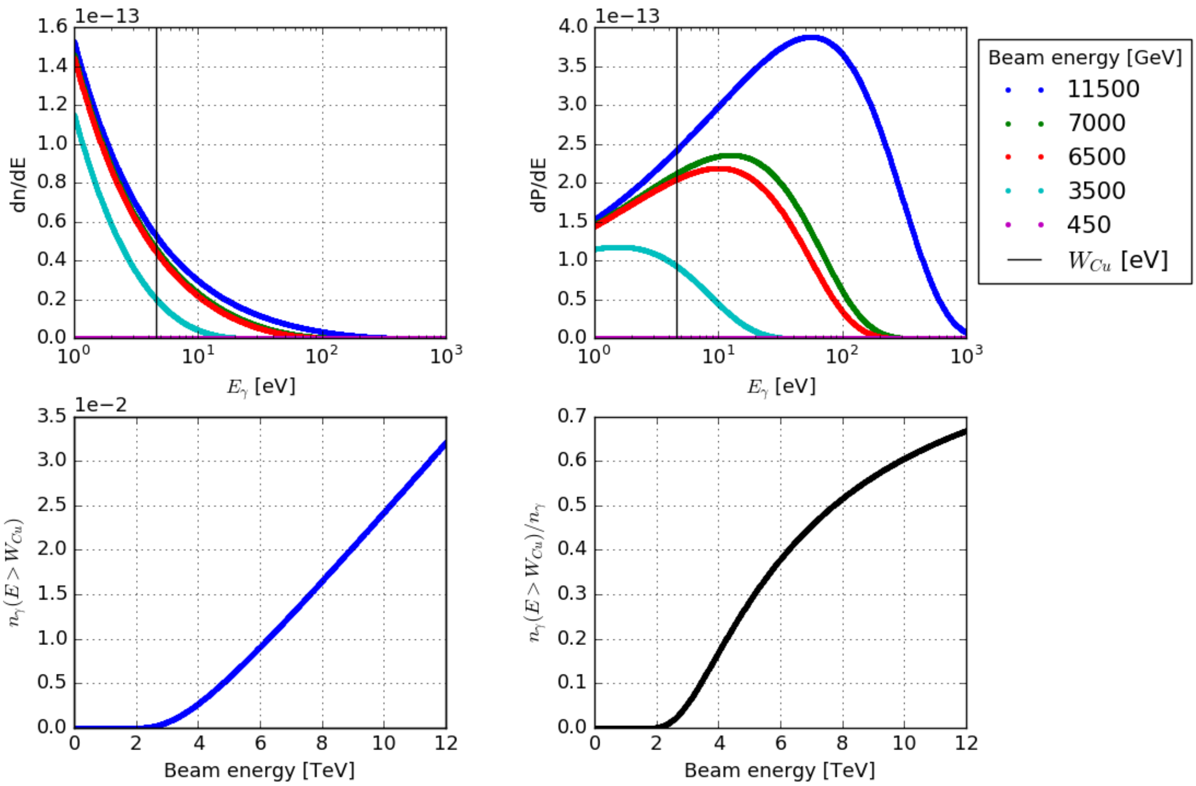

Figure 3.1: Top left: the photon energy distribution of the synchrotron radiation emitted by a proton travelling in an LHC dipole with different kinetic energies. Top right: the corresponding emitted power spectrum. Bottom left: the number of photons above the work function of copper W_{Cu} (4.6 eV [53]) as a function of the proton energy for different energies of the LHC proton beam. Bottom right: the fraction of photons with an energy above the work function of copper as a function of the proton energy for different energies of the LHC proton beam.

The following equation describes the power spectrum $\frac{\mathrm{d}P}{\mathrm{d}\omega}$ of the radiation emitted by a highly relativistic charged particle on a circular trajectory:

$$\frac{\mathrm{d}P}{\mathrm{d}\omega} = \frac{P_s}{\omega_c} S_s\left(\frac{\omega}{\omega_c}\right) \tag{3.1}$$

where P_s is the total emitted power, ω_c the critical frequency of the radiation and the function S_s an integral of the modified Bessel function $K_{5/3}$:

$$P_s = \frac{e^2}{4\pi\epsilon_0}\frac{2c\gamma_{\mathrm{rel}}^4}{3\rho^2} \tag{3.2}$$

$$\omega_c = \frac{E_c}{\hbar} = \frac{3c\gamma_{\mathrm{rel}}^3}{2\rho} \tag{3.3}$$

$$S_s(x) = \frac{9\sqrt{3}}{8\pi}x\int_x^\infty K_{5/3}(z)\,\mathrm{d}z \tag{3.4}$$

The trajectory is characterized by the bending radius ρ, and the charged particle by the relativistic parameter γ_{rel}. The emitted power spectrum is related to emitted photons per unit time $\frac{\mathrm{d}\dot{n}_\gamma}{\mathrm{d}\omega}$:

$$\frac{\mathrm{d}P}{\mathrm{d}\omega} = \hbar\omega\frac{\mathrm{d}\dot{n}_\gamma}{\mathrm{d}\omega} \tag{3.5}$$

Using Eq. 3.1 yields:

$$\frac{\mathrm{d}\dot{n}_\gamma}{\mathrm{d}\omega} = \frac{1}{\hbar\omega}\frac{\mathrm{d}P}{\mathrm{d}\omega} = \frac{1}{\hbar\omega}\frac{P_s}{\omega_c}S_s\left(\frac{\omega}{\omega_c}\right) \tag{3.6}$$

The top left graph in Fig. 3.1 shows the photon spectrum from Eq. 3.6 as a function of the photon energy, while the top right plot shows the power spectrum of the radiation. The photon energy is related to the radiation frequency by:

$$E_\gamma(\omega) = \hbar\omega \tag{3.7}$$

Integration of Eq. 3.6 yields the number of photons per second above a certain frequency, which is relevant later in this report. In the following, the substitution $x = \frac{\omega}{\omega_c}$ is used, and the definition of $S_s(x)$ in Eq. 3.4 is applied.

$$\dot{n}_\gamma(\omega > \omega_{\mathrm{min}}) = \frac{P_s}{E_c}\int_{\omega_{\mathrm{min}}}^\infty \frac{1}{\omega}S_s\left(\frac{\omega}{\omega_c}\right)\,\mathrm{d}\omega \tag{3.8}$$

$$= \frac{P_s}{E_c}\int_{\omega_{\mathrm{min}}/\omega_c}^\infty \frac{1}{x}S_s(x)\,\mathrm{d}x \tag{3.9}$$

$$= \frac{P_s}{E_c}\frac{9\sqrt{3}}{8\pi}\cdot\int_{\omega_{\mathrm{min}}/\omega_c}^\infty\int_x^\infty K_{5/3}(z)\,\mathrm{d}z\,\mathrm{d}x \tag{3.10}$$

The double integral in Eq. 3.10 can be rewritten, with the substitution $x_{\mathrm{min}} := \frac{\omega_{\mathrm{min}}}{\omega_c}$ and using integration by parts.

$$\int_{x_{\mathrm{min}}}^\infty \underbrace{\int_x^\infty K_{5/3}(z)\,\mathrm{d}z}_{=F(x)}\,\mathrm{d}x = \int_{x_{\mathrm{min}}}^\infty F(x)\cdot 1\,\mathrm{d}x \tag{3.11}$$

$$= \underbrace{\lim_{x\to\infty} F(x)\cdot x}_{=0} - F(x_{\mathrm{min}})\cdot x_{\mathrm{min}} - \int_{x_{\mathrm{min}}}^\infty F'(x)\cdot x\,\mathrm{d}x \tag{3.12}$$

$$= -\int_{x_{\mathrm{min}}}^\infty K_{5/3}(x)\,\mathrm{d}x\cdot x_{\mathrm{min}} - \int_{x_{\mathrm{min}}}^\infty (-K_{5/3}(x))\cdot x\,\mathrm{d}x \tag{3.13}$$

$$= \int_{x_{\mathrm{min}}}^\infty K_{5/3}(x)(x - x_{\mathrm{min}})\,\mathrm{d}x \tag{3.14}$$

The number of photons above a certain frequency per unit path length is obtained by applying a factor of $1/c$ to $\dot{n}_\gamma(\omega > \omega_{\mathrm{min}})$ from Eq. 3.8. This variable is called $n_\gamma(\omega > \omega_{\mathrm{min}})$ for the remainder of this report, where γ stands for photon and is not to be confused with γ_{rel}.

$$n_\gamma(\omega > \omega_{\mathrm{min}}) := \frac{1}{c}\dot{n}_\gamma(\omega > \omega_{\mathrm{min}}) = \frac{\sqrt{3}}{8\pi^2}\frac{e^2\gamma_{\mathrm{rel}}}{\hbar c\epsilon_0\rho}\cdot\int_{\omega_{\mathrm{min}}/\omega_c}^\infty \mathrm{d}x\,K_{5/3}(x)(x - \frac{\omega_{\mathrm{min}}}{\omega_c}) \tag{3.15}$$

Note that also ω_c depends on $\gamma_{\rm rel}$ (Eq. 3.3), with the effect that $n_\gamma(\omega > \omega_{\min})$ depends nonlinearly on the beam energy as shown in Fig. 3.1.

Due to the photoelectric effect, electrons can be extracted from the beam chamber surface. The work function of a metal is the energy gap between the Fermi and vacuum energy levels [54], which, in the case of copper, is 4.6 eV [53]. Only photons with energies sufficient to cross this gap can contribute to the photoelectron generation process. The bottom plots in Fig. 3.1 show the number of such photons per unit length and per proton, as well as their ratio with respect to all photons.

Another interesting feature is the angular distribution of photons. Far above the critical angle θ_c, emission of synchrotron radiation is negligible. The critical angle can be written as:

$$\theta_c(\omega) = \frac{1}{\gamma_{\rm rel}}\left(\frac{2\omega_c}{\omega}\right)^{1/3} = \left(\frac{3c}{\rho\,\omega}\right)^{1/3} \tag{3.16}$$

For energies corresponding to the copper work function, the critical angle is about 0.36 mrad. It is even smaller for higher energies.

3.2 Beam screen photoemission properties

Photoemission from the LHC beam screens was extensively studied with dedicated measurements between 1998 and 2004 [48, 49, 51, 50]. A summary of their main results is given here. The following notation is used in most of them: R is the photon reflectivity of the material, and Y, Y^* are the photoelectron yields per incident and absorbed photon, respectively. They are defined as follows, where N_e is the number of photoelectrons and the n_γ the number of photons with sufficient energy to participate in the photoelectric effect:

$$n_{\gamma,\rm incident} = n_{\gamma,\rm absorbed} + n_{\gamma,\rm reflected} \tag{3.17}$$

$$R = \frac{n_{\gamma,\rm reflected}}{n_{\gamma,\rm incident}} \tag{3.18}$$

$$Y = \frac{N_e}{n_{\gamma,\rm incident}} \tag{3.19}$$

$$Y^* = \frac{N_e}{n_{\gamma,\rm absorbed}} = \frac{Y}{1-R} \tag{3.20}$$

Surface	Status	45 eV R (%)	45 eV Y* (e/ph)	194 eV R (%)	194 eV Y* (e/ph)
Cu co-lam.	as-received	80.9	0.114	77.0	0.318
	air baked	21.7	0.096	18.2	0.180
Cu elect.	as-received	5.0	0.084	6.9	0.078
Cu sawtooth	as-received	1.8	0.053	-	-
	150°C, 9h	1.3	0.053	1.2	0.052
	150°C, 24h	1.3	0.040	1.2	0.040

Figure 3.2: Three different copper samples were irradiated by synchrotron radiation profiles with different critical energy (see also Fig. 3.1). These are characterized by their critical energy, 45 eV and 194 eV correspond to radiation by protons in the LHC at 7 TeV and 11.5 TeV (Eq. 3.3). 194 TeV corresponds to 11.5 TeV protons in the LHC. Photoemission properties for different materials when irradiated with different synchrotron radiation profiles, characterized by their critical photon energy [48].

In [48], measurements that were performed at the Electron Positron Accumulator (EPA [55]) at CERN are reported. The properties of several materials were studied using synchrotron radiation from this machine, including co-laminated Cu and Cu with a sawtooth structure. It was possible to measure the reflectivity (only in the forward direction), as well as the photoelectron yield Y^*. The results are shown in Fig. 3.2.

A different experiment [49] quantified the effect of photon-induced conditioning on the photoelectron yield of co-laminated copper with sawtooth. Figure 3.3 shows the results. Photon scrubbing with a dose of $1.5 \cdot 10^{22}$ photons, corresponding to about 600 hours of nominal LHC operation, caused a decrease of the photoelectron yield by roughly

	45 eV		194 eV	
Dose (ph/m)	R (%)	Y* (e/ph)	R (%)	Y* (e/ph)
~ 2 10^{19}	8	0.029	7	0.040
1.5 10^{22}		0.015		0.022

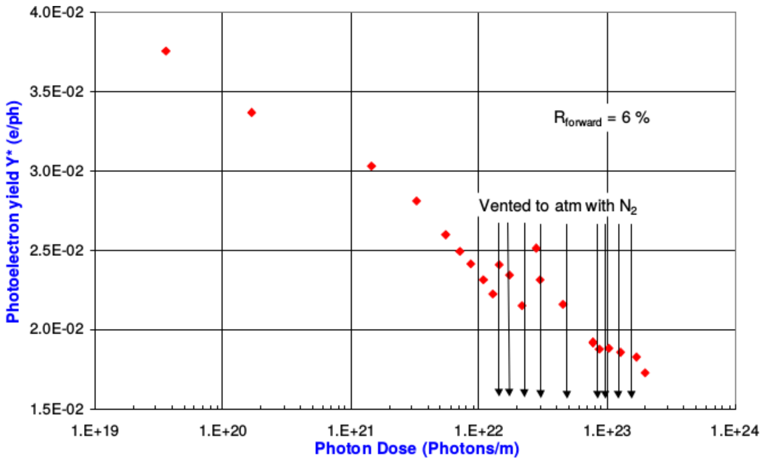

Figure 3.3: Left: reflectivity and photoelectron yield from measurements of copper samples with sawtooth structure. Right: the impact of photon scrubbing on the photoelectron yield. Both results were published in [49]

50%. The results indicate that this process had not saturated and could have possibly decreased the yield even further given an increased photon dose. No effect of photon scrubbing is observed on the photon reflectivities. One can note that this experiment measured larger photon reflectivities with respect to the results reported in [48].

The angular distribution of reflected photons is studied in detail in [50]. Copper samples with and without sawtooth structures were irradiated with synchrotron light between 8 eV and 200 eV at grazing incidence, and the reflectivities in different directions were measured. The critical energy of the radiation profile was 44 eV, again similar to the one emitted from 7 TeV LHC proton beams. The main results are shown in Fig. 3.4. Most reflected photons are scattered in forward direction in case of the flat Cu sample. For the sawtooth Cu sample, the overall reflectivity is strongly reduced, and more photons are scattered backwards. One has to note that higher reflectivities of the sawtooth sample (10%) are observed than in [48, 49] (1.8% and 8%).

The comprehensive paper [51] covers many aspects that are in connection with photoemission properties relevant for accelerators. Among these are the kinetic energy spectra of photoelectrons, the angular spectra of photoemission and the dependency of photoelectron yields on photon energy (see also Fig. 3.13). Furthermore, also the total photoemission yields and how these are affected by photon-induced conditioning is reported (see Fig. 3.5). Several materials used for accelerator technology were studied including copper, although only without a sawtooth structure. One has to note that, unlike in the previously mentioned measurement campaigns, the reflectivities were not measured. The photoelectron yields therefore correspond to yield per incident photons, Y. The published yields tend to be higher than those presented in [48, 49]. Furthermore, the incidence angle of photons was 45°, compared to a 11 mrad (0.63°) grazing incidence in case of [48, 49].

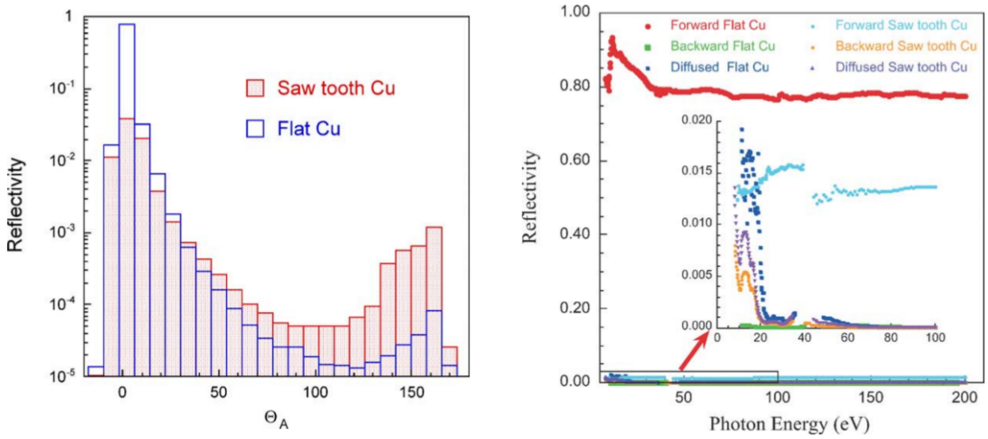

	Flat sample	Saw-tooth sample
Forward scattering (%)	80	4
Back scattering (%)	0	2
Diffused (%)	2	4
Total	82	10

Figure 3.4: Left: Measured reflectivity of Cu samples for incoming light at grazing incidence (26 mrad). The reflected photons were measured at different angles. A low value of Θ_A corresponds to forward reflection. Right: The reflectivities depending on the photon energy. Bottom: Summary of reflectivities for a LHC-type spectrum. These graphics were published in [50].

Sample	Low dose WL yield (electrons/photon)	Energy window low dose WL yield (electrons/photon)	WL yield (electrons/photon)	Energy window WL yield (electrons/photon)
Au	0.047 ± 0.020	0.022 ± 0.020	0.041 ± 0.002	0.023 ± 0.002
Cu	0.103 ± 0.020	0.051 ± 0.020	0.063 ± 0.002	0.042 ± 0.002

Figure 3.5: Measured white light (WL) photoelectron yields for Au and Cu [51] before (low dose WL yield) and after (WL yield) conditioning with synchrotron radiation with a spectrum similar to that emitted by LHC beams. The yield decreased by about 40% as a consequence of this conditioning. The other columns that are labeled "energy window" only take into account those electrons that have been emitted with a kinetic energy between 1 and 6 eV.

3.3 Simulation input parameters

The calculations and measurement results from Sec. 3.1 and 3.2 are converted to PyECLOUD input parameters in order to model the photoelectron seeding in build-up simulations.

We introduce the following notation, see also Eqs. 3.18-3.20:

Y_i, Y_i^*	Photoelectrons yields (defined by Eq. 3.19 and Eq. 3.20) in the region of direct impact of the synchrotron radiation (e.g. sawtooth region).
Y_r, Y_r^*	Photoelectron yields in the remaining part of the chamber.
R_i, R_r	Reflection rates in the region of direct synchrotron radiation impact and in the remaining part of the chamber, respectively.
N_i, N_r	Photoelectrons emitted in the region of direct impact of the synchrotron radiation and in the remaining part of the chamber, respectively.
N_t	Total number of emitted photoelectrons.
$n_\gamma(E > W_{\mathrm{Cu}})$	Number of photons with an energy above the copper work function, emitted per proton and m in the LHC arc bending magnets (Eq. 3.15).

In the PyECLOUD code the photoemission process is parametrized through the number of photoelectrons emitted per proton and per meter **k_pe_st**, and the fraction of photoelectrons emitted from reflected photons **refl_frac**. This means that (1-**refl_frac**) is the fraction of photoelectrons that is generated at the part of the beam screen where the synchrotron radiation first impacts. The calculation of **k_pe_st** requires knowledge of the beam energy, since $n_\gamma(E > W_{\text{Cu}})$ depends on γ_{rel} (see Eq. 3.15). In the following, $n_\gamma(E > W_{\text{Cu}})$ is computed for an LHC beam with an energy of 6.5 TeV.

In the case of uniform properties on the beam pipe surface, **k_pe_st** is computed as follows:

$$\textbf{k\_pe\_st} = n_\gamma(E > W_{\text{Cu}})\frac{Y}{1-R} = n_\gamma Y^* \tag{3.21}$$

The reflection coefficient is not needed since all photons are eventually absorbed, either on direct impact or after an arbitrary number of reflections, and the material properties are uniform.

However, if the region of initial impact has different properties, as in the case for the LHC beam screen with its sawtooth structure, the properties from both surface types must be taken into account. The number of photons that are absorbed at the sawtooth and after initial reflection have to be weighted with the respective photoelectron yields Y^* and the probability of initial reflection:

$$\textbf{k\_pe\_st} = N_i + N_r \tag{3.22}$$

$$= n_\gamma(E > W_{\text{Cu}})\big((1-R_i)Y_i^* + R_i Y_r^*\big) \tag{3.23}$$

$$= n_\gamma(E > W_{\text{Cu}})\big(Y_i + R_i Y_r^*\big) \tag{3.24}$$

Here the effect of photons that are reflected back to the sawtooth material is ignored, as this part covers only a small fraction of the total beam screen surface.

The quantity **refl_frac** is computed as follows:

$$\textbf{refl\_frac} = \frac{N_r}{N_t} = \frac{N_r}{N_i + N_r} = \frac{R_i Y_r^*}{(1-R_i)Y_i^* + R_i Y_r^*} \tag{3.25}$$

Source	Cu co-lam.			with sawtooth		
	R [%]	Y	Y^*	R [%]	Y	Y^*
Baglin et al. 1998 [48]	80.9	0.022	0.114	1.8	0.052	0.053
Cimino et al. 1999 [51]	-	0.103/0.063	-	-	-	-
Baglin et al. 2001 [49]	-	-	-	8	0.021/0.011	0.029/0.015
Mahne et al. 2004 [50]	82	-	-	10	-	-

Table 3.1: The different published experimental results on photoelectron yields and reflectivities are compared in this table. If two values are stated for a photoelectron yield, they correspond to measurements before and after photon scrubbing. The reflectivities colored in red only include the forward reflectivity. The yields in blue were not published but could be retrieved with the simple relation between R, Y and Y^* (Eq. 3.20).

Table 3.1 provides an overview of the results from the papers reviewed in the previous section. Y was calculated from Y^* and R in case of [51]. Since only the references [48, 49] include results for sawtooth materials, these publications are used to extract the parameters for electron cloud simulations. The reflectivities from [50] are chosen as they also include backward scattering of photons.

Two types of beam screens are considered, one with a sawtooth structure at the sawtooth where the synchrotron radiation directly impacts and another one with flat copper everywhere. For a **conservative estimate** (Tab. 3.2), a possible conditioning of the surfaces is not taken into account and the high photoelectron yields Y from [48] are used.

An **optimistic estimate** (Tab. 3.3) includes the lowest yields that can be constructed from the published results that were summarized in the previous section. Photon conditioning effects need to be included for both the material, in the sawtooth and elsewhere. This was quantified in [48, 49] for copper with sawtooth structures, in which case a reduction of the yield by a factor of 4.7 is observed (Y^* is 0.052 in [48] and 0.011 in [49] after conditioning). In the absence of published measurement results for smooth Cu after photon conditioning in [49], the same factor as for the sawtooth is applied in this case, obtaining:

$$Y = \frac{2.2 \cdot 10^{-2}}{4.7} = 4.6 \cdot 10^{-3} \tag{3.26}$$

Chamber type	R_i	R_r	Y_i	Y_r	Y_i^*	Y_r^*
Cu co-lam. with sawtooth	10.0	82.0	5.2e-02	2.2e-02	5.8e-02	1.2e-01
Cu co-lam.	82.0	82.0	2.3e-02	2.3e-02	1.3e-01	1.3e-01

Chamber type	N_i	N_r	N_t	n_γ	refl_frac	k_pe_st
Cu co-lam. with sawtooth	5.2e-02	1.2e-02	6.4e-02	1.1e-02	1.89e-01	7.00e-04
Cu co-lam.	2.3e-02	1.0e-01	1.3e-01	1.1e-02	8.20e-01	1.38e-03

Table 3.2: The yields and reflectivities from Tab. 3.1, together with the number of photons from Eq. 3.15, lead to a conservative estimate of the PyECLOUD input parameters refl_frac and k_pe_st..

Chamber type	R_i	R_r	Y_i	Y_r	Y_i^*	Y_r^*
Cu co-lam. with sawtooth	10.0	82.0	1.0e-02	4.6e-03	1.1e-02	2.6e-02
Cu co-lam.	82.0	82.0	4.6e-03	4.6e-03	2.6e-02	2.6e-02

Chamber type	N_i	N_r	N_t	n_γ	refl_frac	k_pe_st
Cu co-lam. with sawtooth	1.0e-02	2.6e-03	1.3e-02	1.1e-02	2.03e-01	1.39e-04
Cu co-lam.	4.6e-03	2.1e-02	2.6e-02	1.1e-02	8.20e-01	2.81e-04

Table 3.3: Photon scrubbing effects are considered to arrive at a more optimistic estimate with lower electron yields.

A python module using the formulas Eq. 3.1-3.16 as well as the material properties from Tabs. 3.2 and 3.3 has been developed [56]. It can be used to generate the input parameters refl_frac and k_pe_st (Eqs. 3.24 and 3.25) given the necessary beam and surface properties. The beam energy is only considered in the calculation of $n_\gamma(E > W_{\mathrm{Cu}})$ (Eq. 3.15). The dependence of R and Y^* on the radiation spectrum, which in turn depends on the beam energy, is unknown and therefore neglected. It shall be noted that the references [48, 49, 50, 51] all used a synchrotron radiation spectrum that is very similar to the one from the LHC running at 7 TeV. Results for 11.5 TeV beams (see Fig. 3.2 and 3.4) are significantly different. The radiation spectra for 6.5, 7 and 11.5 TeV are compared in Fig. 3.1.

3.4 Simulation results and predicted heat loads

PyECLOUD build-up simulation studies have been performed for all relevant magnetic elements and for the drift sections of the LHC arcs. Each of these magnets is simulated either with photoemission seeding or starting with a uniform initial distribution of 10^7 electrons per meter. Such an initial population is small with respect to the densities that are reached in simulations above the multipacting threshold. The magnetic lengths and the operational magnetic field parameters of the simulated devices operating at a beam energy of 6.5 TeV are shown in Tab. 2.1.

For all considered magnetic elements, simulations have been performed with the conservative estimates for the photoemission parameters (see Tab. 3.2). The simulated beam consists of two trains of 288 bunches, each formed by four batches which in turn consist of 72 bunches. The two trains are interleaved with 30 empty bunch slots, and the consecutive batches are interleaved with eight empty slots. The bunch intensity is set to $1.1 \cdot 10^{11}$ p/bunch. The corresponding heat loads are shown in Fig. 3.6. The heat load from the second train is rescaled in order to obtain the heat load that corresponds to a filled LHC machine with 2800 bunches in total, without having to simulate each train. This procedure is chosen since the electron cloud in the second and later trains are identical in case the electron density is saturated by the end of every train, a condition that is usually satisfied as shown in Fig. 3.7. The right axes in Fig. 3.6 correspond to the heat load scaled to the length that each element has in the average cryogenic cell of the LHC arcs, as reported in Tab. 2.1.

It becomes clear that only drifts and dipoles (including the corrector magnets) are notably affected by the choice of seeding parameters, while there are only minor differences for higher order magnets. For the sensitive elements, also the optimistic parameters from Tab. 3.3 have been used in another set of simulations. The multipacting thresholds, characterized by a rapid increase in heat load after a certain value of the secondary emission parameter (SEY or $\delta_{\max}$), can be clearly identified.

This threshold is significantly altered by the photoelectrons in the case of the drift space. In this particular case where the electrons can move freely in the chamber, the photoelectrons from the whole surface can contribute to the electron cloud build-up, including those generated by the direct impact of the synchrotron radiation at the side of the beam screen.

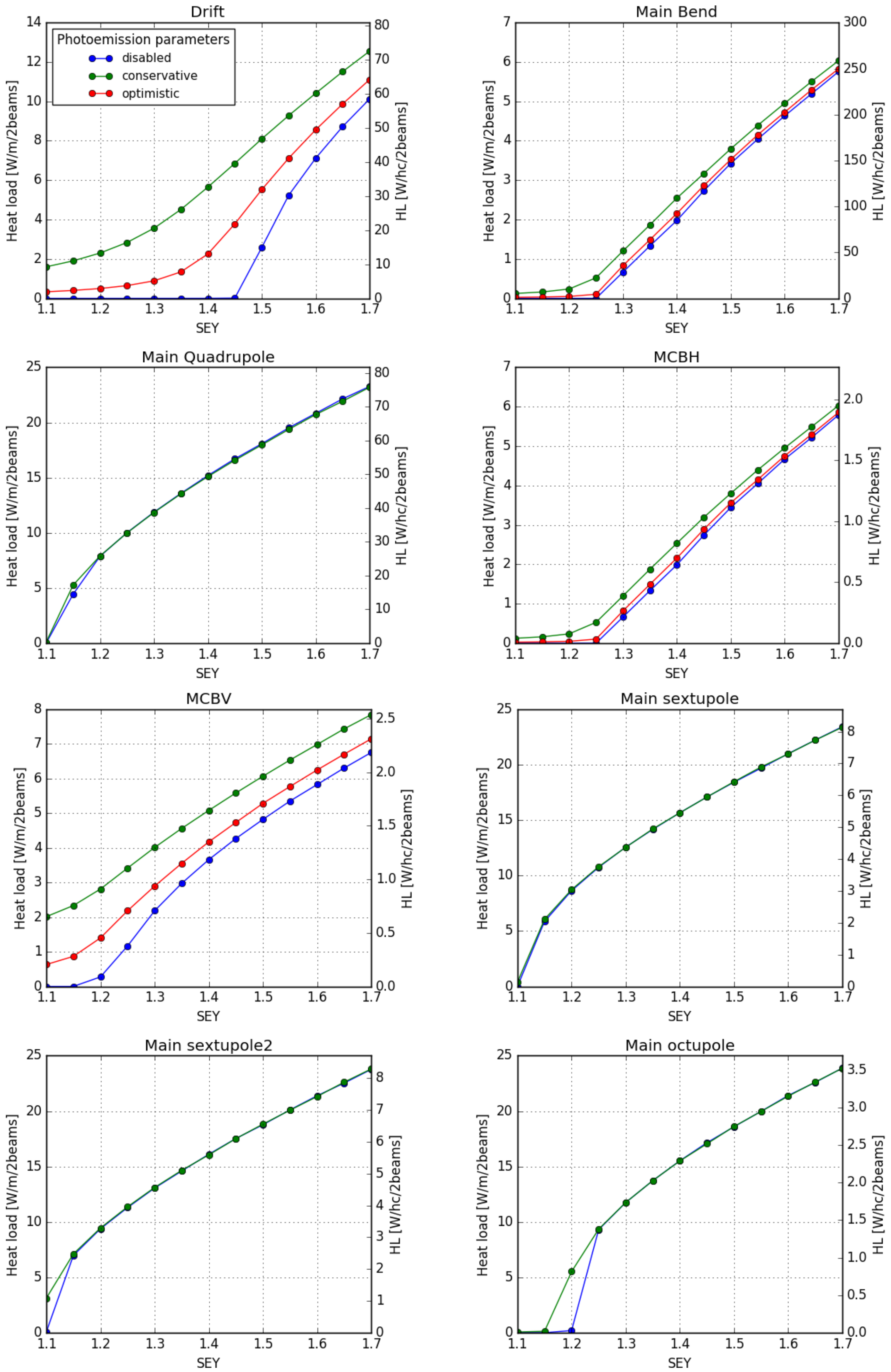

Figure 3.6: Heat loads from PyECLOUD simulations with "conservative" photoemission parameters derived in Sec. 3.3 and magnetic field parameters from Sec. 2.1. In case of the drifts and dipole magnets (MB, MCBH, MCBV), also the "optimistic" parameters have been simulated. The left axes correspond to the heat load per meter, the right axes to the heat load in the average cryogenic cell.

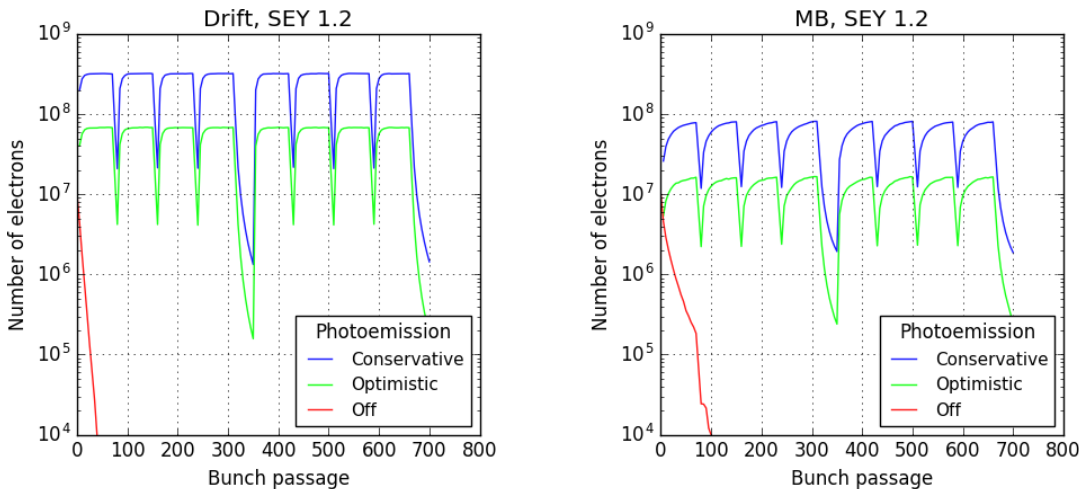

Figure 3.7: The evolution of the number of electrons per meter in the chamber of a drift and a dipole as obtained from PyECLOUD simulations with an SEY parameter of 1.2. The different electron cloud seeding mechanisms are compared.

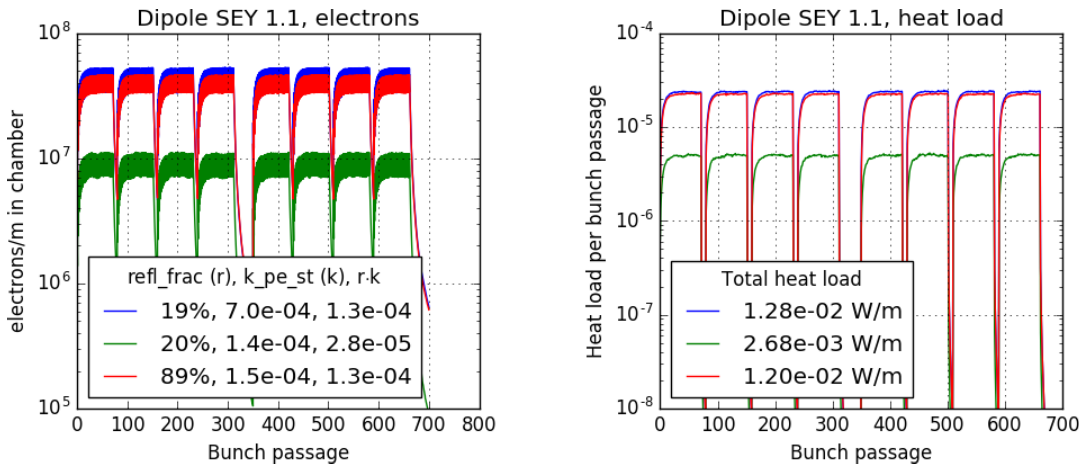

Figure 3.8: The total number of electrons in the chamber and the heat loads from three simulations with different photoemission parameters are compared. The reference simulations utilize the conservative estimates (blue) and optimistic estimates (green) from Tab. 3.2 and 3.3. For the other simulation (red), k_pe_st has been decreased by a factor of 4.7 with respect to the conservative case, while refl_frac has been increased by the same factor. The product of refl_frac and k_pe_st is the number of photoelectrons from reflected photons per proton and meter.

For all other magnet types, only the photoelectrons generated in the characteristic stripes (Fig. 2.5) contribute significantly. To validate this explanation, three simulations of an LHC dipole and 288 bunches were run with different k_pe_st and refl_frac parameters, see Fig. 3.8. Even though the total number of photoelectrons is determined by k_pe_st, it is clear that k_pe_st·refl_frac, corresponding to the photoelectrons from reflected photons, is more important for the total electron numbers and deposited heat loads. This means in turn that the photoelectrons generated at the side of the beam screen are of little importance in this case.

For each of the LHC arc half-cells the heat load deposited on the beam screens can be estimated from the measured thermodynamic parameters of the cooling fluid (e.g. temperatures, pressures). For standard arc cells, the installed sensors only allow measuring the total heat load over the two 53 m long beam screens, while it is not possible to disentangle the effect of the single magnets nor of the single beam.

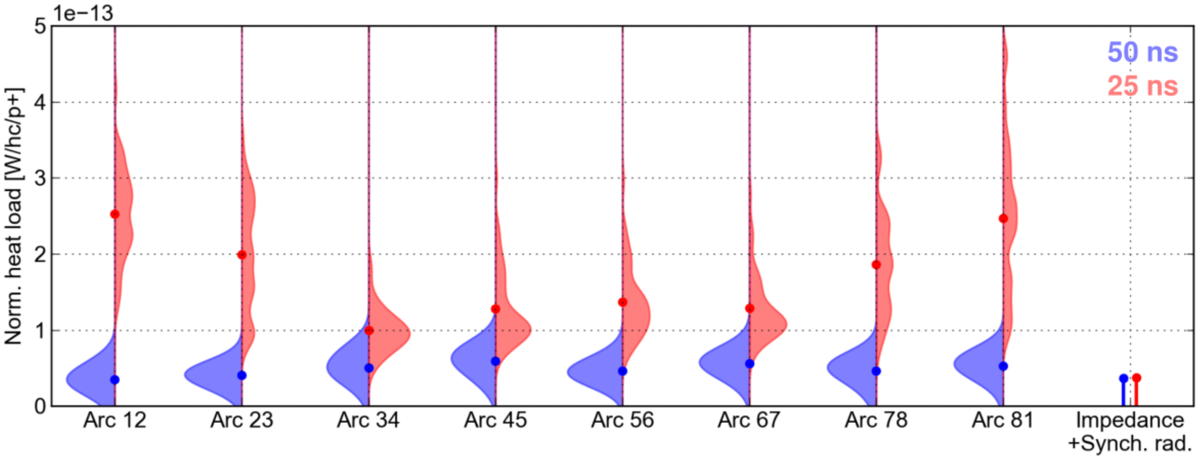

Figure 3.9: Top: distribution and average of the normalized heat loads (i.e. divided by the total intensity in the two LHC beams) in the cryogenic cells of the eight LHC arcs, measured at high energy during physics fills with 25 ns and 50 ns bunch spacing. Bottom: main beam parameters during the two fills [38].

Figure 3.9 shows the cell-by-cell heat load distributions measured at high energy in the eight LHC arcs during physics fills with two different bunch spacings [38]. The data is normalized by the total intensity in the ring. The average bunch intensities and bunch lengths for the two fills were very similar.

One can observe that with 50 ns bunch spacing the eight arcs behave very similarly and that the average heat load is compatible with the expectation from impedance and synchrotron radiation. This confirms that with this large bunch spacing there is no significant heating from e-cloud effects.

The situation is very different with 25 ns bunch spacing. In all sectors the average measured heat loads are significantly larger than the expectation from impedance and synchrotron radiation, which indicates the presence of a significant heat contribution from the e-cloud. Moreover, the different sectors show significant differences both in the average measurement and in the spread observed in the values. These features were first observed in 2015, at the start of operation with 25 ns beams after the 2013-14 Long Shutdown (LS1) and stilll persist in spite of the beam scrubbing accumulated in the period 2015-2017. The origin of these differences is not clear and is presently under investigation [38].

In order to compare these data with the simulations presented in the previous section, the total heat load expected for the average arc half-cell was calculated. The contributions from impedance, synchrotron radiation (computed using the HeatLoadCalculators tool [39]) and e-cloud from the different elements are summed up. This is done by assuming that all beam screen surfaces in the half-cell have the same SEY. As before, three configurations for the photoemission are considered: uniform initial seeding with no photoemission, conservative and optimistic surface parameters as described in Sec. 3.3.

It can be observed that, especially when taking into account the effect of photoelectrons, the lowest observed heat load values are compatible with an almost full suppression of the multipacting process (SEY<1.2). The highest observed values in Sectors 12, 23, 78 and 81, instead, correspond to SEY parameters in the range 1.4 to 1.5.

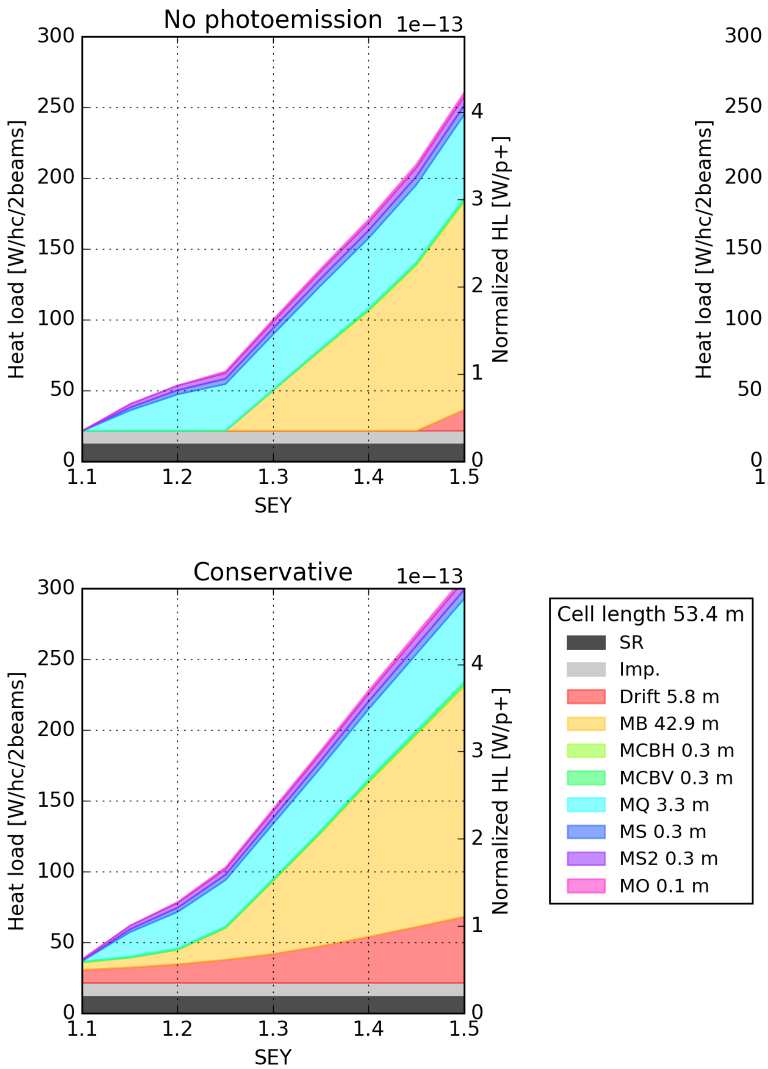

Figure 3.10: Total heat load in the average LHC half cell as a function of the SEY parameter of the beam-screen surface (assumed to be the same over the intire half-cell). The different contributions are shown in different colors. Three configurations for the photoemission are considered: uniform initial seeding with no photoemission, conservative and optimistic parameters as described in Sec. 3.3.

Photoelectron yields and reflectivities are only a part of the photoelectron seeding model. In this section the impact of other, more general properties is investigated. Changes to the code have been introduced that optionally allow for variations of the initial energy of photoelectrons, as well as the times or locations at which they are generated in the chamber. The influence of these changes on the simulations is discussed in the following subsections.

In PyECLOUD, photoelectrons are generated with the same time structure as the longitudinal beam profile. In reality however, the two are not exactly synchronized due to the fact that the protons are bent by the magnetic field while the photons are not (see Fig. 3.11). The difference is calculated in the following equations, where R is the bending radius of

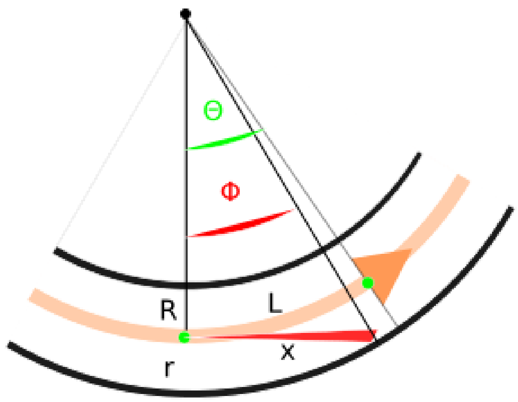

Figure 3.11: The path difference between protons (green) and photons(red). R and r are the bending and chamber radii, while L and x are respectively the paths the protons and the photons travel until the photon hits the chamber walls.

the LHC main dipoles (2803.95 m) and r (22 mm) is half of the chamber diameter, see Fig. 3.11. A beam travelling with the speed of light is assumed, therefore L and x are equally long by definition.

$$(R+r)^2 = R^2 + x^2 \tag{3.27}$$

$$x = \sqrt{2Rr + r^2} = 11.1 \text{ m} \tag{3.28}$$

$$\Phi = \tan^{-1}\frac{x}{R} \tag{3.29}$$

$$\Theta = \frac{L}{R} = \frac{x}{R} \tag{3.30}$$

The time-delay between the beam and the synchrotron radiation is given by:

$$\Delta t = \frac{R(\Theta - \Psi)}{c} = 1.938 \cdot 10^{-13}\, s \tag{3.31}$$

This difference is negligible as it is much smaller than a time step in the simulation, which is normally around 10^{-11} s.

Photons that are absorbed only after several reflections (note that the reflection coefficient for grazing incident photons on copper without sawtooth was measured to be larger than 80%, see Sec. 3.2) are delayed significantly with respect to the originating beam charge. One reflection to the opposite side of the chamber causes a delay of $\Delta t = \frac{2r}{c} = 1.48 \cdot 10^{-10}$ s, which is already longer than a time step in the simulations, but much shorter than the bunch spacing. Backward reflections however, which are expected for sawtooth surfaces, lead to delays that are in the order of the bunch spacing of 25 ns, for which a distance of travel of 7.5 m is required. This means that there is a seeding mechanism of build-up simulations that extends to the gaps between bunches, and could in principle alter the way the electron cloud decays.

To investigate the impact of the time structure of the photoelectron generation, a modified version of PyECLOUD has been utilized, in which photoelectrons are generated uniformly in time. The results are presented in Fig. 3.12 and compared to the usual PyECLOUD modelling. The heat loads are practically not affected by the changes, while the electron densities are only noticeably different in between trains, which has no effect on the electron cloud density seen by most of the circulating bunches. Therefore, changes to the code concerning the temporal distribution of emission are not deemed necessary.

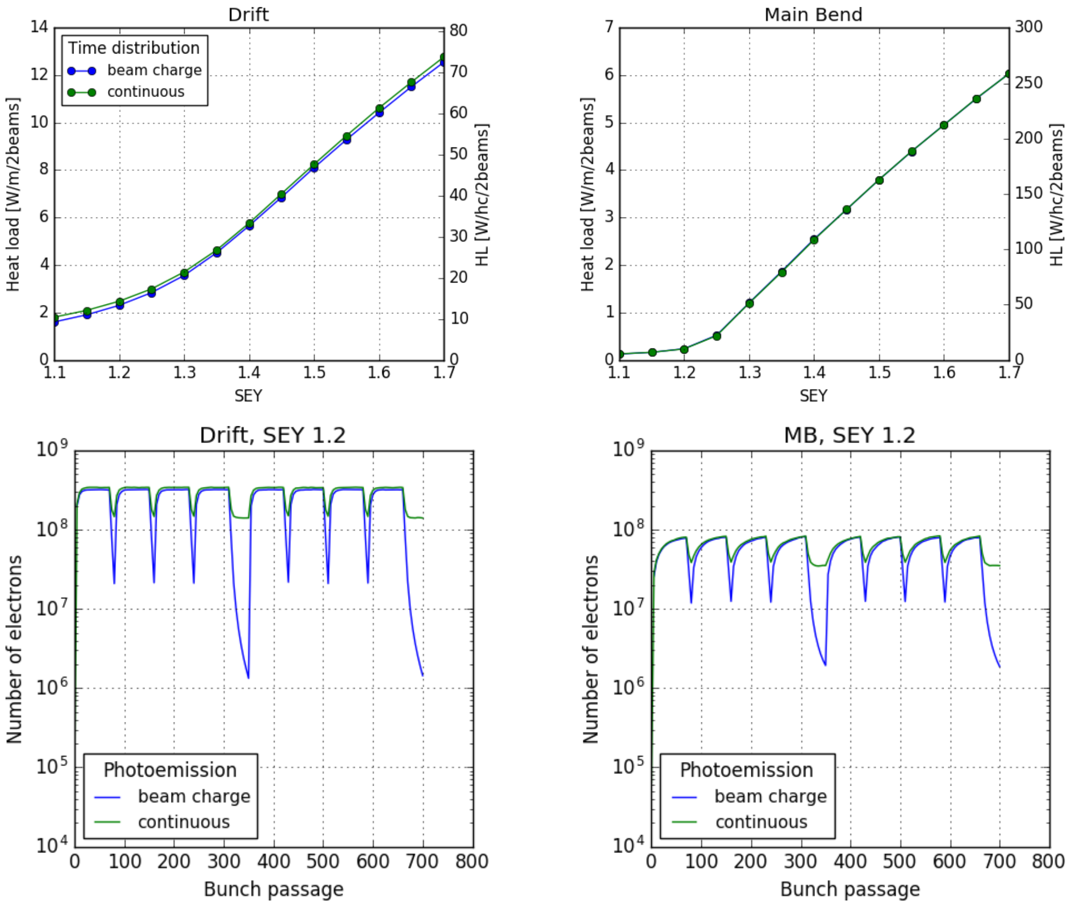

Figure 3.12: For drifts and dipoles, the effect of a generation of photoelectrons that is continuous in time is compared to the usual assumption, where the generation coincides with the beam charge profile. Both simulations use a uniform angular distribution of reflected photons, see also Fig. 3.16.

The energy of generated photoelectrons is not very relevant in the current implementation of PyECLOUD, as they are generated in parallel to the beam charge and immediately accelerated to much higher energies by the electric field. It could become more important in case of a photoelectron generation that also covers the time between bunches or even batches.

Currently a truncated Gaussian is used for the energy distribution in PyECLOUD simulations. According to laboratory measurements [51], different distributions are more realistic (see Fig. 3.13). Therefore, other distributions have been optionally introduced to the simulation code. These are specified by the new input parameter **energy_distribution**, which allows to choose from the following options (see Fig. 3.14):

- A truncated Gaussian, which is the standard in PyECLOUD. Negative energies are not allowed.

$$p(E) = \frac{1}{\sqrt{2\pi\sigma^2}} e^{-\frac{(E-\mu)^2}{2\sigma^2}} \tag{3.32}$$

- a Lorentzian, truncated to positive values as indicated by Fig. 3.13. However it only fits well for the low-dose sample, otherwise the low-energy part is greatly reduced.

$$p(E) = \frac{1}{\pi} \frac{\sigma}{\sigma^2 + (E-\mu)^2} \tag{3.33}$$

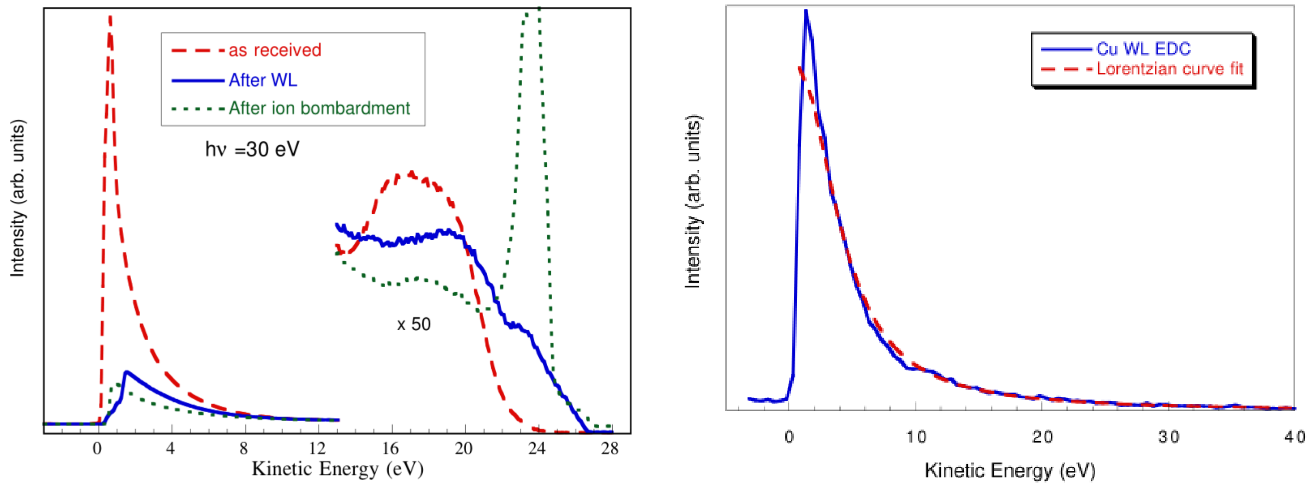

Figure 3.13: Left: The photoemission spectra for 30 eV photons on copper [51]. The blue curve corresponds to a state after white light (WL) scrubbing has been performed, it is similar to the spectrum after a surface cleaning with ion bombardment. Right: A Lorentzian fit to the energy spectrum before white light scrubbing, when the material is exposed to broadband synchrotron radiation (also dubbed white light in [51]).

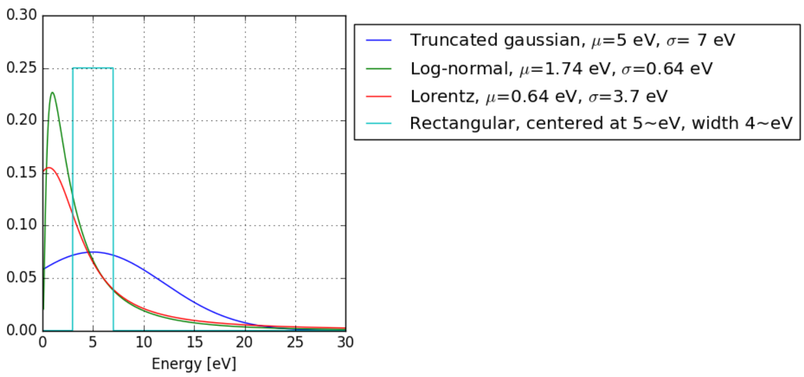

Figure 3.14: This plot shows a truncated normal distribution, as well as a log-normal distribution (Eq. 3.34) with the same mean and variance as the undistorted Gaussian distribution (note that μ, σ in Eq. 3.34 are not the mean and standard deviation). In addition, also a Lorentzian with the parameters from Fig. 3.13 (right) [51] and a rectangular distribution are shown.

- A log-normal distribution, which could probably also be fitted to the data in Fig. 3.13. One advantage is that it does not have to be truncated, as negative energies cannot occur.

$$p(E) = \frac{1}{E\sigma\sqrt{2\pi}}\, e^{-\frac{(\ln E-\mu)^2}{2\sigma^2}} \tag{3.34}$$

  It shall be noted that μ and σ are simply parameters and not the mean and standard deviations of the distribution.

- A rectangular or a mono-energetic distribution in order to study the sensitivity when an unphysical distribution is utilized.

Figure 3.15 shows a comparison of the resulting heat loads for different energy distributions, as well as the electrons in the chamber at various time steps in simulations of drift spaces. The parameters used for the distribution functions are as in Fig. 3.14. The simulations were performed with a generation of photoelectrons that is uniform in time. Nevertheless, the initial energy of the photoelectrons does not have any impact on the resulting heat loads. [h]

In this subsection the impact of the distribution of absorbed photons, and therefore the positions of new macroparticles, is studied. The different investigated models are listed below. The definition of the angles Ψ and θ is sketched in Fig. 3.16, while N_r and N_i are defined in Sec. 3.3.

1. A $\cos^2(\Psi)$ distribution of N_r and a very narrow Gaussian distribution of N_i (defined through θ) at the corner of the beam screen. This distribution has also been used in simulations with the ECLOUD code, a predecessor of PyECLOUD [20].

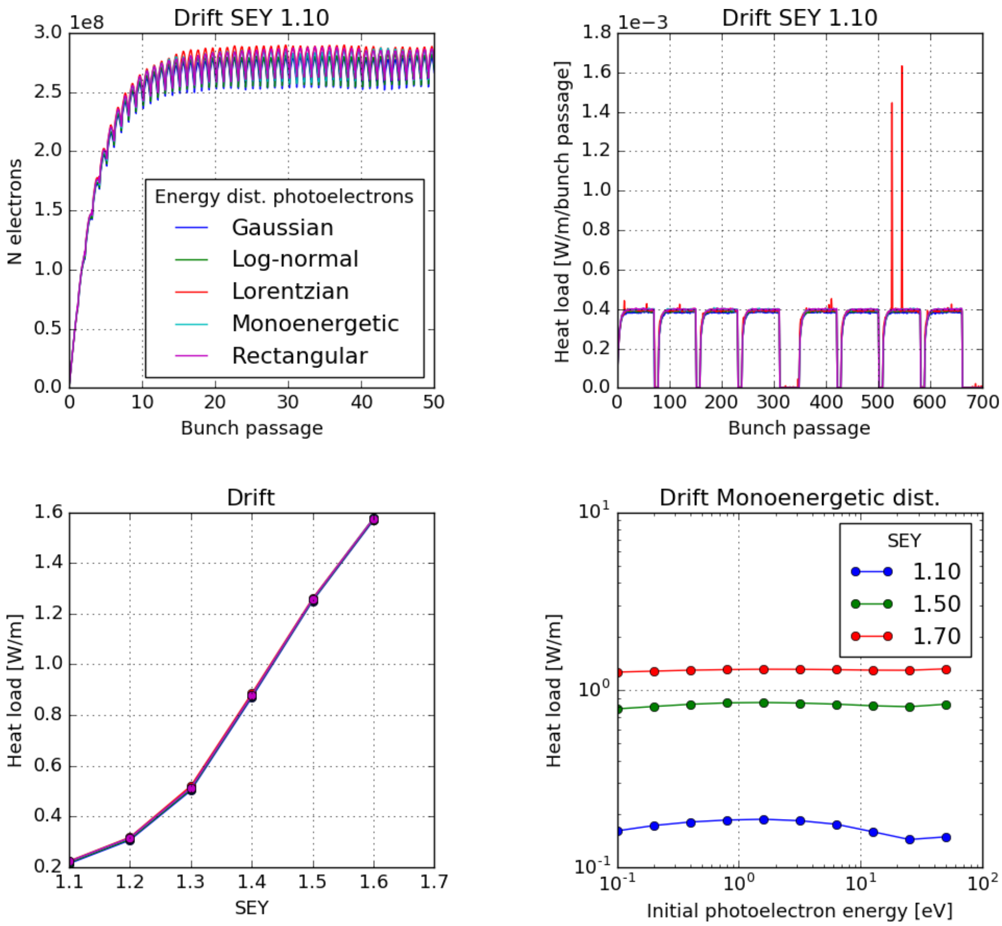

Figure 3.15: The impact of several different energy distributions of emitted photoelectrons is investigated by simulating a drift with different energy distribution functions. Top left: the number of electrons for different bunch passages. Top right: the heat load per bunch passage of the same simulations. The spikes correspond to the usage of the Lorentzian, which occasionally leads to the generation of extremely high energy photoelectrons. Bottom left: the heat loads at different values of the SEY parameter. Bottom right: the heat loads for three different SEY values when the initial energy of photoelectrons is varied between 0.1 eV and 50 eV.

2. A uniform distribution of N_r (defined through Ψ in Fig. 3.16) and again a Gaussian distribution as above for N_i.
3. A distribution where the distinction between N_i and N_r is abandoned and the input parameter refl_frac is unused. The angular distribution of the photoelectrons with respect to the center of the chamber (θ) is uniform in the simulated case

The option to model the distribution as in the variant 3 has been included to the PyECLOUD code over the course of this work. It is possible to define the angular distribution (defined as θ in Fig. 3.16) in a file supplied by the user, which is read at runtime of the simulation. In future studies it will be possible to use the results of dedicated simulations of photon paths and absorption points as an input for PyECLOUD. Some results have already been published [57], using the simulation software Synrad3D developed at Cornell University [58], they are however not yet ready to be used [59]. Another suitable software would be Synrad+, developed at CERN [60, 61].

The three aforementioned variants have been simulated, the resulting heat loads are shown in Fig. 3.17 for dipoles and drift spaces and SEY parameters between 1.1 and 1.7 at a nominal beam intensity ($1.1 \cdot 10^{11}$ p/bunch). The total number of photoelectrons, as computed from the parameter k_pe_st (see Sec. 3.3), was identical.

In case of the drift space, all of these three implementations yield very similar heat loads, which is not surprising since the electrons can move freely in the chamber due to the absence of strong magnetic fields. In case of the dipole however, it becomes clear that the uniform distribution of all photoelectrons enhances the electron cloud. On the other hand, the two choices that change the location of only those photoelectrons that are generated from reflected photons yield an identical result.

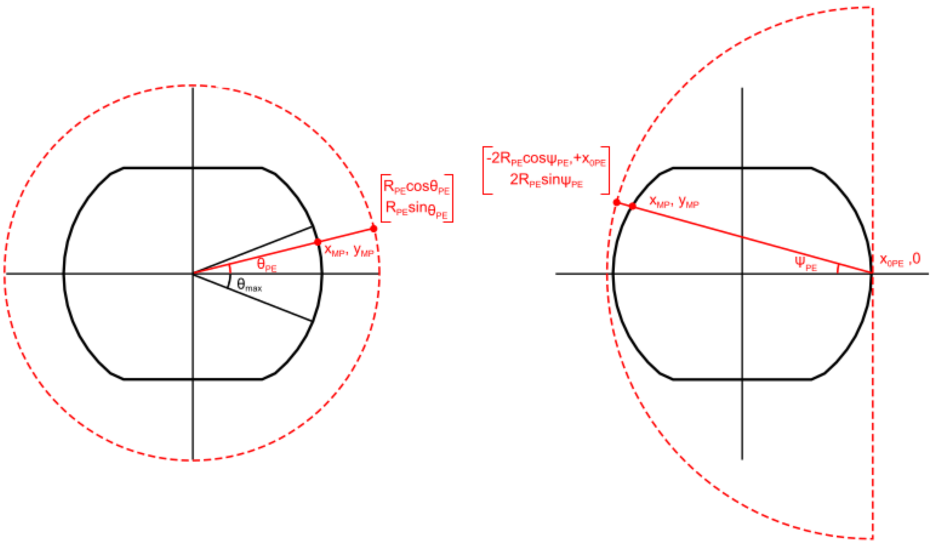

Figure 3.16: The angular distribution of photons is modelled in PyECLOUD using the angles θ and Ψ. The photoelectrons generated from reflected photons are using a distribution depending on Ψ, measured from the corner of the beam screen. The photoelectrons generated from non-directed photons are distributed as a function of θ, measured from the center of the beam screen.

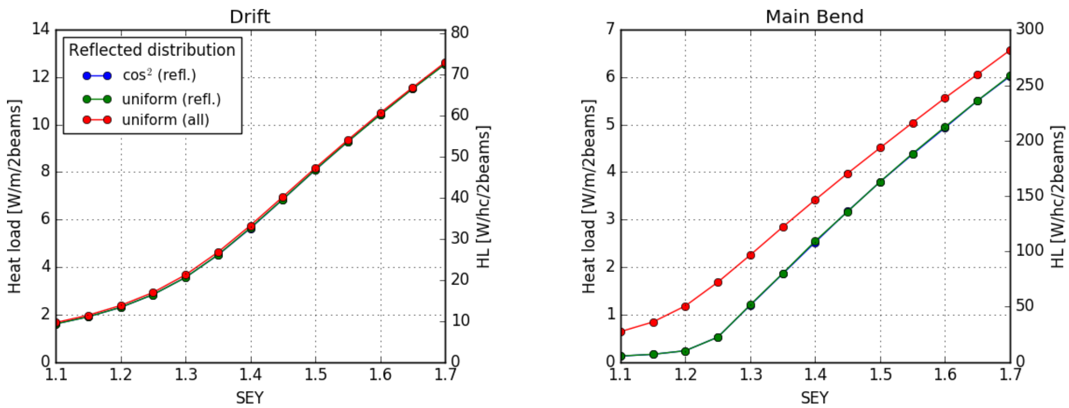

Figure 3.17: Three different distributions of reflected photons on the walls of the beam screen are simulated. No effect on the simulation results is observed in case

Over the course of this project, significant progress was made in terms of the analysis of electron cloud induced heat loads measured at the LHC, as well as electron cloud build-up simulations. As part of the master thesis proposal, a systematic scan of secondary emission parameters was performed. It was shown that PyECLOUD simulation results are very sensitive to most of them. The calculation of the heat loads at the LHC cryogenic cells was reimplemented and improved. A conveniently accessible database of heat loads and beam parameters of the LHC in run 2 (2015-present) was built. The subsequently performed data analysis has proven as very useful.

The PyECLOUD simulation code has been improved in various ways over the course of this work. A misconception has been identified in the implementation of the $\cos\theta$ distribution for the secondary electrons. The issue has been resolved, and the impact is discussed in the appendix of this report.

Moreover, arbitrarily high multipoles and combinations of different magnet types (compound magnets) are now supported. An electron cloud study on sextupoles and octupoles has thereupon been performed. The simulation results feature some similarities between e-cloud effects in quadrupoles and sextupoles, while the cloud appears to be weaker in octupoles. These elements do therefore not pose a greater risk to beam operation than quadrupoles, which have already been extensively studied before. At the same time, the combined length of the quadrupoles in the LHC is much higher that that of any higher order magnet. It is therefore not deemed necessary to include these elements in every future electron cloud study.

A comprehensive study of simulations with photoemission seeding was conducted. Input parameters were derived from basic equations on synchrotron radiation as well as published measurement results of the surface properties of beam screen materials. Two different kinds of parameters to model the photoemission seeding are obtained. One of them is a conservative estimate which features high numbers of photoelectrons, and corresponds to measurements of clean, "as-received" samples of copper. The other is a more realistic one where photon induced conditioning of the surface is considered, which could be observed in dedicated laboratory measurements.

It was shown that photoemission seeding can significantly change the simulation results for drift spaces and dipoles. Therefore, this seeding mechanism should always be enabled when simulating those devices at high beam energies. A small module was coded which provides the input parameters that are related to photoelectrons. The findings of this study could also be relevant for future accelerators, since they feature higher beam energies and intensities and therefore emit also more photons. However it shall be reiterated that the parameters that were obtained from the literature correspond to the synchrotron radiation profile of the LHC at 7 TeV. The values of these parameters cannot be adopted for a beam that emits radiation with a vastly different profile.

A simulation study for all magnetic elements that occur in the average cryogenic cell was performed. Photoelectron seeding was enabled, using the parameters from the literature review. The simulated heat load of each device was scaled with its average length. This is therefore a predicted heat load based on the secondary emission model used in the software. A comparison to measured heat loads of all cryogenic cells allows to draw conclusions on the secondary emission parameter.

5.1 Emission angles of generated photoemitted and secondary electrons

The angular distribution of secondary electrons, as well as photoelectrons, is meant to follow a $\cos\theta$ distribution in PyECLOUD (see also Sec. 1.2). This distribution is defined in the following, where θ and φ are the azimuthal and polar angles, and $\mathrm{d}\Omega$ is the differential solid angle in spherical coordinates [20]:

$$\frac{\mathrm{d}n}{\mathrm{d}\Omega} \propto \cos\theta \tag{5.1}$$

$$\mathrm{d}\Omega = \sin\theta \ \mathrm{d}\theta \ \mathrm{d}\varphi \tag{5.2}$$

$$\int \frac{\mathrm{d}n}{\mathrm{d}\Omega} \ \mathrm{d}\Omega = 1 \tag{5.3}$$

Note that θ ranges between 0 and $\frac{\pi}{2}$ since the electron trajectories always point towards the inner side of the chamber. The resulting distribution of the emission angle θ is obtained by omitting the dependency on φ, which is uniform between 0 and 2π. The normalization of $\frac{\mathrm{d}n}{\mathrm{d}\theta}$ yields a factor of 2:

$$\frac{\mathrm{d}n}{\mathrm{d}\theta} = \frac{\sin\theta\cos\theta}{\int_0^{\pi/2} \sin\theta\cos\theta \ \mathrm{d}\theta} = 2\sin\theta\cos\theta = 2\sin(2\theta) \tag{5.4}$$

Unfortunately, the following distribution has been implemented in PyECLOUD, which is a common misconception in 2D codes [31]:

$$\frac{\mathrm{d}n}{\mathrm{d}\theta} = \cos\theta \tag{5.5}$$

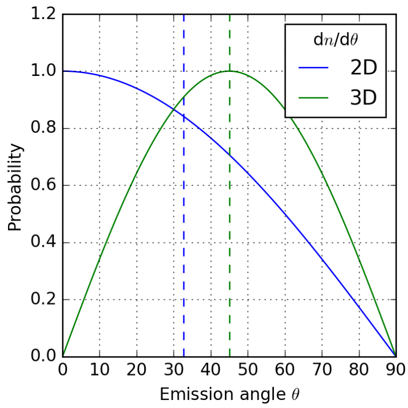

Figure 5.1: The cosine distribution, implemented correctly (3D) or incorrectly (2D). The dashed lines specify the average angles of emission.

The implications are shown in Fig. 5.1, where the correct case is labelled as 3D and the traditional behavior as 2D. In the 3D case, the probability of emission is significantly shifted to higher angles.

The 3D variant has been added to the code, currently the user has to specify optional input parameters to choose the emission angle distribution for electrons generated from secondary emission or photoemission processes. Currently, the default behavior has not been changed as to keep backwards compatibility. Starting in the near future however, an error will be raised if the user does not specify an angular distribution [62].

A simulation study was performed to estimate the impact of the angular distribution on simulations with nominal beam parameters. The investigated magnetic devices were drifts, dipoles and quadrupoles. Photoemission seeding was disabled, and a uniform initial distribution of electrons was used instead. Figure 5.2 show the impact of switching from the old to the new angular distribution in terms of several properties.

- The total heat loads of simulations with different δ_{max} parameters depends on the chosen distribution function for the emission angles. In most cases, the heat loads are decreased when switching from the old to the new implementation of the cosine distribution.
- The total number of electrons (Fig. 5.2) per time step is shown in order to see potential changes in the speed of the electron cloud build-up or the reached plateau. An decrease of this number is observed when switching to the correct angular distribution in case of the drift space, but there are only small changes for dipoles and quadrupoles.
- The central electron density is most important for investigations of instabilities, tune shifts or other effects the electron cloud may have on the beam. It is defined as number of electrons in the sphere that is defined by a radius of 0.1 mm around the middle of the chamber divided by its volume. The code changes led to an increase of the density in drift simulations, but barely affected in quadrupole simulations. The latter device is most critical, since the central electron density and thereby also the perturbation of the beam is much higher than in drifts and dipoles.

- The histogram of deposited energies is important to understand the spatial distributions of the electron cloud in the chamber. The x coordinates and energy of the electrons that hit the surface are stored. This is similar to the density profiles shown in Fig. 2.5, but one-dimensional. No significant changes can be observed for dipoles and quadrupoles.
- The effect of the emission angle distribution on the observed angles of impact is shown in Fig. 5.3. The impact angles are also shifted to higher values in all cases, thereby increasing the secondary electron yield as specified in Eq. 1.4.

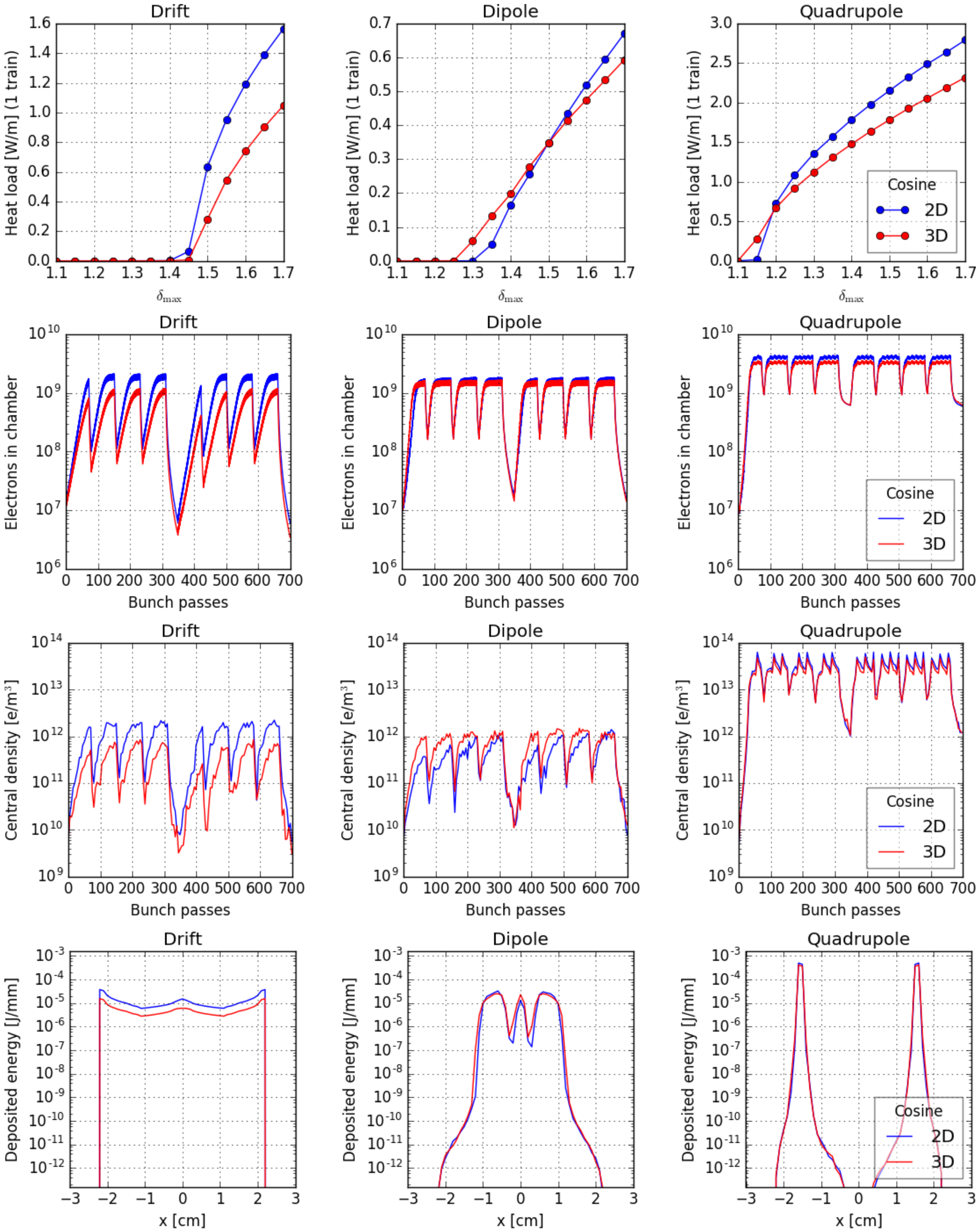

Figure 5.2: The consequence of choosing one of the two different emission angle distributions is studied. The δ_{max} parameter was set to 1.5 in these simulations. These are explained in Fig. 5.1 and Eq. 5.4 and 5.5. For drifts, dipoles and quadrupoles, the total number of electrons, the total kinetic energy and the heat loads per bunch passage are compared.

In the master thesis proposal [1], a sensitivity study was performed for some of the parameters that are used for the modeling of secondary electron emission in PyECLOUD. These included a factor A that has been introduced to model the dependence of $\delta_{\max}$ on the incidence angle θ:

$$\delta'_{\max}(\theta, A) = \delta_{\max}\, e^{A\frac{(1-\cos\theta)}{2}} \tag{5.6}$$

Normally, A is set to 1 as in Eq. 1.4. In a simulation study, A has been varied between 0 and 2, where the corner cases correspond to a removal (0) and a vast increase (2) of the θ dependency. The effect of A on $\delta(E,\theta)$ is shown in Fig. 5.3 (top). The bunch intensity was fixed at $1.1 \cdot 10^{11}$ p/bunch, and the beam consisted of 288 bunches.

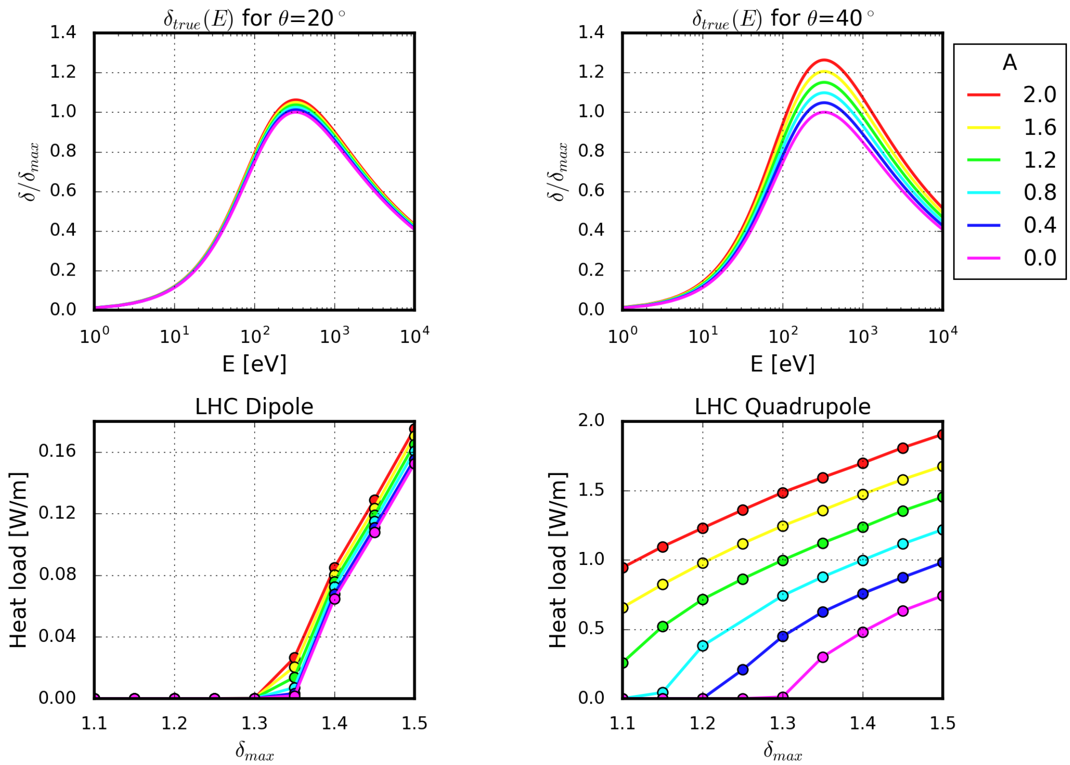

Figure 5.3: Top: The secondary emission curves $\delta(E,\theta)$ (Eq. 1.3) for different values of the parameter A (introduced in Eq. 5.6). The bottom plots show the effect on the heat loads. This plot was also part of the master thesis proposal [1].

The resulting total heat loads are shown in Fig. 5.3 (bottom) for a simulated dipole and quadrupole field, they are scaled with the revolution frequency of the LHC. It is noticeable that the impact of A is extremely strong on the quadrupole heat loads, while it is relatively small on the dipole heat loads.

In order to investigate this behavior, the cosine of the incidence angles of all impinging electrons have been added to the stored simulation results. This was not yet available when the master thesis proposal was finalized. In Fig. 5.4, these are shown in normalized histograms for three devices and the two different distributions of emission angles that are implemented in PyECLOUD. In both of these cases, the mean angle of incidence is highest for the quadrupole, whereas dipole and drift devices are similar. This was expected from the results as shown in Fig. 5.3.

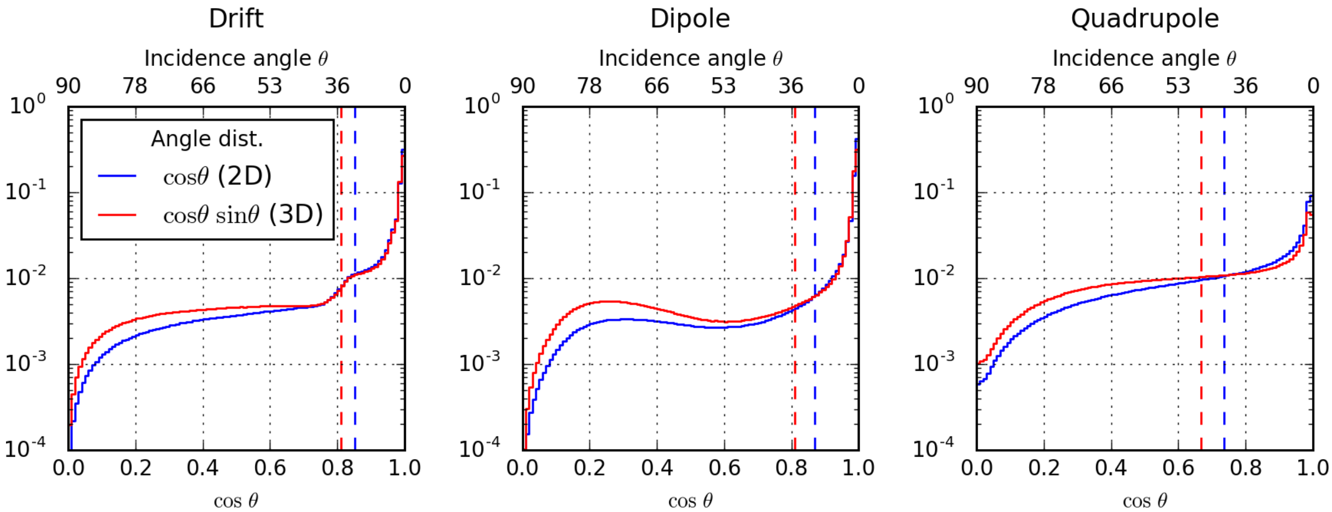

Figure 5.4: The cosine of the incidence angle of all impinging electrons has been saved for simulations of three different devices. The dashed lines correspond to the average incident angles. The simulations were performed with a $\delta_{\max}$ value of 1.5. The two curves in each plots relate to the distribution of emission angles (see Sec. 1.2 and 5.1).

Acknowledgements

It has been a great honor and privilege to write my master thesis at CERN.
First and foremost I would like to thank Giovanni Iadarola who supervised me over the course of this year. He has always provided excellent support and guiding. We had discussions multiple times per week, and spent a lot of time together working on the code and the data analysis.
I thank my university tutor Oliver Boine-Frankenheim for giving me the possibility of working in this interesting field, as well as the discussions of my work.
I am indebted to Rüdiger Schmidt, his lectures at TU Darmstadt sparked my interest in accelerator physics while I was still an undergraduate student. He also agreed to overtake the task of the second referee for this thesis.
I am grateful to Benjamin Bradu, who has provided excellent support on the heat load recalculations and helped me understand the basics of the LHC cryogenics. This important part of the work would not have been possible without him.
I would like to thank Lotta Mether for her help on data analysis and the discussions on photoemission simulations.
It has been a pleasure to attend the section meetings chaired by Elias Métral. He has always been supportive and interested in my work.
I thank Annalisa Romano, who has supported me especially in the first months of the previous year where I still had to find myself. She has also helped me in preparing the presentations I gave over the course of this work.
I would like to thank Giovanni Rumolo for the fruitful discussions on electron cloud effects, where I could profit from his deep understanding of this matter.
I am especially grateful to Giovanni Iadarola, Giovanni Rumolo, Frank Zimmermann and Guiliano Franchetti (GSI) for allowing me to attend the EuCARD workshop in Karlsruhe in March 2017. Furthermore I could also attend the MULCOPIM'17 conference together with Giovanni Rumolo in April.

[1] P. Dijkstal, "Electron cloud buildup simulations for the LHC." Master thesis proposal, https://indico.cern.ch/event/605497/, 2017.

[2] The ATLAS Collaboration *et al.*, "The ATLAS Experiment at the CERN Large Hadron Collider," *Journal of Instrumentation*, vol. 3, no. 8, 2008.

[3] G. Aad *et al.*, "Combined Measurement of the Higgs Boson Mass in *pp* Collisions at $\sqrt{s} = 7$ and 8 TeV with the ATLAS and CMS Experiments," *Physical Review Letters*, vol. 114, no. 19, p. 191803, 2015.

[4] CERN, "Accélérateurs du CERN." http://project-integration-accelerateurs.web.cern.ch (figure).

[5] O. S. Brüning, P. Collier, P. Lebrun, S. Myers, R. Ostojic, J. Poole, and P. Proudlock, *LHC Design Report*. Geneva: CERN, 2004.

[6] R. A. Fernandez, "The Large Hadron Collider." Presentation at JUAS 2015, https://indico.cern.ch/event/356897/.

[7] G. Iadarola, *Electron Cloud studies for CERN particle accelerators and simulation code development*. PhD thesis, University of Naples Federico II, 2014.

[8] G. Apollinari, I. Béjar Alonso, O. Brüning, M. Lamont, and L. Rossi, *High-Luminosity Large Hadron Collider (HL-LHC): Preliminary Design Report*. CERN Yellow Reports: Monographs, Geneva: CERN, 2015.

[9] F. Bordry, "Chamonix 2016 conclusions." Presentation at Chamonix workshop 2016, https://indico.cern.ch/event/486336/.

[10] B. Henrist, N. Hilleret, M. Jiménez, C. Scheuerlein, M. Taborelli and G. Vorlaufer, "Secondary electron emission data for the simulation of electron cloud," in *Proc. of ECLOUD'02, Geneva, Switzerland, April 2002*, p. 84, 2002.

[11] V. Baglin, I. Collins, B. Henrist, N. Hilleret and G. Vorlaufer, "A Summary of main experimental results concerning the secondary electron emission of copper," *CERN LHC Project Report*, vol. 472, 2002.

[12] R. Cimino, I. R. Collins, M. A. Furman, M. Pivi, F. Ruggiero, G. Rumolo, and F. Zimmermann, "Can low-energy electrons affect high-energy physics accelerators?," *Physical Review Letters*, vol. 93, p. 014801, 2004.

[13] R. Cimino and I. Collins, "Vacuum chamber surface electronic properties influencing electron cloud phenomena," *CERN LHC Project Report*, vol. 669, 2003.

[14] M. T. A. Kuzucan, H. Neupert and H. Störi, "Secondary Electron Yield on Cryogenic Surfaces as a Function of Physisorbed Gases," in *Proc. of the IPAC11 International Particle Accelerator Conference, San Sebastian, Spain*, 2011.

[15] R. Cimino, L. A. Gonzalez, R. Larciprete, A. Di Gaspare, G. Iadarola, and G. Rumolo, "Detailed investigation of the low energy secondary electron yield of technical cu and its relevance for the lhc," *Phys. Rev. ST Accel. Beams*, vol. 18, May 2015.

[16] F. Zimmermann, "Electron-Cloud Effects in past and future machines - walk through 50 years of Electron-Cloud studies," in *Proc. of ECLOUD12, La Biodola, Isola d'Elba, Italy*, 2012.

[17] R. E. Kirby and F. King, "Secondary electron emission yields from PEP-II accelerator materials," *Nuclear Instruments and Methods in Physics Research Section A: Accelerators, Spectrometers, Detectors and Associated Equipment*, vol. 469, no. 1, p. 1, 2001.

[18] E. Bronchalo, A. Coves, I. Montero, L. Olano, R. Mata, B. Gimeno, and V. E. Boria, "Influence of the angle of incidence of primary electrons on the total secondary electron yield," in *Proc of International Workshop on Multipactor, Corona and Passive Intermodulation MULCOPIM 2017, Noordwijk, Netherlands*, 2017. (unpublished).

[19] J. M. Jimenez *et al.*, "Electron cloud with LHC-type beams in the SPS: A review of three years of measurements," in *Proc. of ECLOUD'02, Geneva, Switzerland, April 2002*, CERN, 2002.

[20] G. Rumolo and F. Zimmermann, "Electron-Cloud Simulations: Build Up and Related Effects," in *Proc. of ECLOUD'02, Geneva, Switzerland, April 2002*, p. 105, 2002.

[21] E. Bronchalo *et al.*, "Secondary Electron Emission of Pt: Experimental Study and Comparison With Models in the Multipactor Energy Range," *IEEE Transactions on Electronic Devices*, vol. 63, no. 8, p. 3270, 2016.

[22] J. Jonker, “The angular distribution of the secondary electrons of soot,” *Philips Research Reports*, vol. 8, no. 6, p. 434, 1953.

[23] H. Kanter, “Zur Rückstreuung von Elektronen im Energiebereich von 10 bis 100 keV,” *Annalen der Physik*, vol. 455, no. 1-6, p. 144, 1957. (In German language).

[24] H. Kanter, “Contribution of backscattered electrons to secondary electron formation,” *Physical Review*, vol. 121, no. 3, p. 681, 1961.

[25] T. Koshikawa and R. Shimizu, “A monte carlo calculation of low-energy secondary electron emission from metals,” *Journal of Physics D: Applied Physics*, vol. 7, no. 9, p. 1303, 1974.

[26] M. Furman and M. Pivi, “Probabilistic model for the simulation of secondary electron emission,” *Physical Review Special Topics-Accelerators and Beams*, vol. 5, no. 12, p. 124404, 2002.

[27] K. Kanaya and H. Kawakatsu, “Secondary electron emission due to primary and backscattered electrons,” *Journal of Physics D: Applied Physics*, vol. 5, no. 9, p. 1727, 1972.

[28] J. P. Boris, “Relativistic plasma simulation-optimization of a hybrid code,” in *Proc. of the 4th Conference on the Numerical Simulation of Plasmas, Naval Research Lab, Washington DC*, p. 3, 1970.

[29] H. Qin, S. Zhang, J. Xiao, J. Liu, Y. Sun, and W. M. Tang, “Why is boris algorithm so good?,” *Physics of Plasmas*, vol. 20, no. 8, p. 084503, 2013.

[30] G. Iadarola *et al.*, “PyECLOUD Reference Manual.” `https://github.com/PyCOMPLETE/PyECLOUD/wiki`, 2017.

[31] J. Greenwood, “The correct and incorrect generation of a cosine distribution of scattered particles for monte-carlo modelling of vacuum systems,” *Vacuum*, vol. 67, no. 2, p. 217, 2002.

[32] S. W. V. Sciver, *Helium Cryogenics*. New York: Springer, 2 ed., 2012.

[33] E. Hatchadourian, P. Lebrun, and L. Tavian, “Supercritical Helium Cooling of the LHC Beam Screens,” *CERN LHC Project Report*, vol. 212, 1998.

[34] A. Romano, G. Iadarola, K. Li, and G. Rumolo, “Effect of the lhc beam screen baffle on the electron cloud buildup,” in *Proc. of International Particle Accelerator Conference (IPAC’16), Busan, Korea, May 8-13, 2016*, p. 1454, 2016.

[35] V. Anashin *et al.*, “Magnetic and electric field effects on the photoelectron emission from prototype LHC beam screen material,” *Vacuum*, vol. 60, no. 1, p. 255, 2001.

[36] Y. Suetsugu, Y. Tanimoto, Y. Hori, K. Kanazawa, M. Kobayashi, and Y.-J. Hsu, “Reduction of the photoelectron yield from a copper beam chamber by saw-tooth machining,” in *Proc. of Particle Accelerator Conference (PAC) 2001, Chicago, USA*, vol. 3, p. 2177, 2001.

[37] G. Iadarola and P. Dijkstal, “LHC heat loads: Observations with different bunch spacings.” presented at Electron Cloud Meeting 24.02.2017 `https://indico.cern.ch/event/615085`.

[38] G. Iadarola, “Analysis of the heat load differences between sectors.” presented at Electron Cloud Meeting 25.08.2017 `https://indico.cern.ch/event/660465/`.

[39] G. Iadarola and P. Dijkstal, “Heat load calculators for the Large Hadron Collider,” 2016. `https://github.com/giadarol/HeatLoadCalculators` (code).

[40] Elias Métral, “Beam Screen Issues,” 2010. Presentation at EuCARD - AccNet mini workshop on a "High Energy LHC", 15. Oct. 2010.

[41] K. Wille, *Physik der Teilchenbeschleuniger und Synchrotronstrahlungsquellen*. Stuttgart: Teubner, 2 ed., 1996. In German language.

[42] A. Seryi *et al.*, “Overview of design development of fcc-hh experimental interaction regions,” in *Proc. of International Particle Accelerator Conference (IPAC’17), Copenhagen, Denmark*, p. 2151, 2017.

[43] K. Oide *et al.*, “Design of beam optics for the future circular collider e+ e- collider rings,” *Physical Review Accelerators and Beams*, vol. 19, no. 11, p. 111005, 2016.

[44] H. Grote and F. Schmidt, “Mad-x-an upgrade from mad8,” in *Proc. of Particle Accelerator Conference (PAC) 2003, Portland, USA*, vol. 5, p. 3497, 2003.

[45] J. Rossbach and P. Schmüser, “Basic course on accelerator optics,” 1993. Lecture notes. `https://cds.cern.ch/record/247501`.

[46] H. Wiedemann, *Particle Accelerator Physics*. Springer, 2015.

[47] P. Dijkstal, “Electron cloud buildup simulations for the LHC (master proposal presentation).” presented at Electron Cloud Meeting 31.03.2017, `https://indico.cern.ch/event/605497/`.

[48] V. Baglin, I. R. Collins, and O. Gröbner, “Photoelectron yield and photon reflectivity from candidate LHC vacuum chamber materials with implications to the vacuum chamber design,” in *Proc. of EPAC’98, Stockholm, Sweden*, 1998.

[49] V. Baglin, I. R. Collins, O. Gröbner, C. Grünhagel, B. Henrist, N. Hilleret, and B. Jenninger, “Measurements At EPA Of Vacuum And Electron-Cloud Related Effects,” in *Proc. of 11th Chamonix - LHC Workshop, Chamonix, Switzerland*, 2001.

[50] N. Mahne, V. Baglin, I. Collins, A. Giglia, L. Pasquali, M. Pedio, S. Nannarone, and R. Cimino, “Photon reflectivity distributions from the LHC beam screen and their implications on the arc beam vacuum system,” *Applied Surface Science*, vol. 235, no. 1–2, p. 221, 2004.

[51] R. Cimino, V. Baglin, and I. Collins, “VUV synchrotron radiation studies of candidate LHC vacuum chamber materials,” *Vacuum*, vol. 53, no. 1, p. 273, 1999.

[52] A. Hofmann, *The Physics of Synchrotron Radiation*. Cambridge: University Press, 2004.

[53] L. A. Gonzales, M. Angelucci, R. Larciprete, and R. Cimino, “SEY and LE-SEY studies on different materials of relevant interest for Multipacting and e-Cloud mitigation,” in *Proc of International Workshop on Multipactor, Corona and Passive Intermodulation MULCOPIM 2017, Noordwijk, Netherlands*, 2017. (unpublished).

[54] A. Kahn, “Fermi level, work function and vacuum level,” *Materials Horizons*, vol. 3, p. 7, 2016.

[55] J.-P. Delahaye and A. Krusche, “The lattice design of the lep electron positron accumulator (epa),” *IEEE Transactions on Nuclear Science*, vol. 30, no. 4, p. 2050, 1983.

[56] P. Dijkstal, “Python Repository for PyECLOUD Input Parameters,” 2017. `https://github.com/pdijksta/CellStudyInputPyECLOUD` (code).

[57] G. G. Cantón, D. Sagan, and F. Zimmermann, “Simulating Proton Synchrotron Radiation in the Arcs of the LHC, HL-LHC and FCC-hh,” in *Proc. of International Particle Accelerator Conference (IPAC’16), Busan, Korea*, 2016.

[58] G. Dugan and D. Sagan, “Synrad3D Photon propagation and scattering simulation,” in *Proc. of ECLOUD 2010: 49th ICFA Advanced Beam Dynamics Workshop on Electron Cloud Physics, Ithaca, NY*, p. 118, 2010.

[59] L. Mether and G. G. Cantón. Private communication, August 2017.

[60] R. Kersevan, “SYNRAD, a Monte Carlo synchrotron radiation ray-tracing program,” in *Proc. of Particle Accelerator Conference (PAC) 1993, Washington, D.C., USA*, p. 3848, 1993.

[61] M. Ady, *Monte Carlo simulations of ultra high vacuum and synchrotron radiation for particle accelerators*. PhD thesis, EPFL Lausanne, 2016.

[62] G. Iadarola. Private communication, September 2017.

Electron cloud buildup simulations for the LHC

Project-Proposal von Philipp Dijkstal
Tag der Einreichung:

1. Gutachten: Prof. Dr. rer. nat. Oliver Boine-Frankenheim
2. Gutachten: Dr. rer. nat. Giovanni Iadarola

TECHNISCHE UNIVERSITÄT DARMSTADT

Fachbereich Physik
Theorie Elektro-
magnetischer Felder (TEMF)

Electron cloud buildup simulations for the LHC

Vorgelegtes Project-Proposal von Philipp Dijkstal

1. Gutachten: Prof. Dr. rer. nat. Oliver Boine-Frankenheim
2. Gutachten: Dr. rer. nat. Giovanni Iadarola

Tag der Einreichung:

Abstract

Electron clouds are a phenomenon that arises in accelerators operating with positively charged particles. They are the result of an interaction between the beam and the confining chamber. Primary electrons, that can by generated by various processes, are accelerated by the beam and impinge on the chamber walls, which in turn emits secondary electrons (secondary electron emission). This process can trigger an avalanche multiplication of the electrons and the formation of an electron cloud. The impacting electrons deposit energy on the chamber's wall which can become a significant heat load especially in cryogenic environments, as it is the case for a major part of the Large Hadron Collider (LHC) at CERN. The consequences of this effect are very important for the LHC and future accelerators including the LHC luminosity upgrade (HL-LHC). The main goal of this work is to improve the understanding of the electron cloud induced heat loads, from the side of simulations and measurements. This report describes the steps that have been made so far and their implications.
The heat load data analysis has been improved by recalculating and storing the heat loads measured in different cryogenic sectors of the LHC for all proton fills in 2015 and 2016. An excerpt of this data has been created, which includes also various kinds of beam parameters. Its analysis proved to be very useful in identifying features and patterns of the electron cloud induced heat loads that went previously unnoticed, and that could be relevant for future studies.
Information has been collected also in dedicated tests performed at the LHC during Machine Development sessions. Three fills have been performed in 2016 with the purpose of exploring the intensity dependence of electron cloud effects in the regime of bunch intensities between 0.6 and $1.1 \cdot 10^{11}$ particles per bunch. Their analysis revealed a sensitivity of the heat load on the bunch intensity that should be reproducible by electron cloud buildup simulations. This is a necessary pre-condition to use these simulations in order to make predictions for intensity ranges that are relevant for the HL-LHC upgrade but that are unavailable for the current LHC accelerator.
In the future work leading up to the Master's thesis, emphasis will be laid on improving the electron cloud buildup simulations for the LHC, using the available measurements to identify possible weaknesses. In the course of this it will also be necessary to improve the model of the LHC cryogenic cell, including for example higher order magnets (sextupoles, octupoles) that have so far been neglected in electron cloud studies at CERN. The generation of photoelectrons through synchrotron radiation, that act as primary electrons for the buildup-process will also be examined in detail.

Contents

1 Introduction

This chapter introduces the Large Hadron Collider (LHC), the accelerator which is subject to the studies of this report. To help readers unfamiliar with the jargon used at CERN, basic aspects of beam operations are introduced. Later on, the need for further electron cloud studies at the LHC is motivated with necessary predictions on electron cloud effects for future machines and available data from the previous two years of beam operations at the LHC.

1.1 Large Hadron Collider

The Large Hadron Collider is the world's largest particle accelerator and capable of accelerating protons and lead ions. These beams are collided in four main experiments to investigate fundamental laws of physics. The detectors at the interaction points are ATLAS and CMS, that have most notably found the Higgs Boson in 2012 [1], ALICE which specialises on heavy ion collisions and LHCb, designed to study particles that contain bottom quarks. The LHC is supplied with protons by the injector complex made by Linac 2, the PS Booster, the Proton Synchrotron (PS) and the Super Proton-Synchrotron (SPS) (see Fig. 1.1). If ions are accelerated instead, an alternative route is being taken where Linac 2 and the Booster are replaced by Linac 3 and the Low Energy Ion Ring (LEIR). This report is however focused on proton operations.

The long-term operational schedule of the LHC is divided into runs and long shutdowns (LS), each of which lasts between two and four consecutive years [2]. The beam operations take place during the runs, while the LS are reserved for maintenance and upgrades in the LHC and its injector complex. Figure 1.2 shows the time plan for the following years, and includes also the high luminosity upgrade of the LHC.

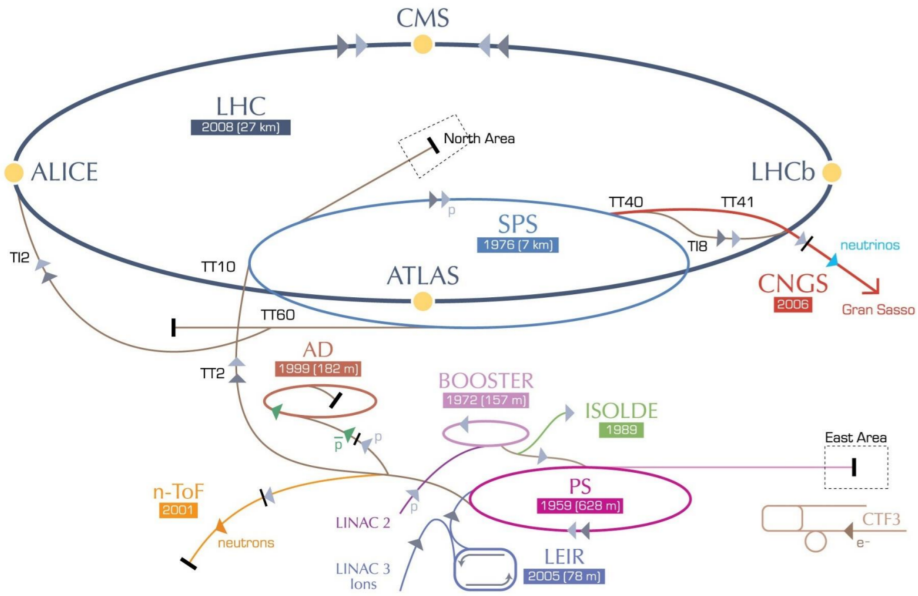

Figure 1.1: The accelerator complex at CERN including some signature experiments and detectors [3].

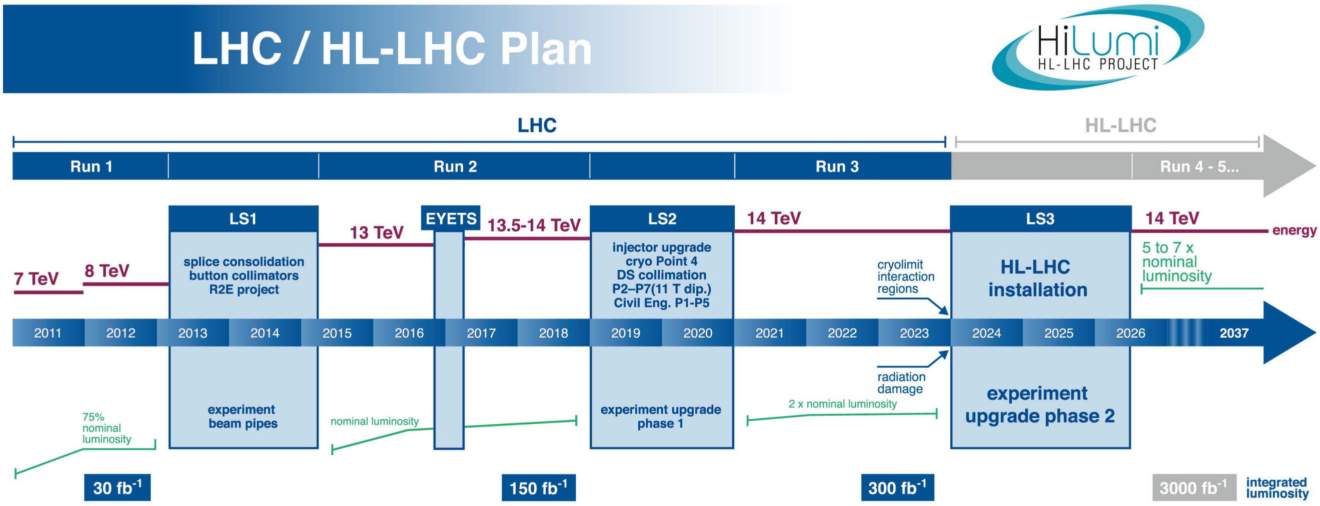

Figure 1.2: The schedule of the LHC operations since 2011, including the planned high luminosity upgrade. Some abbreviations used in this figure are Long Shutdown (LS) and Extended Year-End Technical Stop (EYETS). At the bottom, the expectations on the beam luminosity are noted in fb^{-1}. This is are a measure for the number of collisions in the detectors and therefore also the performance of the LHC from the point of view of the physics experiments. The collision energy in red is the sum of the energies of both beams [4].

1.2 A typical fill for proton physics at the LHC

This section explains the main phases of a typical fill for proton physics, where beams are put into collision for the LHC experiments. An overview is provided in Fig. 1.3, where the energy, the total intensities, the bunch length and the average heat load on the cryogenic cells for each arc are shown.

Such a fill begins right after the previous beam has left the accelerator, meaning that the superconducting magnets have to be ramped down first. Multiple injections from the SPS are necessary to refill the LHC because of its larger circumference. Shortly after the injection of the last train, the machine is ready to ramp the beam energy from injection (450 GeV) to flat top energy (6.5 TeV). The beam size at the interaction regions in the LHC is decreased (squeezed) to increase the collision rate (luminosity). The machine parameters are adjusted to optimize the performance, before the "stable beams" condition is declared and the experiments begin the collection of data. The intensity starts to decrease notably afterwards, mainly because the collided protons are lost. This is also called the luminosity burn-off. Furthermore the energy spread of the beam shrinks as the protons with higher energy emit more synchrotron radiation. Because bunch length and energy spread are linked through the synchrotron motion, the former also decreases in the process (see Fig. 1.3). The machine is meant to operate for several hours in this way, until the intensity becomes too low and a planned dump takes place. Often enough however, the beam has to be dumped early for machine safety reasons. Because of this, there is a wide spread in the duration of proton physics fills, ranging from only several hours to 40 hours.

A quick overview of the basic beam properties relevant for electron clouds is provided here. Most fills for proton physics in 2016 contained between 2040 and 2220 bunches, with up to $1.3{\cdot}10^{11}$ protons per bunch (see also Fig. 4.1). A bunch spacing of 25 ns has been the main operational mode since 2015. The filling pattern is formed by the LHC injector complex, especially the PS and the SPS, and is occasionally changed to optimize the machine performance. It consists of batches of consecutively filled bunch slots separated by empty slots, see Fig. 1.4. The batches are separated by gaps of 225 ns, corresponding to the rise time of the SPS injection kicker. Several batches form a train, and consecutive trains are interrupted by 925 ns of empty slots due to the LHC injection kicker rise time. An abort gap of 3 μs has to be present at one point in the filling pattern, to enable an extraction at high energy towards the beam dump [5].

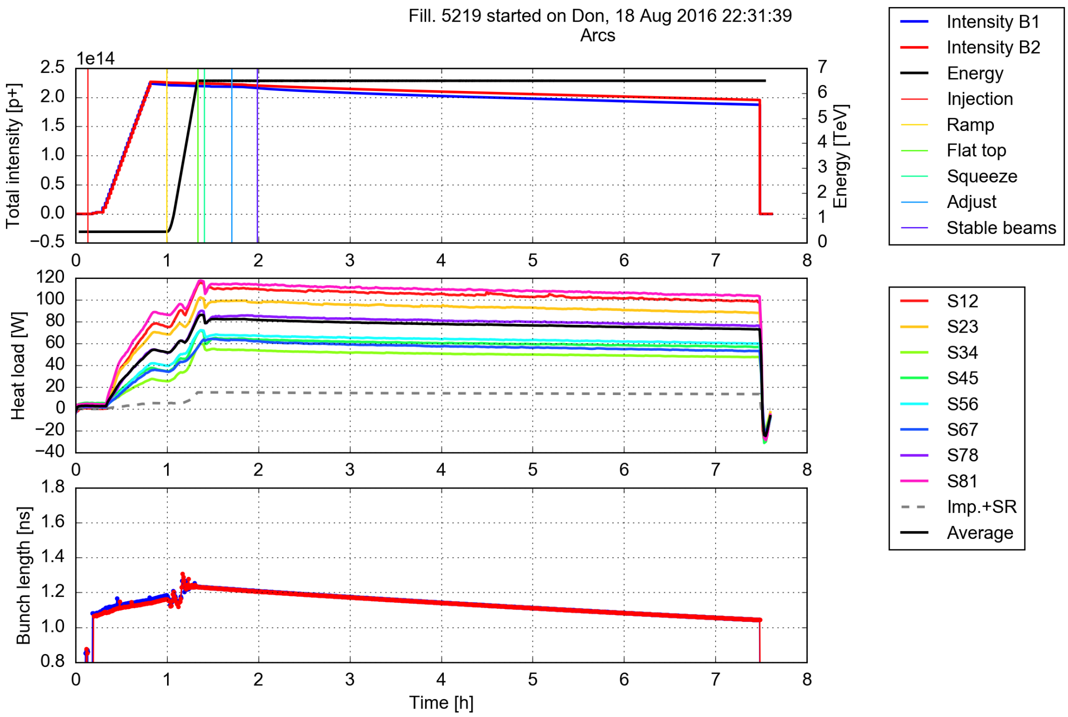

Figure 1.3: In the upper plot, the energy and the total beam intensities are shown during a typical fill in the LHC. It is also indicated when the status of the fill changes. The middle plot features the average heat loads on the cells of the cryogenic system in the eight arcs of the LHC. The sources of heat load besides the electron cloud are impedance and synchrotron radiation. At the bottom, the average bunch length is shown.

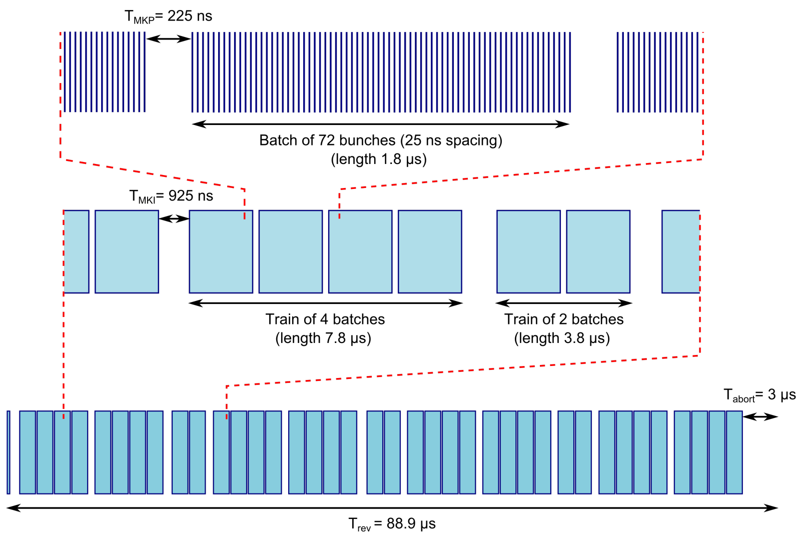

Figure 1.4: The LHC filling pattern consists of several trains, these in turn consist of several batches of consecutively filled bunch slots. The filling pattern has a great influence on the electron cloud effects [5].

The number of electrons in a beam pipe can grow large enough to become significant mainly because of secondary electron emission. It means that, depending on properties of the surface, one impinging electron can cause multiple other electrons to emerge into the chamber as well. It requires the presence of primary electrons, which can for example be created by the photoelectric effect or residual gas ionization. This can lead to a substantial increase of electrons in the chamber, called electron cloud (EC). This process eventually reaches an equilibrium state when the space charge effect of the already present electrons prevents a further increase. The cloud of electrons interacts with the beam through electro-magnetic forces and can distort the beam quality. Another problem is that in environments such as the LHC with its large number of magnets at cryogenic temperatures, the heat that the many electrons cause while impinging on walls has to be absorbed by the cooling system at very low temperatures. If these heat loads were to reach the limits of the cooling system, the beam parameters would have to be modified to allow for a continuation of beam operations. Already for the current LHC, the cryoplants for some of the arcs operate at around 75% of their maximum cooling capacity. This is shown in Fig. 1.3 where heat loads of up to 120 W per cryogenic cell are measured as the average for some arcs, while the performance limit of the cooling circuits is known to be 160 W per cryogenic cell.

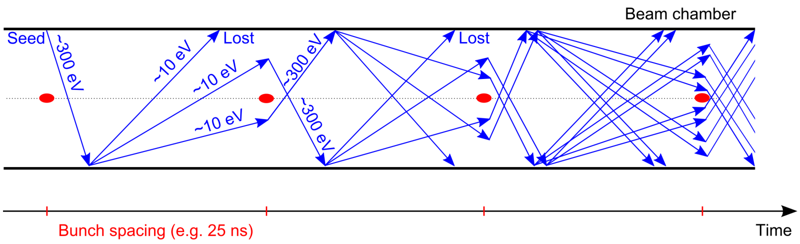

Figure 1.5: This sketch visualizes how electrons can trigger an avalanche effect as they are accelerated by the positively charged beam and then hit the wall, causing more electrons to enter the chamber. In the end, the population is dense enough to be called a cloud of electrons [5].

Electron cloud effects have been studied at CERN for many years. The CERN electron cloud team performs simulations and experimental work to improve the operation of the LHC and future machines. These include most importantly the planned HL-LHC and the proposed Future Circular Collider (FCC). For each of these accelerators, EC effects have been recognized as among the major performance limitations [4, 6]. A good understanding of these effects is therefore crucial for the future of high energy hadron accelerators. The upgrade to HL-LHC will require higher bunch intensities of planned $2.2 \cdot 10^{11}$ protons per bunch [4], while the current LHC has only operated with up to $1.3 \cdot 10^{11}$ in run 2. The cooling system will not be upgraded.

In contrast to previous studies that include buildup simulations for LHC [5], the data that has been accumulated during run 2 is now available. Especially the measured heat loads on the cryogenic system can provide insight, as they are primarily caused by electron clouds. This is even more significant because EC effects are much stronger at a bunch spacing of 25 ns, the default configuration of run 2 that is also going to be used for the HL-LHC. During the preceding run 1, 50 ns were used for the most part instead.

This leaves several frontiers for this work. On one side, the LHC cryogenic cells, where the heat loads are measured, have to be simulated using the best knowledge available. On the other side, the measured heat loads themselves need to be closely examined to ensure that they are correctly interpreted. Furthermore, the large set of especially heat load data should be analyzed to find previously unknown features and scaling laws of electron cloud effects.

This chapter starts with a brief description of the secondary emission model used for the simulation software PyECLOUD. This tool has been used at CERN for several years, and its fundamental aspects are recapped. Examples of buildup simulations for quadrupoles and dipoles are shown. Afterwards, several parameters from the previously mentioned SEY model have been varied to show the impact on the heat loads yielded by the simulations.

2.1 Secondary emission of electrons

The process of secondary electron emission (SEY) is subject of ongoing research at CERN and other labs. The CERN electron cloud team uses a model based on experimental data for copper [5, 7, 8, 9, 10, 11]. The secondary emission parameter $\delta(E)$ is defined as the ratio between the electron current onto the wall and the emitted current. It is dependent on the energy of the impinging electrons and their angle of incidence θ.

$$\delta(E,\theta) = \frac{I_{\mathrm{Emit}}}{I_{\mathrm{imp}}(E,\theta)} \tag{2.1}$$

The emitted current, and therefore also $\delta(E)$, can be divided into parts formed by true secondary electrons and elastically scattered electrons. The latter are modelled in the following way, not depending on θ:

$$\delta_{\mathrm{elas}}(E) = R_0 \left(\frac{\sqrt{E} - \sqrt{E+E_0}}{\sqrt{E} + \sqrt{E+E_0}} \right)^2 \tag{2.2}$$

For the two parameters R_0 and E_0, 0.7 and 150 eV are used by default for the LHC beam chamber. However there are conflicting opinions on the shape of the for the very low energy part of this relation, where some say $\delta_{\mathrm{elas}}(E=0)$ should approach 0 or 1. The value 0.7 for R_0 is a compromise following this disagreement [12, 13].

The true secondary emission yield depends on the shape parameter s and on E_{max}, the incident energy resulting to the most secondary electrons.

$$\delta_{\mathrm{true}}(E,\theta) = \delta'_{\mathrm{max}}(\theta) \frac{s \frac{E}{E'_{\mathrm{max}}(\theta)}}{s - 1 + \left(\frac{E}{E'_{\mathrm{max}}(\theta)} \right)^s} \tag{2.3}$$

$$\delta'_{\mathrm{max}}(\theta) = \delta_{\mathrm{max}}\, e^{\frac{1-\cos\theta}{2}} \tag{2.4}$$

$$E'_{\mathrm{max}}(\theta) = E_{\mathrm{max}}\,(0.3 + 0.7\cos\theta) \tag{2.5}$$

The angular dependence is motivated by the increased time that electrons spend close to the surface in case they have a larger angle of incidence. Therefore their chance to produce secondaries is enhanced. Plots that show δ_{true} and δ_{elas} are found in Fig. 2.1. It becomes clear that the elastic scattering only happens for low incident energies, and that high angles of incidence significantly increase the emission of true secondaries. Because δ_{max} is expected to change in the process of electron cloud mitigated scrubbing (see Sec. 4.2), it is scanned in almost all simulation studies and often called "the SEY parameter". E_{max} and s on the other hand have been fixed at 1.35 and 330 eV for most simulations.

The energy of the emitted secondaries follows a log-normal distribution specified by μ and σ, normally determined as 1.0828 and 1.6636 (see [5] and references therein).

$$\frac{\mathrm{d}n_{\mathrm{true}}}{\mathrm{d}E} = \frac{1}{E\sigma\sqrt{2\pi}} e^{-\frac{(ln(E)-\mu)^2}{2\sigma^2}} \tag{2.6}$$

The angle of emitted secondaries follows a cosine distribution.

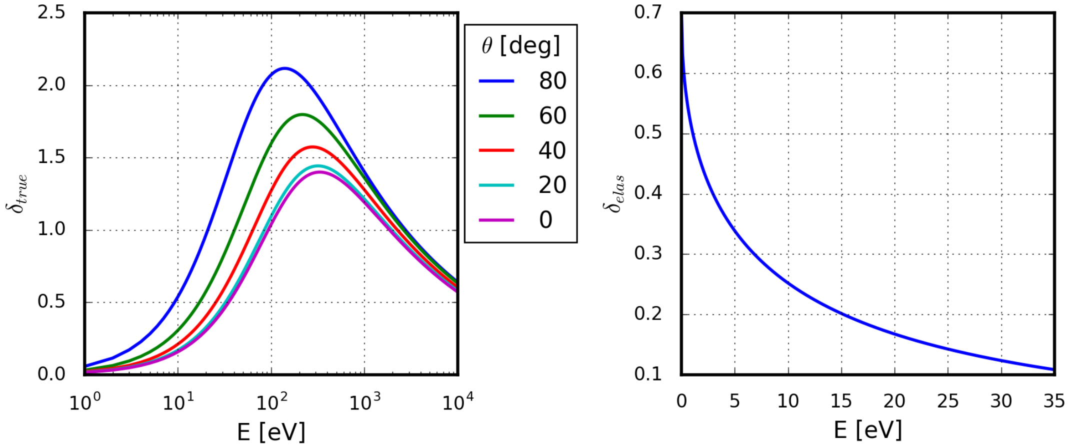

Figure 2.1: These curves correspond to Eq. (2.3) and (2.2), and show the ratios of true secondary and elastically scattered electron currents with respect to the impinging current.

2.2 PyECLOUD buildup simulations

PyECLOUD is a 2D code that simulates the EC buildup in a thin slice around a certain section of a particle accelerator. Electrons are grouped in macro-particles (MP), in order to achieve a reasonable computational burden. The program is thoroughly described in [5], a summary of the principal features is provided here. Figure 2.3 shows a flowchart of the main loop in the simulation.

1. It begins with the seeding process, where gasionization and photoemission by synchrotron radiation are implemented. Alternatively, an initial distribution of primary electrons can be specified, without considering a seeding mechanism. This is a valid approximation in case there is multipacting and the seeding process would soon become irrelevant anyways compared to the large number of secondaries.

2. The beam is approximated to be rigid, meaning it remains unaffected by the EC for the duration of the simulation. The electromagnetic fields of the beam have therefore to be calculated only once in the initialization stage. The beam charge distribution takes the following form

$$\rho(x,y,s,t) = \lambda(s-ct)\rho_{\perp}(x,y), \tag{2.7}$$

   where the transverse beam profile $\rho_{\perp}$ is assumed to be Gaussian. The longitudinal profile λ is either specified or also generated with a Gaussian form.

3. A Particle in Cell (PIC) algorithm is used to obtain the space charge forces of the electron cloud. This means that the macro-particles are projected on a grid, and the electrostatic potential is calculated with the Finite Differences method. The electric field is the first derivative of the electrostatic potential.

4. The MPs are tracked in the chamber while they are exposed to the electromagnetic forces from the confining magnet, the beam and the electrons themselves. The Lorentz force determines the movement of the particles.

$$\mathbf{F} = -q\left(\mathbf{E} + \mathbf{v} \times \mathbf{B}\right) \tag{2.8}$$

5. When macro-particles impact on the chamber walls, it is decided how many of them are treated as elastically reflected or as a secondary electrons. In case of the latter, the size of the MP may grow. A dedicated procedure to split up MPs that are too large, and to remove MPs that are very small is implemented. The number of macro-particles is therefore dynamic.

For the beam chamber as installed at the LHC Arcs, one train of protons has been simulated in dipoles and quadrupoles, see Fig. 2.2. The magnetic fields and beam parameters are those that occur at 6.5 TeV during a typical fill. The 4 σ bunch length was set to 1.2 ns, and the bunch intensity to 1.1 $\cdot 10^{11}$ particles per bunch. The train consisted of 4 batches of 72 bunches each, separated by 8 empty slots. The parameter $\delta_{\max}$ has been scanned, while the others are set as described in the previous section. A uniform initial distribution of 10^7 electrons per m has been in the chamber.

It is possible to use a measured beam profile as an input, where the bunch lengths and bunch intensities from the FBCT (Fast Beam Current Transformer) for all bunches are used to create a Gaussian shaped beam. Whenever an MP hits the chamber wall, the deposited energy is calculated and saved. The sum of these impacts yields the simulated heat load, which can in turn be compared with the measured heat loads from the same beam (see Fig. 2.4).

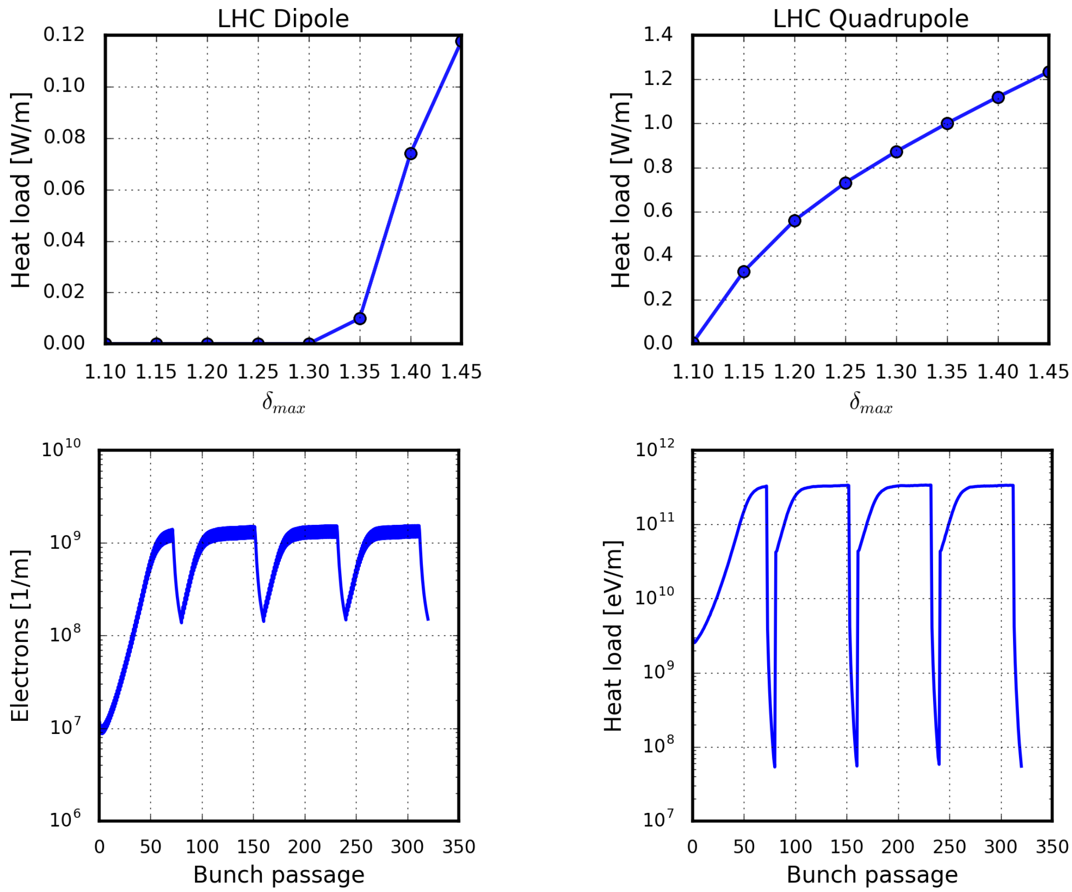

Figure 2.2: One train of protons (288 bunches) has been simulated under variation of $\delta_{\max}$. The upper plots show the resulting heat loads for dipoles and quadrupoles. The bottom plot features the number of electrons and the heat loads per bunch passage. These are taken from the simulation for dipoles with $\delta_{\max} = 1.45$.

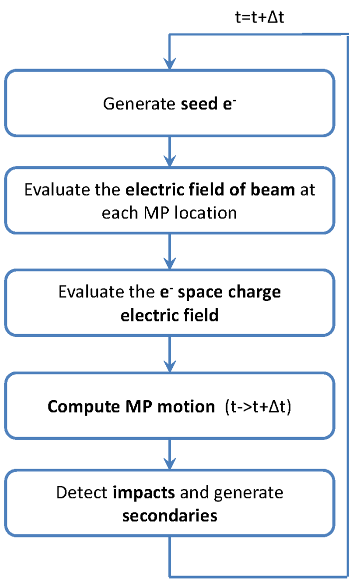

Figure 2.3: A flowchart of the PyECLOUD main loop [5].

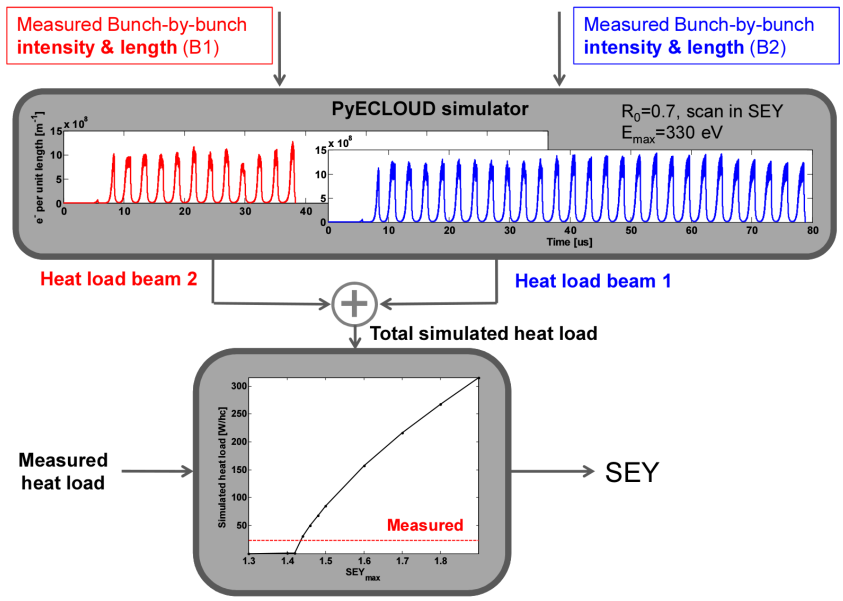

Figure 2.4: This sketch demonstrates how PyECLOUD can be utilized to infer the $\delta_{\max}$ (SEY) parameter in the LHC. This implies that the other parameters, for example R_0 and $E_{\max}$, are known [5].

Some of the input parameters for the SEY model have been varied in order to find out how sensitive the simulated heat loads are. All other parameters have been identical to the simulations shown in Fig. 2.2.

Figure 2.5 (top) shows the changes in heat loads when E_{max} from Eq. (2.3) is altered. It has opposite effects on dipoles and quadrupoles. This can be explained by trapped electrons in the quadrupoles, where the increasing fields in transverse direction can have the effect of an magnetic bottle. These electrons can be accelerated by multiple bunch passages and reach higher energies before impacting the wall. In case of the dipole, there are no possible trapping effects, and the occurring energies are lower.

Below in Fig. 2.5, the enhancement of the secondary emission with respect to the angle of incidence has been varied. The factor corresponds to A in the following equation, which replaces $\frac{1}{2}$ in Eq. (2.4):

$$\delta'_{\text{max}}(\theta) = \delta_{\text{max}}\, e^{A\cdot(1-\cos\theta)} \tag{2.9}$$

When the enhancement is fully removed (red curve), the EC effects for the quadrupole are diminished by a large factor. This means that most impinging electrons in this device do so with large angles of incidence, which is not the case for dipoles.

In Fig. 2.6, the energy distribution of secondary electrons has been changed (see Eq. (2.6)). First, only μ has been varied, which changes the SEY threshold for the dipoles, but not to a great extent for the quadrupoles. The second part changed both μ and σ by the specified factors, while the original curve is retained in red. This barely shifts the thresholds for both devices, but has a greater effect overall on the quadrupoles.

Parameters that have not been scanned so far include R_0 and E_0 for the elastically scattered SEY, and the angular dependence of the secondary electrons.

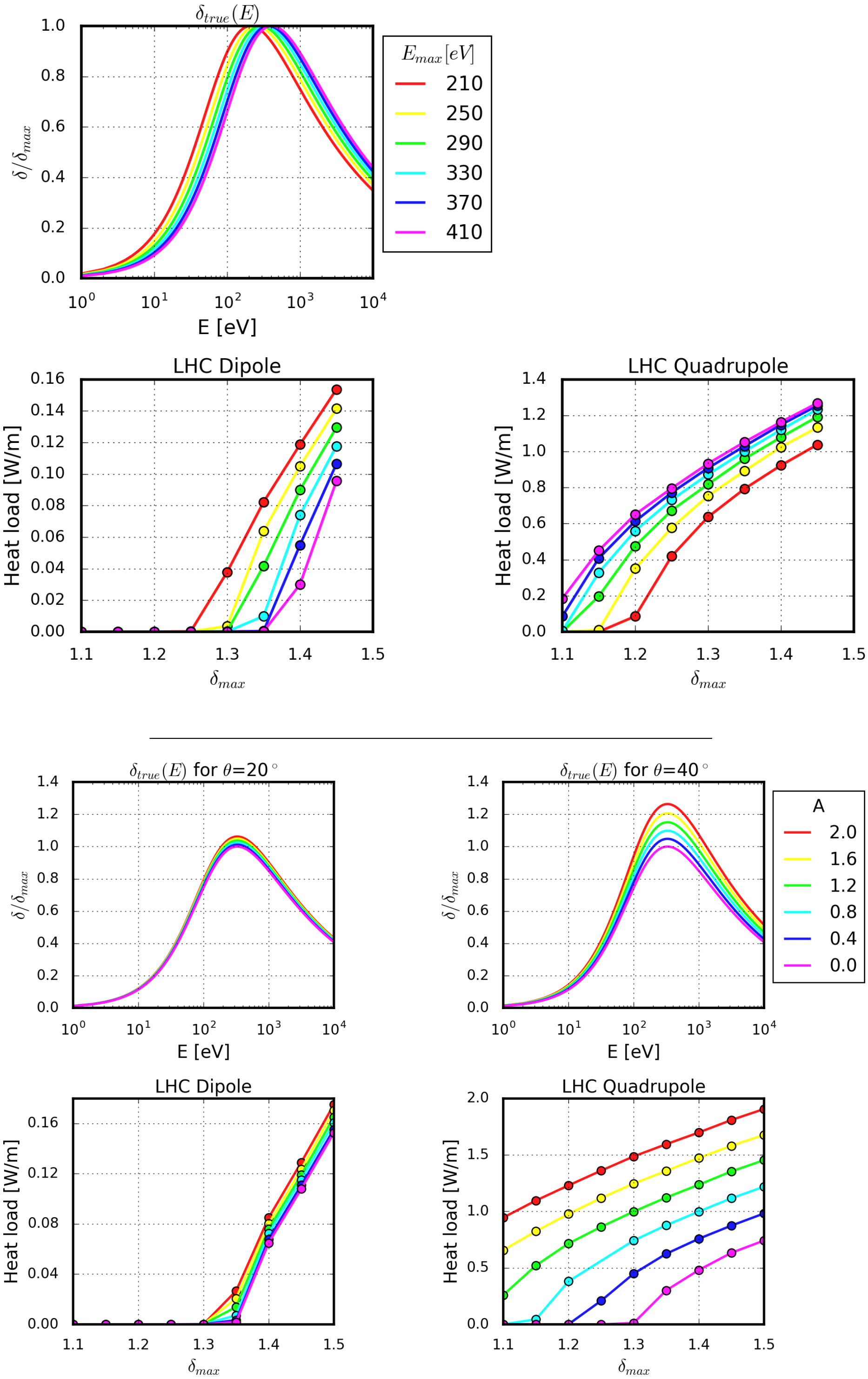

Figure 2.5: Top: the $E_{\max}$ parameter defines the secondary emission yield and has been varied for this set of simulations. With increasing $E_{\max}$, the EC in the dipoles decreases while it increases in the quadrupoles. Bottom: the factor A enhances or diminishes the increase of SEY with the angle electrons impinge on the walls, see Eq. (3.5). Normally is is defined as 0.5. The top two plots show the secondary emission yield for angles of 20° and 40°. This has a much larger effect on the quadrupoles.

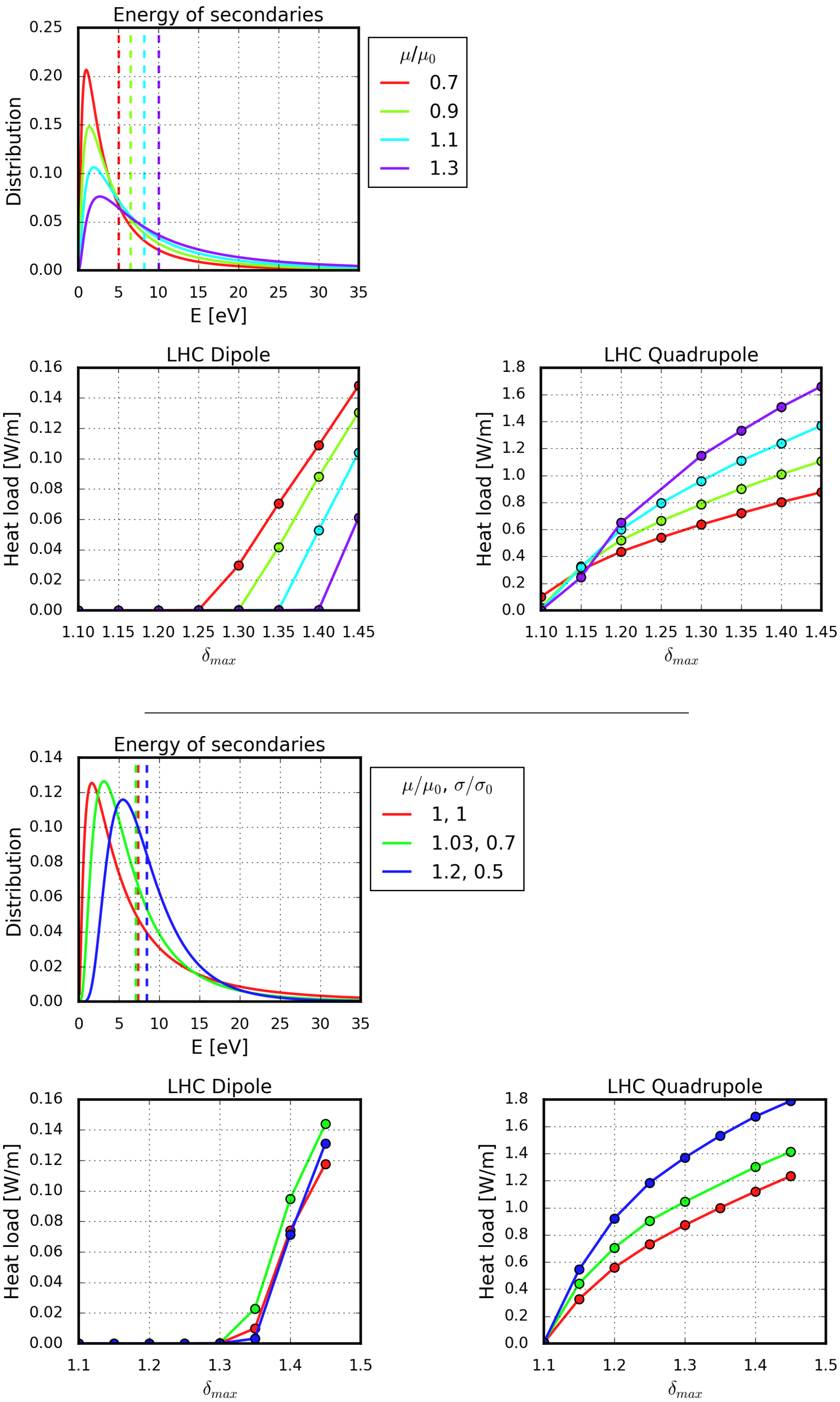

Figure 2.6: The energy distribution of secondary electrons has been modified. The upper part shows the effect of changing μ in the underlying log-normal distribution. For the lower part, both μ and σ have been changed.

An important part of this work is to closely examine the heat loads that are being caused by electron cloud. These are measured at the LHC and enhance our knowledge of EC effects. Furthermore they can be compared to simulation results.

This chapter describes the parts of the LHC cryogenic system that are relevant for this work, and how the beam screen cooling power is being measured. It is also necessary to estimate the components of the heat load that are not related to electron cloud and subtract them.

For the arc cells, only the combined heat load from multiple magnets and magnet types as well as their interconnections is being measured. It is therefore not easy to disentangle their contributions which are expected to by very different. Because of this, there are currently three specially instrumented cells with temperature sensors after each magnet. The detailed analysis of these cells, only partially attempted before, is part of this work.

For reasons that are outlined later in this chapter, it has been necessary to reimplement the heat load calculation as a more flexible module than what has been used prior to this work[1]. One section is devoted to a validation of the results, where also parts of work done by other people is shown to provide the reader with the necessary overview.

3.1 Cryogenics

Outside of the crossing regions of the LHC, the two particle beams are enclosed by separate vacuum chambers (beam tubes). The superconducting magnet coils are in thermal contact to these tubes and cooled by liquid helium at 1.9 K. The part of the vacuum vessel that has this lowest temperature is also called cold mass. Figure 3.1 shows a cross-section of an arc dipole. A beam screen (BS) is installed inside the beam tubes, with the purpose of absorbing the heat load caused by the beam, see Fig. 3.2. This beam screen is thermally isolated from the cold mass and kept at a higher temperature between 4.6 and 20 K. This allows for non-isothermal cooling that is around eight times more efficient with respect to isothermal cooling at 1.9 K [14]. The BS is cooled by a flow of weakly supercritical helium through two small attached tubes.

A cryogenic cell contains three dipoles and one quadrupole, as well as the necessary correction magnets and interconnections. Because two cryogenic cells correspond to a FODO cell in terms of beam optics, these are often called half-cells. An overview of the cryogenic transfer lines for the beam screens of a cryogenic cell in the arcs is shown in Fig. 3.3. The helium in the supply header denoted C origins from the cryoplants, it supplies the cells of an arc in parallel. The pressure and temperature is measured every four cells along the header. The helium enters a cell at the location subscripted 1 in the figure. During the following transfer line towards the magnets, a sink-in heat load Q_S has to be taken into account, as the tubes rest on support posts which leads to a small thermal coupling. An electrical heater is available to stabilize the temperature and the gas flow if there are rapid changes in the required cooling power, for example at the beginning and the end of fills. The flow is split up two times afterwards, first because there are two beam screens, and then again for the two cooling tubes of each BS. The temperatures T_2 and T_3 are measured in every cell before and after the beam screens, where the amount of heat denoted Q_{BS} is transferred to the helium. The mass flow is controlled by a valve (at position 4 in Fig. 3.3), after which the helium enters the return header D. Here, the pressure and temperature T_4 and P_4 are measured once again every four cells. While the heat is absorbed, the pressure changes only by a small amount whereas the temperature increases significantly (see Fig. 3.4). The pressures P_1 and P_4, the temperatures T_1, T_2, T_3 as well as the power of the electrical heater and the valve opening are stored in the logging data base at CERN and can be conveniently accessed. The details of the heat load computation, which relies on these quantities, are shown in the following pages.

3.2 Heat load calculation

Even though the necessity of a cell by cell measurement of the heat loads has not been foreseen during the design phase of the LHC, the cryogenics team of CERN has established such a procedure, which is described in this chapter [17][2].

1 The new module is available online under `https://github.com/pdijksta/GasFlowHLCalculator`

2 The author is indebted to Benjamin Bradu from BE-ICS-PCS, who answered a lot of questions regarding the cryogenic system and heat load calculations. Writing the new module, that is also based on his code, would have been impossible without his help.

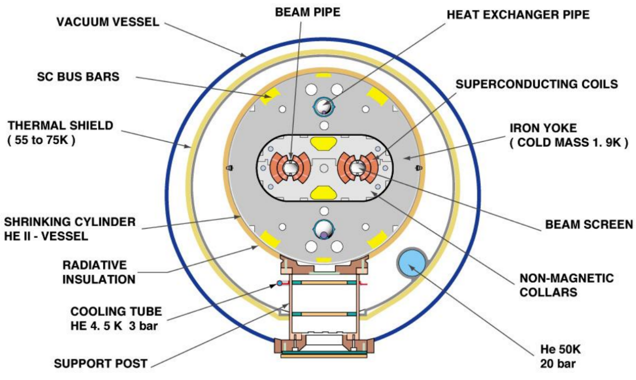

Figure 3.1: The cross section of the vacuum vessel of a dipole in the LHC [15]

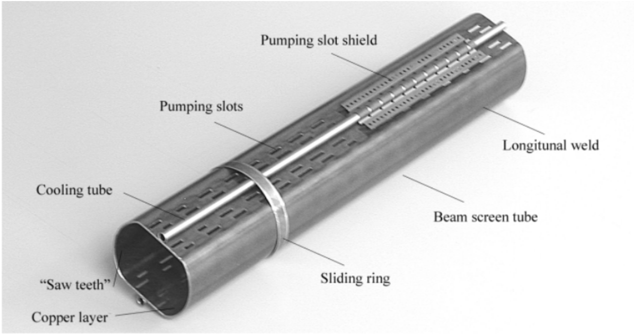

Figure 3.2: A photograph of a beam screen, which protects the cold mass at 1.9 K from beam-induced heat. Its design aperture is 44.04 mm and 34.28 mm in the horizontal and vertical planes. The purpose of the pumping slot shield is to intercept electrons [16].

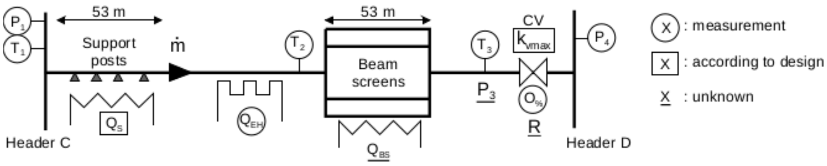

Figure 3.3: A sketch of the beam screen cooling for a typical cryogenic cell in the arcs. The different heat load contributions and the installed pressure and temperature sensors are shown [17].

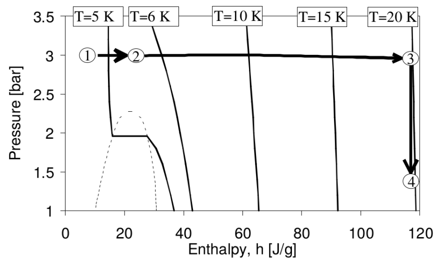

Figure 3.4: The state of the helium by design follows this line in the P-h diagram [14].

The beam induced heat load $\dot{Q}_{\mathrm{BS}}$ is obtained with an enthalpy balance. The indices of h follow Fig. 3.3 and the previously mentioned sensors.

$$\dot{Q}_{\mathrm{BS}} = \dot{m} \cdot (h_3 - h_1) - \dot{Q}_{\mathrm{EH}} - \dot{Q}_{\mathrm{S}} \tag{3.1}$$

Here, $\dot{m}$ is helium the mass flow, h the specific enthalpy and $\dot{Q}_{\mathrm{S}}$, $\dot{Q}_{\mathrm{EH}}$ are the sink-in heat load and the power of the electrical heater. The enthalpy is a function of pressure and temperature and can be obtained by interpolation of tables that have been calculated with dedicated software [18]. $\dot{Q}_S$ is part of the heat load calibration for every cell and assumed constant in time.

3.2.1 Mass flow

Because real flow meters have not been installed at the LHC, the mass flow $\dot{m}$ is instead computed through virtual flow meters. The procedure follows the Samson method [15], which is an engineering formula with empirical factors in suitable units. It requires knowledge of the thermodynamical state of the helium and the valve properties.

$$\dot{m} = 14.2 \cdot A(\frac{P_{\mathrm{out}}}{P_{\mathrm{in}}}) \cdot \sqrt{\rho_{\mathrm{in}} \cdot P_{\mathrm{in}}} \cdot K_{\mathrm{V}}(l) \tag{3.2}$$

$$K_{\mathrm{V}}(l) = K_{\mathrm{V,max}} \cdot R^{l-1} \tag{3.3}$$

$$\gamma = \frac{C_{\mathrm{p}}(P_{\mathrm{in}}, T_{\mathrm{in}}) + C_{\mathrm{p}}(P_{\mathrm{out}}, T_{\mathrm{out}})}{C_{\mathrm{v}}(P_{\mathrm{in}}, T_{\mathrm{in}}) + C_{\mathrm{v}}(P_{\mathrm{out}}, T_{\mathrm{out}})} \tag{3.4}$$

$$A(\frac{P_{\mathrm{out}}}{P_{\mathrm{in}}}) = \begin{cases} 1 \quad \text{if} \quad \frac{P_{\mathrm{out}}}{P_{\mathrm{in}}} < \left(\frac{2}{\gamma+1}\right)^{\frac{\gamma}{\gamma-1}} \\ 1.379 \cdot \sqrt{\frac{2\gamma}{\gamma-1} \cdot \left(\frac{P_{\mathrm{out}}}{P_{\mathrm{in}}}\right)^{\frac{2}{\gamma}} \cdot \left(1 - \left(\frac{P_{\mathrm{out}}}{P_{\mathrm{in}}}\right)^{\frac{\gamma-1}{\gamma}}\right)} \quad \text{otherwise} \end{cases} \tag{3.5}$$

$K_{\mathrm{V}}(l)$ is a property of the valve, where $K_{\mathrm{V,max}}$ defines the maximum mass flow for a fully open valve ($l = 1$). The rangeability R is the ratio between a fully opened and closed valve.

However for the LHC Beam Screen, this Samson method has been modified by the cryogenics team to obtain better results in a weakly supercritical regime [19]. The changes are highlighted in the following set of equations.

$$\dot{m} = \mathbf{1.25 \cdot 10^{-5}} \cdot A(\frac{P_{\text{out}}}{P_{\text{in}}}) \cdot \sqrt{\rho \cdot P_{\text{in}}} \cdot K_{\text{V}}(\mathbf{l})[\text{m}^3/\text{h}] \tag{3.6}$$

$$\mathbf{l} = l(u) = 1.1u - 0.1 \tag{3.7}$$

$$\boldsymbol{\gamma} = \frac{5}{3} \tag{3.8}$$

$$A(\frac{P_{\text{out}}}{P_{\text{in}}}) = \begin{cases} 1 & \text{if } \frac{P_{\text{out}}}{P_{\text{in}}} < \mathbf{0.42} \\ 1.379 \cdot \sqrt{\mathbf{5.03} \cdot \left(\frac{P_{\text{out}}}{P_{\text{in}}}\right)^{\frac{2}{\gamma}} \cdot \left(1 - \left(\frac{P_{\text{out}}}{P_{\text{in}}}\right)^{\frac{\gamma-1}{\gamma}}\right)} & \text{otherwise} \end{cases} \tag{3.9}$$

First of all a different constant is used in Eq. (3.6), $1.25 \cdot 10^{-5}$ instead of 14.2. Secondly, a pre-constraint is applied to the valve in anticipation of the negative thermal expansion during the cooling-down. This is reflected in the expression $l(u)$, where the measured and logged valve opening u is processed to obtain more accurate results. This conversion distorts the meaning of R, as l should normally range between 0 and 1 for minimum and maximum openings, whereas $l(u)$ as in Eq. 3.7 can become negative. In practice however, the electrical heater prevents very low values of u, which remains between 0.15 and 0.98 for a typical fill and translates to values of l that range between 0.06 and 0.98. The approximation of a constant γ is valid for ideal gasses. The critical point of Helium is 5.2 K, while the temperature at the valve is normally around 20 K, which is sufficiently far away. The effects of the changes of the numerical factors in $A(\frac{P_{\text{out}}}{P_{\text{in}}})$ are illustrated in Fig. 3.5.

$$\mathbf{0.42} = \left(\frac{2}{\gamma + 1}\right)^{\frac{\gamma}{\gamma-1}} - 0.067 \tag{3.10}$$

$$\mathbf{5.03} = \frac{2\gamma}{\gamma - 1} + 0.03 \tag{3.11}$$

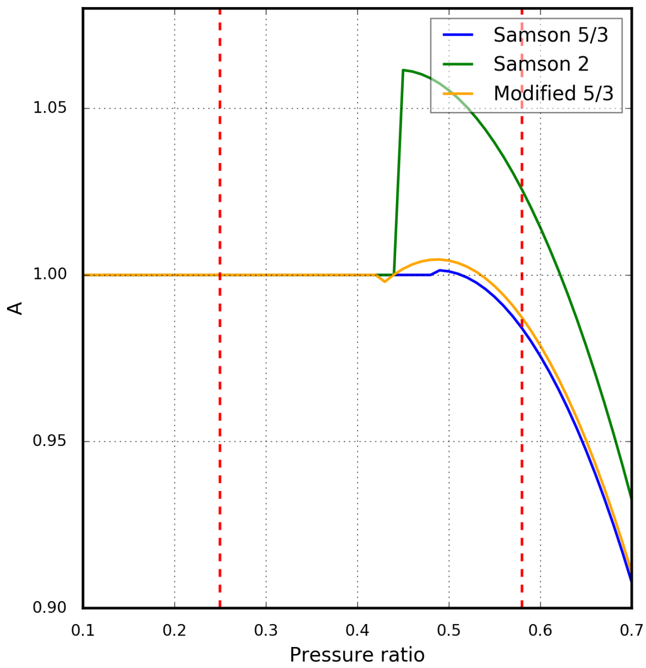

Figure 3.5: These curves illustrate the effect of modifications to the Samson A function. The original function as in Eq. (3.9) is shown for two values of γ, 2 and 5/3 together with the modified version that is implemented for the LHC cryogenics. In red are shown the limits between which the pressure ratios range for a typical fill.

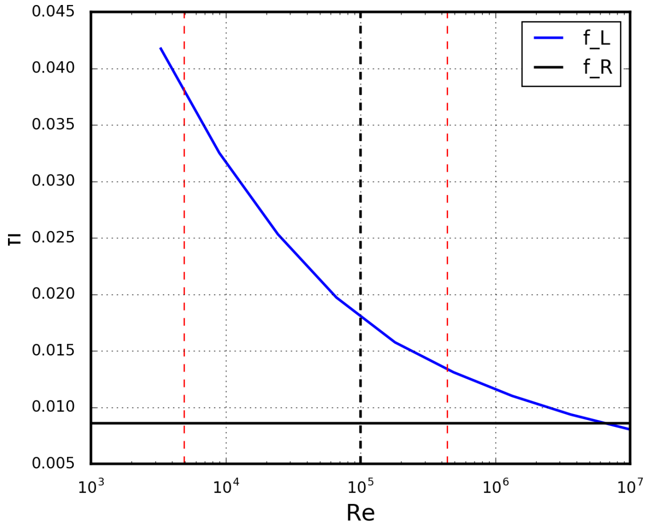

Figure 3.6: The term f_L from Eq. 3.16 is defined in three steps for different ranges of Reynolds number Re. The horizontal line is f_R from Eq. 3.14 for the radius and surface roughness of the Beam Screen cooling pipes is independent from Re. The red lines mark the upper and lower bounds of Re for a typical fill.

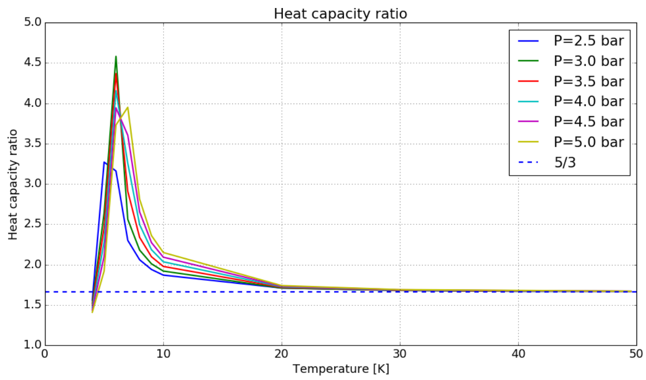

Figure 3.7: The heat capacity ratio γ as in Eq. (3.4) for different pressures and temperatures is obtained by interpolation over tables that have been calculated with HEPAK software [18].

For the valves in the cryogenic cells of the LHC, the pressure P_{in} in the formulas above corresponds to P_3 in Fig. 3.3 and is not measured. It can be approximated with P_1, as the pressure drop along the Beam Screen is expected to be small (Fig. 3.4). This allows to save a significant amount of computation time and is done for the online calculations for the logging database. For heat loads above ∼100 W, that estimation should however be avoided [17].

The pressure drop through a pipe is calculated with the Darcy-Weisbach equation (3.12), again modified by the CERN cryogenics team.

$$\Delta P = \frac{\max(f_{\text{R}}, f_{\text{L}}(\text{Re})) \cdot L \cdot \dot{m}_{\text{P}}^2}{2r \cdot \rho(P,T) \cdot (\pi r^2)^2} \tag{3.12}$$

$$\dot{m}_{\text{P}} = \frac{\dot{m}}{n_{\text{P}}} \tag{3.13}$$

$$f_{\text{R}} = \left(\frac{1}{2\ln(\frac{r}{R}) + 1.74} \right)^2 \tag{3.14}$$

$$\text{Re} = \frac{2r \cdot \dot{m}}{\pi r^2 \cdot \mu(P,T)} \tag{3.15}$$

$$f_{\text{L}}(\text{Re}) = \begin{cases} \frac{0.3164}{\text{Re}^{0.25}} & \text{for } 3 \cdot 10^3 \leq \text{Re} < 10^5 \\ \frac{0.221}{\text{Re}^{0.237}} + 0.0032 & \text{otherwise} \end{cases} \tag{3.16}$$

The pressure drop depends on the mass flow per pipe $\dot{m}_{\text{P}}$, the helium density ρ, the length of the pipe L, the pipe radius r and the friction factor f. Reynolds number Re, a measure for the flow turbulence which depends on the helium viscosity μ, decides upon the way this friction factor is determined. The two branches in Eq. (3.16) are Blasius correlations. A lower limit is defined by f_R, which is the Colebrook-White equation in the limit of an infinite Reynolds number [20, 21].

Figure 3.6 shows $f_L(\text{Re})$ and f_R for the surface roughness and inner radius of the Beam Screen cooling pipes. Re ranges between $4.9 \cdot 10^3$ and $4.4 \cdot 10^5$ for a typical fill.

Because $\dot{m}$ and ΔP depend on each other, an iterative approach is performed where ΔP starts at 0 ($P_3 = P_1$), and $\dot{m}$ is calculated with Eq. (3.2). P_3 is then found as $P_1 - \Delta P$ and serves as an input for the mass flow again. This is continued until P_3 does not change by more than 1% for an iteration.

3.2.3 Comparison of results

The calculation presented in the previous pages has been implemented in a python module for all the cooling loops installed in the LHC. The obtained results have been validated against the values obtained with the online calculation implemented by the cryogenics team, which are recorded in the LHC logging database. The latter has been computed neglecting the pressure drop, whereas the new module offers a choice but defaults to including this effect.

Figure 6.2 in the appendix shows in a histogram the relative change of the pressure from P_1 to P_3, as it is computed for a typical fill with the new module. These changes do not exceed 15%, and are for the most part well below 5%. As $\dot{m}$ and h_3 from Eq. 3.1 also depend on P_3, different $\dot{Q}_{\text{BS}}$ are obtained.

The cooling powers are compared in Fig. 3.8 for both the arc averages and the family of Q6 quadrupoles. Especially for the high heat load cells in the arcs, the differences due to the inclusion of ΔP are visible but do not exceed 10%. On the contrary, the effect is almost nonexistent for the quadrupoles. This is because the pressure drop depends linearly on the length of the cryogenic cell, and the quadrupole cells are only between 4.8 and 8.6 m long compared to 53 m of the arc half-cells.

It is notable that the logged arc heat loads are different from the recalculated values, even those without pressure drop although they are meant to follow the same algorithm. This is due to a difference concerning how the cells with failing sensors are handled. As noted before, the temperature sensor for T_1 and the pressure sensors for P_1 and P_4 are attached to the supply headers. If one of these sensors fail, it is substituted by the previous one, as these headers cover a whole arc and the temperature and pressure there only changes slowly. These corrections are performed both for the logged and recalculated heat loads. If measured values are missing for another type of sensor, for example T_2 or T_3, the calculations for the corresponding cell is not carried out in the new module. This is currently the case for 16 half-cells in the arcs. While taking the arc averages, these are subsequently ignored. In the code used for the logged data, these sensor values are all set to 0 and the calculation is continued, leading to wrong results for those 16 cells. This in turn distorts the arc averages to the extent visible in Fig. 3.8.

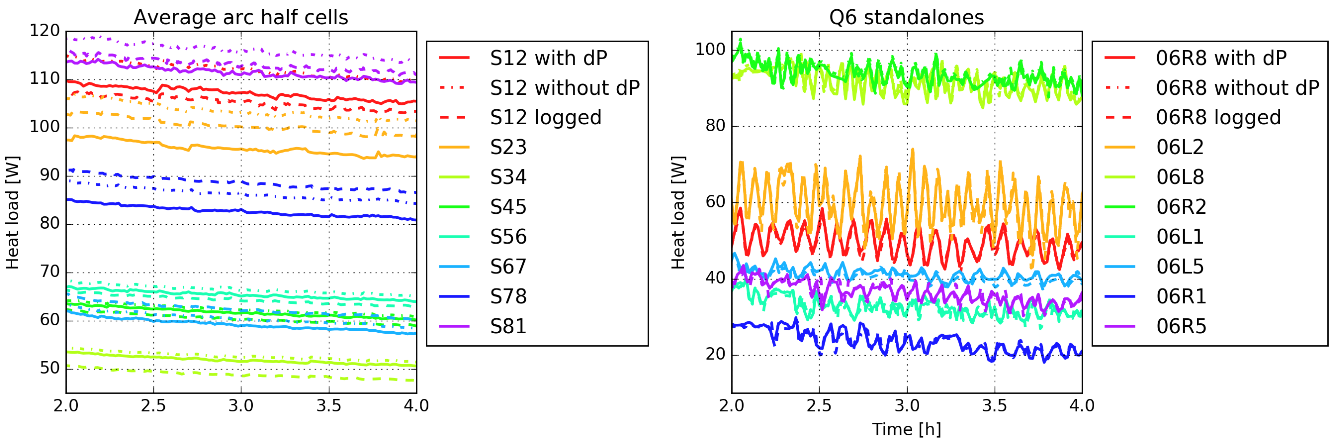

Figure 3.8: The logged and recalculated heat loads for the LHC arcs and Q6 standalone quadrupoles. The lines are not different for the quadrupoles, but show a deviation of up to 10% for the arcs. The quadrupoles do not all have the same lengths. Those in points 2 and 8 (identified by the last character of the label) are 8.6 m long, whereas those in points 1 and 5 are 4.8 m long.

The new module should therefore be used when possible, as it yields more accurate results for the arc averages. Another feature of this module is that it allows for a quick recalculation for all fills of 2015 and 2016 in case the valve configurations $l(u)$ from Eq. (3.7) or $K_{V,max}$, R from Eq. (3.3) are updated, or in case any other changes to the calculations are deemed necessary. For the LHC logging system it is not foreseen to change data once published.

All properties used for the heat load recalculation of the typical fill 5219 (see also Fig. 1.3 are given in the appendix (Sec. 6.2) as histograms. These are formed out of the values from all time steps and all cryogenic cells in the arc. Additionally, only the values at one point in time at high energy are shown, as these are the most relevant ones.

3.3 Specially instrumented cells

Three specially instrumented cells in arc 45 are equipped with additional temperature sensors between the four main magnets, see Fig. 3.9. Their names are 13L5, 33L5 and 13R4 according to the nomenclature that is used for the heat loads on the CERN logging data base[3]. In the last Extended Year-End Technical Stop (EYETS), a dipole had to be exchanged in arc 12 and the whole sector has been warmed up. This made it possible to install additional instrumentation in one of its cells. Once the operation in 2017 has started, this cell will be added to the analysis.

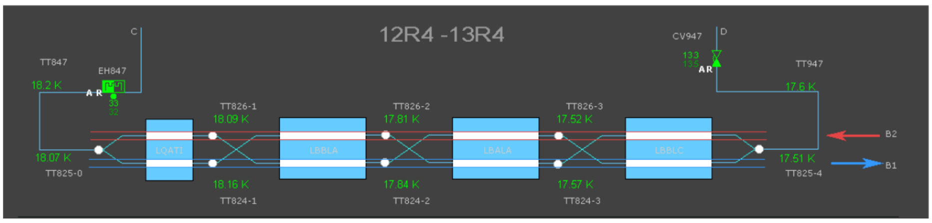

Figure 3.9: Additional temperature sensors between the main magnets are installed in the specially instrumented cells [22].

The heat load calculation for a single magnet is similar to Eq. (3.1), except that the heater and the static sink-in heat loads are not necessary. The mass flow is determined for the whole cell with Eq. (3.6) while neglecting the pressure drop. This could be added to achieve slightly better results. The enthalpy difference is again obtained by interpolating helium property tables.

$$\dot{Q}'_{BS} = \dot{m} \cdot \Delta h \tag{3.17}$$

The pressure drop at each magnet is not taken into account for these cells, as the pressure is unknown at four spots. It would certainly be possible to find an approximation, for example a linear drop from the pressure P_1 to P_3 (following

[3] The pressure and temperature sensors follow a different naming convention, where these cells are called 12R4, 32R4 and 13L5, respectively.

the notation of Fig. 3.3) along the helium line, but this is not currently implemented. P_1 is used at all points instead. Unfortunately a temperature sensor is broken for the cell 33L5, which means that it is not available for analysis.

Figure 3.10 demonstrates the heat loads for a typical fill. Several issues and observations can be immediately identified:

- The recalculated heat loads for the full cell and the sum of the components do not match, the reasons for which are still unclear. Furthermore, the logged values for the cell heat load are very different from the recalculated ones for both cells. These issues need to be followed up together with the cryogenics team.
- The quadrupole for cell 13R4 has negative heat load, this means the helium after this device is measured to be colder than before. This could indicate that there is a heat transfer to the 1.9 K cold mass or that a sensor is wrongly installed or faulty.
- The dipoles, even though identical, yield much different heat loads. This is consistent with the fact that the cells in the LHC show a huge variety in their heat loads. It would be surprising if the dipoles would not show a spread.
- The quadrupole heat loads (after an offset correction) are very low, in the order of a few W/m. The measured heat loads from the Q6 standalone magnets with similar beam screen size are much higher (see Fig. 3.8), a contradiction which is not yet resolved. It could either mean that the measurements are completely wrong for either the family of standalones or for the two special quadrupoles. Alternatively the heat loads could be really different by a large factor that can currently not be explained. This would have a large impact on our understanding of electron cloud. Figure 3.11 demonstrates how the different components would be shared if the dipoles in the arc cells were behaving like the average of the Q6 family.
- The dipole heat load increases significantly during the beam energy ramp, while it barely changes in case of the quadrupoles.

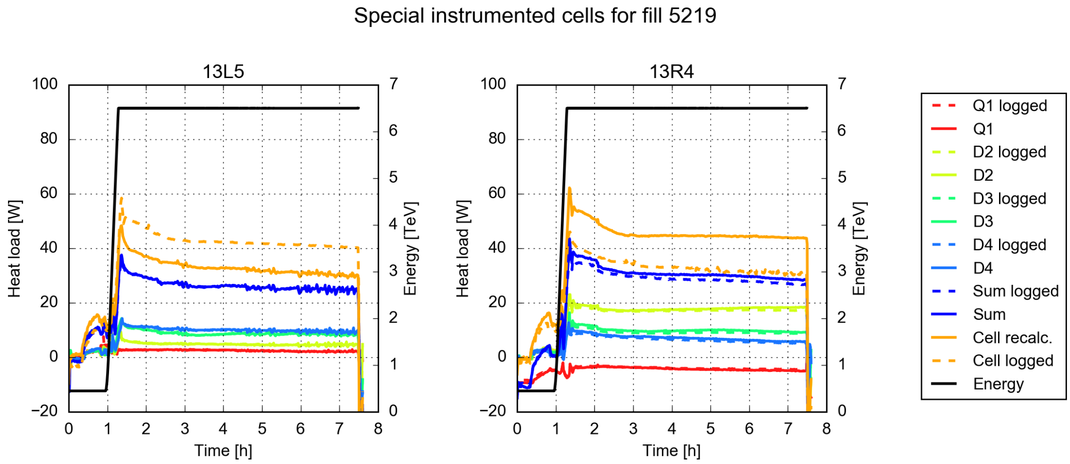

Figure 3.10: For the special instrumented cells, the heat loads of the 4 magnets and the sum are shown. Furthermore the energy of the beam is displayed at the secondary axis. The proton injection takes place in the hour before the energy increase. The recalculated as well as the values form the logging data base are shown. They agree very well for the magnets themselves, whereas they contradict for the full cell when the special sensors are part of the calculation.

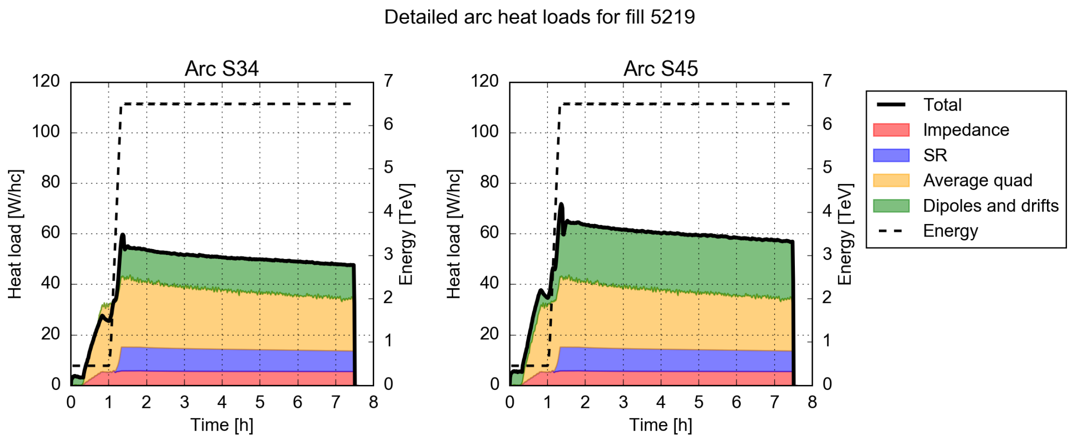

Figure 3.11: Under the speculative assumption that the quadrupoles in the arc cells have the same heat load per m as the standalone Q6 quadrupoles, the different heat load components can be assigned as in these plots. As a consequence, the differences between the arc of the LHC are solely due to the dipoles and interconnections. The same plot for the other arcs is given in Fig. 6.5 in the appendix.

3.4 Estimations of heat loads from other sources

The measured cooling powers that have been subject to this chapter so far include all sources of heat load from the beam, also those that are not related to electron cloud. Therefore, the expected contribution of the resistive wall effect (impedance) and synchrotron radiation is calculated and subtracted. It was implemented as a small python module[4], the coding was done by the author of this report and Giovanni Iadarola.

For the resistive wall effect, classical single bunch formulas as typically done by the CERN impedance team are used [23].

$$P = \frac{1}{C}\Gamma\left(\frac{3}{4}\right)\frac{M}{b}\left(\frac{N_b e}{2\pi}\right)^2\sqrt{\frac{c\rho(T)Z_0}{2}}\sigma_t^{-3/2} \tag{3.18}$$

The following quantities are involved:

- The LHC circumference C.
- The number of bunches M, the particles per bunch N_b and the average bunch length σ_t, which are obtained by Fast Beam Current Transformer (FBCT) measurements and logged. Note that the logged bunch length corresponds to a 2 σ diameter.
- The beam screen half height $b = 18.4$ mm.
- The fundamental constants e, c and Z_0.
- The surface resistivity of the beam screen ρ, where a beam screen temperature of 20 K is assumed.

The surface resistivity of the beam screen is the temperature dependent surface resistivity of copper $\rho_{\mathrm{Cu}}(T)$ (see Fig. 3.12) with corrections from the magneto-resistive wall effect ($\Delta\rho(B)$) and the stainless steel beam screen weld (f_w).

$$\rho(B) = f_\mathrm{w}\left(\rho_{\mathrm{Cu}}(20\ \mathrm{K}) + \Delta\rho(B)\right) \tag{3.19}$$

$$\Delta\rho(B) = 10^{-2.69}\left(B\,\frac{\rho_{\mathrm{Cu}}(273\ \mathrm{K})}{\rho_{\mathrm{Cu}}(4\ \mathrm{K})}\right)^{1.055} \tag{3.20}$$

$$f_\mathrm{w} = \sqrt{\frac{\rho_{\mathrm{SS}}(20\ \mathrm{K})}{\rho_{\mathrm{Cu}}(20\ \mathrm{K})}\cdot\frac{l_\mathrm{w}}{2\pi b}} \tag{3.21}$$

In the last equation, ρ_{SS} is the surface resistivity of stainless steel, which is taken as $6{\cdot}10^{-7}$ Ωm at 20 K, and l_w is the length of the weld, which takes up a fraction of 1/60 of the total beam screen circumference.

[4] Available under `https://github.com/giadarol/HeatLoadCalculators`

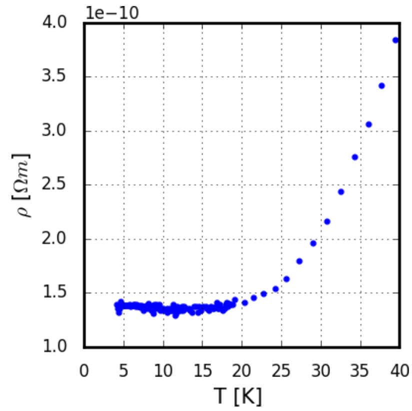

Figure 3.12: The data from which the surface resistivity of copper $\rho_{\mathrm{Cu}}(T)$ is obtained through interpolation. It does not change by much over the temperatures that occur at the beam screen. These range between 4 and 20 K [24].

The synchrotron radiation effect is easier to estimate. Since it is a closed system, the full power of the emitted radiation has to be absorbed by the cooling circuit. The formula for the energy loss per turn is found in standard text books such as [25].

$$\Delta E = \frac{e^2}{3\epsilon_0} \frac{1}{(mc^2)^4} \frac{E^4}{R} \tag{3.22}$$

Here, E is the energy and N the total number of particles of the beam, while m is the proton mass and ϵ_0 the vacuum permittivity. The radius R is the bending radius of the dipoles, not to be confused with the average machine radius. To obtain the power, this has to be scaled with the revolution frequency f_{Rev} and the number of particles in the beam N.

$$P = N \cdot f_{\mathrm{Rev}} \cdot \Delta E \tag{3.23}$$

The synchrotron radiation is only taken into account for the arcs since strong bending magnets are not installed elsewhere. It is assumed to be distributed uniformly across the cryogenic cells.

For a typical fill, the contributions of the modelled heat loads are shown in Fig. 1.3. The synchrotron radiation heat load has a larger effect than the impedance heat load.

3.5 Validation and error analysis

The error analysis of the heat load measurements is being investigated by cryogenics team. The current status was presented in December 2016 [22]. These efforts are quite relevant for this report, so they are in part briefly described here. Some additional data analysis is reported to validate the results of the modelled contributions of synchrotron radiation and the resistive wall effect.

Figure 3.13 demonstrates the error propagation of two parameters in the calculation from Sec. 3.2 on the resulting heat loads. These are the rangeability R and the maximum gas flow trough the valve, $K_{\mathrm{V,max}}$. The possible relative errors of up to 60% are quite alarming at first, but this is merely an arithmetic example of what would happen if these parameters were wrong by up to 30% each.

On the other hand there have also been dedicated measurements to validate the heat loads. These are briefly described in Fig. 3.14 and have been performed for the arcs 12, 23 and 78 in 2016. The bottom line is that even though individual cells can deviate by up to 30% for a typical fill, there is no systematic error towards lower or higher heat loads and the average arc heat loads are deemed accurate by 3%. However this only holds for the typical valve openings as they are encountered in operations.

The combination of synchrotron radiation and impedance heat loads can be compared with the measured cooling power for fills where no significant electron clouds are expected. The best candidate for these are fills with 100 ns bunch spacing, these have last been performed in 2015. Figure 3.15 shows the cell by cell heat load at collision energy as well as the corresponding model heat loads. The average arc heat loads are in very good agreement with the expectations to the extent of less than 1 W. This is true for all arcs. Other plots are shown in the appendix of this report: Fig. 6.6 and 6.7. This being said, large varieties and outliers between cells are present. It is unclear whether these are due to measurement artifacts, for example because there is a thermal coupling with reservoirs at lower or higher temperatures.

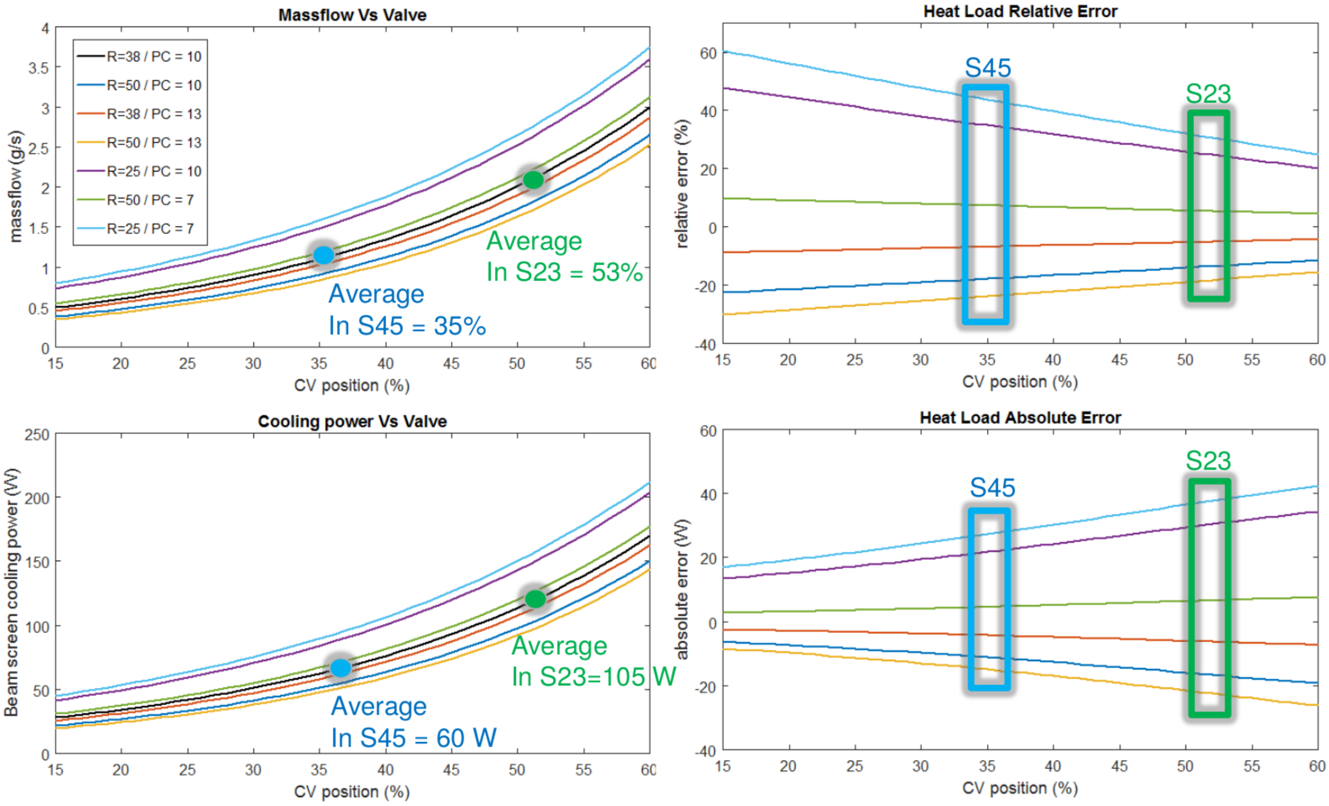

Figure 3.13: The effect of wrong parameters on the calculation presented in Sec. 3.2 is analyzed here. The valve rangeability R from Eq. 3.3 and the pre-constraint PC (the latter being the subtracted term from Eq. 3.7) are being varied by 30% to find out the effect on the resulting heat load. R is defined in the configuration files and assumed as 38 for most cells, while PC is hardcoded as 0.1. The CV position on the x axis corresponds to u from Eq. 3.7. The two plots on the left demonstrate by how much the mass flow and heat loads change for various combinations of R and PC. The blue and green dots indicate the average valve positions of sectors 45 and 23, a low and a high heat load sector (as in Fig. 1.3). On the right, the possible stretch of the results is shown. The impact is larger on low heat loads cells in relative terms, while the opposite is true in absolute terms.
This is a slide taken from a presentation, where a member of the cryogenics team described the ongoing efforts to validate and improve the heat load measurements [22].

Another point to make is the importance of subtracting the offset for low heat load fills. Fig. 3.16 shows how these are found for the 100 ns fill that was featured above. In case this step is omitted, the resulting histograms for 2 arcs can be compared in Figs. 6.7 and 6.8. Not only is the spread between the cells much larger than before, but also do the modelled and measured cooling powers differ by a large amount.

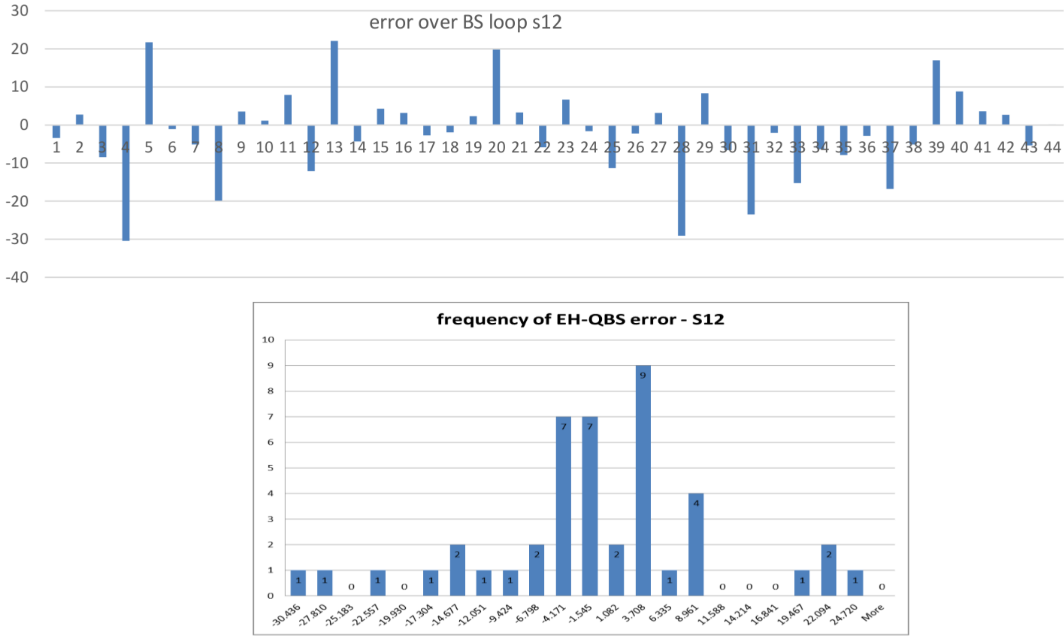

Figure 3.14: The measured beam screen temperatures and valve openings from a typical fill have been reproduced with the electrical heater that is installed in every cell (see Fig. 3.3). The power of the heater is then compared with the measured heat loads, and the deviation is shown in the top plot in relative terms for all cells in the arc 12, which requires among the highest cooling power in the LHC. The bottom plot shows a histogram of these deviations. For the most part, these are rather evenly distributed towards both sides. There are 3 cells with a deviation between -20 and -30% but also 4 cells between +20 and +25%, for example. These plots origin from [22], as well.

Figure 3.15: The cell by cell heat loads for a fill with 100 ns bunch spacing are shown here. As the electron cloud is not expected to be relevant for this fill, the heat loads should match the combination of synchrotron radiation and impedance.

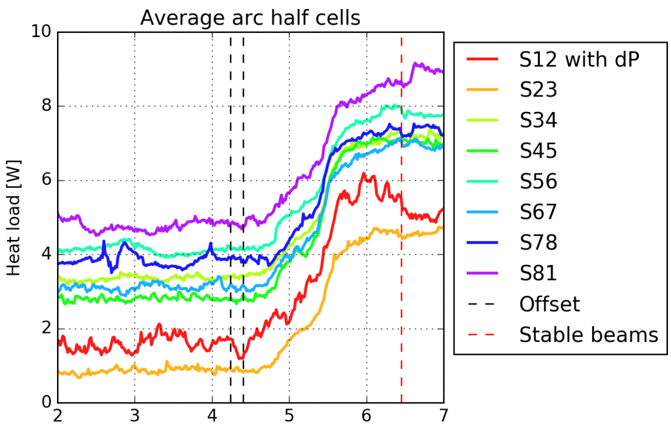

Figure 3.16: This plot corresponds to the same fill as Fig. 3.15 and is meant to explain how the heat load offsets are found. The second vertical black line marks the begin of proton injection. The average of the quarter hour between the two black lines defines the offset that is subtracted from the cooling power for the whole fill. The red line indicates the moment where "stable beams" are declared.

The data from the LHC instrumentation, including the parts relevant for electron cloud studies, are available in the CERN logging database. Although this data can be accessed easily, the comparison of beam or heat load properties between more than just a few fills used to be tedious. One reason is that the data for a fill is stored together in a file which had to be read as a whole even when only a small part of it was needed. To allow for a better data analysis, a tool was developed that greatly increases our data analysis[1]. This tool itself is presented in this section. Later on, an important process called beam induced mitigation of the electron cloud is first explained and then evaluated for the LHC during 2015 and 2016. Furthermore, the results of a Machine Development session dedicated to investigating the effect of different bunch intensities on heat loads are presented. These allow an estimation of the scaling of electron-cloud effects for intensities up to $1.1 \cdot 10^{11}$ particles per bunch.

4.1 Data dictionary

The main output of the implemented module is a nested python dictionary with self-descriptive keys. It contains data for 282 fills, those that have reached the stable beams status in 2015 and 2016. For each of them, the following properties are stored:

	Once or	multiple times per fill	Note
Fill number	x		e.g. 5219
Filling pattern	x		e.g. '25ns_2220b_2208_1940_2036_96bpi_24inj'
Top energy	x		
Bunches per injection	x		Bunches per injection from the SPS
Heat load offset	x		For all cells and the arc averages
Sum of fill heat load	x		For all cells and the arc averages
Heat loads		x	For all cells and the arc averages
Heat load from Imp./SR		x	For both beams
Time points		x	In seconds after 1970 (Unix time)
Average bunch length		x	For both beams, from FBCT
Bunch length standard deviation		x	For both beams
Number of bunches		x	For both beams, from FBCT
Total intensity		x	For both beams, from BCT

Some of the parameters need further clarification.

- The recalculated heat loads and model heat loads from Sec. 3.2 and 3.4 are used.
- The heat load offset is the average of the recalculated heat load between the proton injection ("Injection Physics Beam") and 15 minutes before, this means before there is beam in the machine, see also Sec. 3.5.
- The integral of the fill heat load allows us to estimate the amount of electron bombardment must have taken place. Later on this quantity is compared with the decrease in heat load.
- The bunch length is stored as the diameter of a 2 σ beam, it therefore corresponds to the 4 σ beam length.
- The filling pattern is an identifier for the arrangement of filled and empty bunch slots for a given fill.
- FBCT is the acronym for Fast Beam Current Transformer.

The time points for the parameters that are stored several times per fill is listed here, they correspond to what is also shown in Fig. 1.3.

- The beginning of the fill.
- The beginning of the proton injection, which corresponds to the "Injection Physics Beam" mode.
- The beginning of the energy ramp.
- The end of the beam size squeeze process.

[1] This python module is available online under `https://github.com/pdijksta/hl_dicts`

- The declaration of stable beams.
- Every hour afterwards for up to 24 hours.

The basic properties of the fills that are stored in the heat load dictionary are shown in Fig. 4.1.

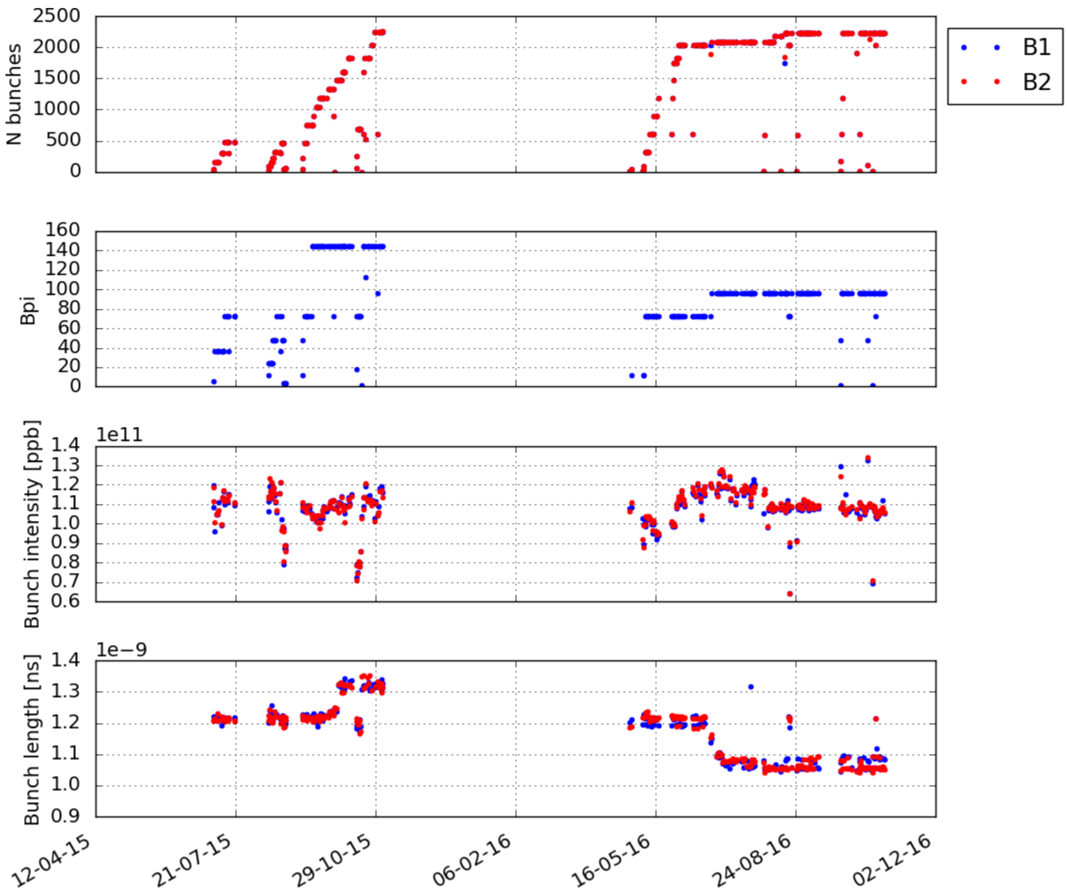

Figure 4.1: Basic beam properties are shown for all fills that are contained in the dictionary. The number of bunches for the two beams is identical for almost all fills, the red and blue dots overlap. Bpi is short for bunches per injection, a measure which corresponds to the length of the trains.

4.2 Electron cloud mitigated scrubbing in 2015 and 2016

The secondary electron emission of surfaces that are exposed to electron irradiation tends to decrease gradually. This effect is called "scrubbing" or "SEY conditioning". In the case of electron clouds, it means that they can be self-mitigating. Dedicated measurements have taken place for example at the SPS, these show a rapid decrease of electron emission after only a few hours. This process however slows down considerably as it can be seen in Fig. 4.3, where much longer time intervals are necessary to decrease the SEY curve by roughly the same amount.

In the case of the LHC, there are no measurement devices installed to observe electron clouds directly. The analysis from this section is focused on the how the arc heat loads have changed during the scrubbing that occurred during the proton physics fills in 2015 and 2016. Fills with less than 800 bunches per beam were excluded. For all following plots, the heat load is shown at the end of the squeeze process. The model heat load from impedance and synchrotron radiation has not been subtracted. Figure 4.3 first displays the heat loads as they have been measured. Because of much less bunches for the earliest fills of 2015, this plot alone would be misleading as the heat loads are rising by a great amount. A second plot, where the heat load is normalized to the total beam intensity, reveals that the electron cloud effects are strongly decreasing for the whole year of 2015. This trend continues in 2016, albeit at a much slower rate.

While looking at the third plot, it turns out that the differences between the arcs has only barely decreased in 2016. Apparently there is a cause of heat load generated by a source that scales with the beam intensity and is not affected by electron-cloud mitigated scrubbing.

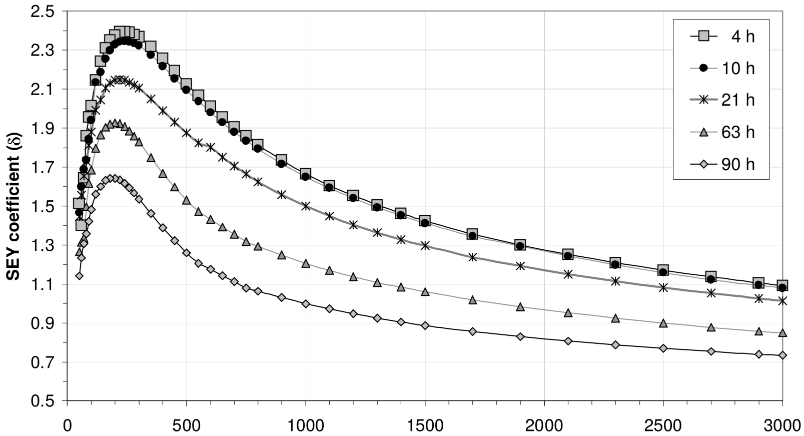

Figure 4.2: A copper sample has been exposed to a beam similar to the ones at LHC. The measured secondary emission yield changes with the duration of exposure. This data has been taken in the SPS [26].

Figure 4.4 shows a very similar plot, where the half-cells in the arcs are not grouped by the arc they are located in, but according to the cooling power they required for the last ten fills of 2016. Every of these "deciles" corresponds to the average of about 37 cells, which are relatively similar to each other. It becomes clear that the difference between these cells in normalized heat load traces back to at least the beginning of operations in 2015.

The next figure (Fig. 4.5) then relates the measured heat loads to the sum of the heat loads from all previous fills. Here, also the dipoles from the specially instrumented cells and the Q6 quadrupoles are shown. For the arcs and for the deciles, it is clear that the cells that correspond to the high heat load curves do not condition faster even though their measured heat load is far higher. It appears to be some kind of offset that they cannot overcome. The reasons for this are yet unclear and will be subject to further studies.

The data for the quadrupoles is very different, but has not been thoroughly studied yet. Only two of the quadrupoles show a notable change in heat loads. It might be that the others have already arrived at their final plateau before 2015. This needs a more careful analysis, however. The data for the dipoles from the special cells on the other hand is compatible with the findings from the arc averages and deciles.

The question came up whether this difference between the cells mentioned before could be caused by an impedance effect. From the side of the impedance team this is regarded as unlikely, but is being further investigated [27, 28]. The next section of this report shows that the electron cloud generated heat loads do scale linearly with intensity in the current regime.

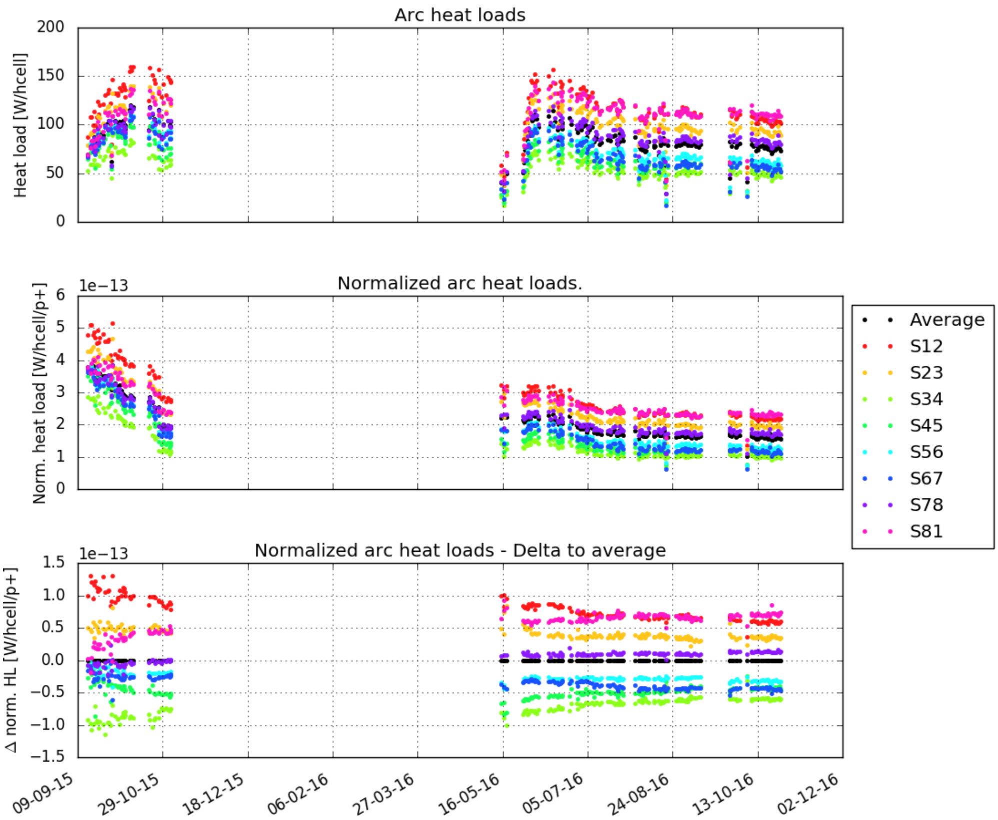

Figure 4.3: The measured average arc cooling powers are plotted in absolute terms in the top plot, while they are normalized with the beam intensity in the middle plot. The bottom shows the differences in normalized heat load with respect to the average value.

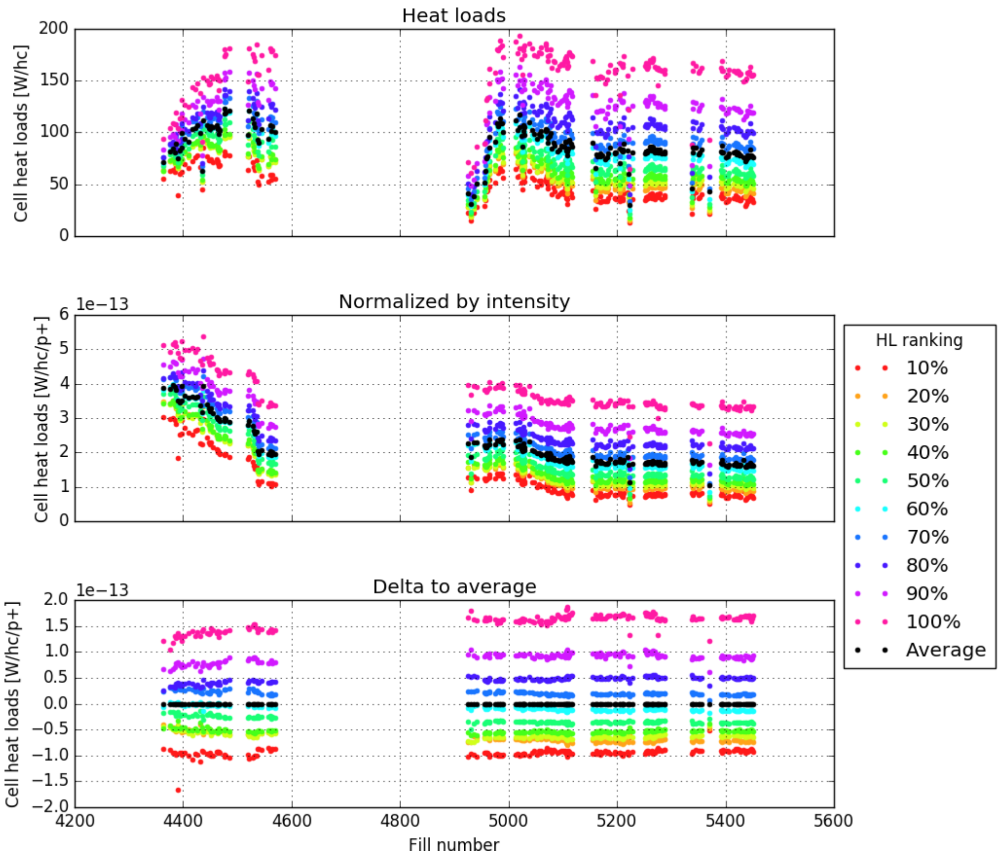

Figure 4.4: Instead of being grouped into arcs, all the cryogenic cells are ranked with respect to the cooling power they required in the last ten fills of 2016. This plot demonstrates that this hierarchy has been present from early on. Relative to each other, the differences in normalized heat load barely changes.

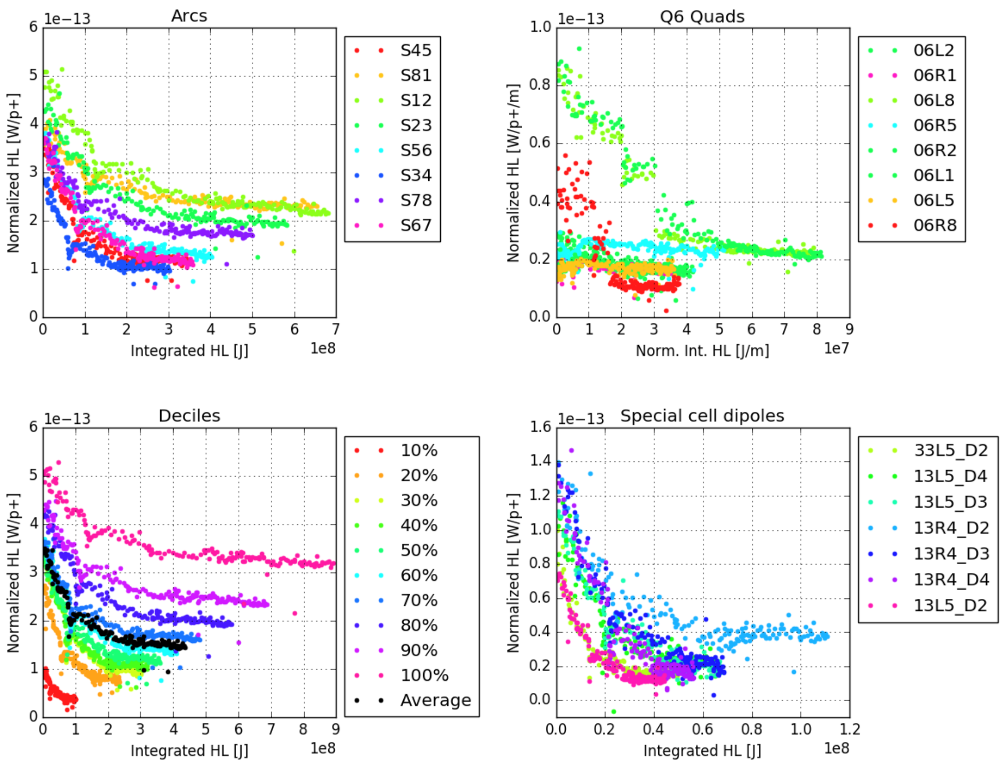

Figure 4.5: The normalized heat loads are plotted against the sum of the heat loads of previous fills since 2015. The special cell dipoles and the Q6 standalone quadrupoles are shown on the right. The plot for the latter is normalized also by the length of the respective quadrupole.

In August 2016, three fills have been performed during an Machine Development session, with the purpose of investigating the dependence of e-cloud build-up on the bunch intensity of the circulating beam. These three fills (5219, 5222 and 5223) were identical in terms of filling schemes and RF settings, but possessed different injected bunch intensities (respectively $1.11 \cdot 10^{11}$, $0.9 \cdot 10^{11}$ and $0.7 \cdot 10^{11}$ p/bunch).

Figure. 4.6 (left) shows the bunch length at high energy against the bunch intensity. The initial value of the bunch length was about 1.2 ns for all fills. The right plot shows the evolution of the heat load at high energy plotted against the bunch intensity. It is notable that for each sector the measurements from the three fills seem not to lie on the same line. This is due to the fact that the bunch length at the end of each fill is significantly shorter than at the beginning of the following one, which increases the electron cloud effects.

In Fig. 4.7, the heat load measured for the same bunch length of 1.15 ns is compared, as indicated by the black lines in Fig 4.6. The uncertainties for this plot consist of 5% of what has been measured, in addition to the offset (see Sec. 3.5), but should be considered as preliminary. In contact with the cryogenics team, a final stance on how the uncertainties should be specified will be found and used for the work leading up to the Master's Thesis.

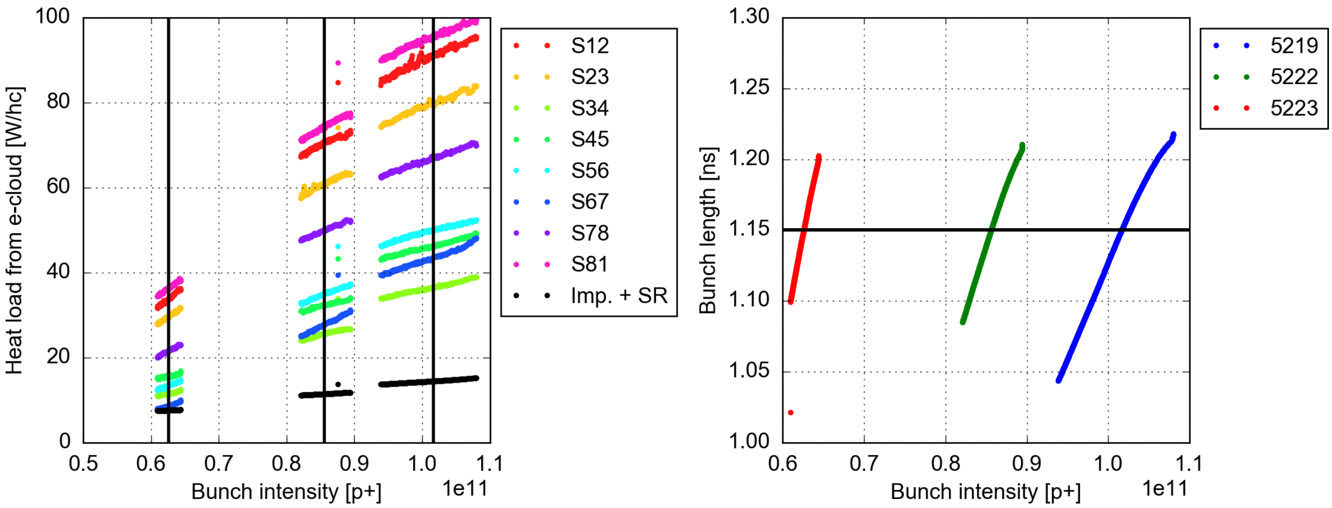

Figure 4.6: The Heat loads as a function of the bunch intensity for the three test fills with different initial bunch intensity are shown on the left. The estimated heat loads from the beam screen impedance and from synchrotron radiation are subtracted and indicated in black.

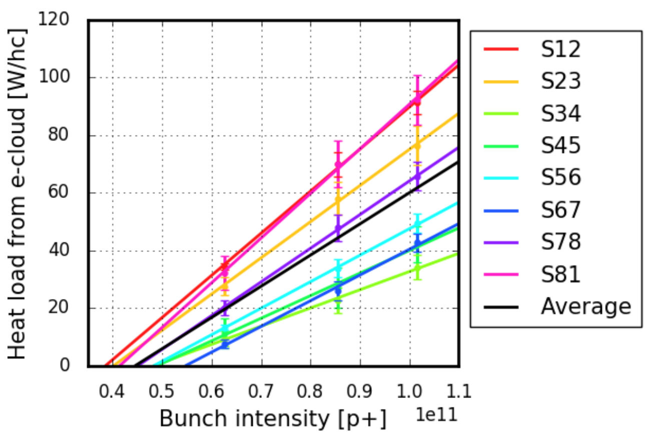

Figure 4.7: The heat loads from the figure above are shown together with a linear fit.

The report gave a description of the work that has been performed in order to improve the understanding of electron cloud effects at the LHC. This final part briefly recaps these steps and points out what should be done in the months to come. While major parts concerning data analysis have been finished, emphasis will be put especially on performing buildup simulations.

5.1 Buildup simulations

The buildup simulations for electron clouds rely on the secondary emission model, which defines how electrons interact with the chamber. The dependence of this model on various input parameters has been studied, see Sec. 2.3. As a next step, simulations based on measured beam parameters have to be performed.

A suitable fill is presented in Fig. 5.1, which shows the total intensity, the average arc heat loads and the bunch length. This data changed significantly over the duration of the fill, and should in principle be reproduced with simulations. The vertical bars indicate interesting points in time along the fill. Simulations using the measured bunch lengths and intensities at these points have already been performed, but not been analyzed to date.

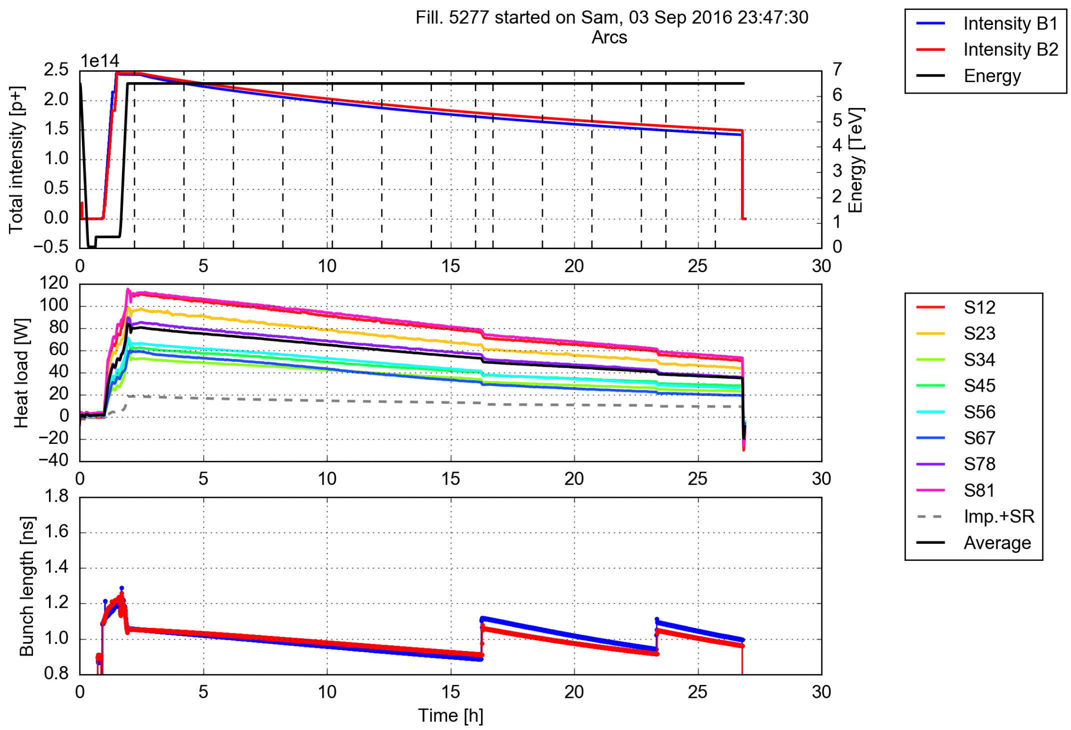

Figure 5.1: Simulations based on this fill will be analyzed to show in which way the modelled electron cloud effects depend on beam parameters such as intensity and bunch length. On two occasions, the bunch length has been increased which is reflected in a sudden change of heat load.

Another necessary step is the formation of a more accurate model of the cryogenic cells in the LHC arcs. The simulations presented earlier in this report covered dipoles and quadrupoles. This has to be extended to the magnet interconnections, which take up about 7 out of 53 m of a cryogenic cell. This space is filled with drift space and correction magnets, some of them of higher order such as sextupoles and octupoles. As such multipoles have not been simulated yet within PyECLOUD, the code will be extended in this aspect.

Furthermore, photoemission by synchrotron radiation will be used as a seeding mechanism for buildup simulations, in place of an initial distribution of primary electrons in the chamber. Measurements taken at CERN with the materials used in the LHC are available, these describe the photon reflectivity and electron yield per impinging electron [29].

Because the cooling power required for the beam screens of the cryogenic cells is the most important indication for electron cloud effects at the LHC, a large part of this report has been dedicated on data analysis and improvement. A module for recalculating the heat loads for all fills in 2015 and 2016 has been written, see chapter 3.2. It includes the effect of the pressure drop, especially relevant for cells with high heat loads. Furthermore, the average arc heat loads are now correctly calculated, ignoring the cells that do not have a full set of functioning sensors. Additionally, specially instrumented cells that allow for a heat load calculation of individual magnets in the arcs have been analyzed (Sec. 3.3). Heat loads from sources other than electron cloud are synchrotron radiation and impedance. These contributions have been calculated and a good agreement is found with the measured cooling powers for fills with very low electron cloud effects (Sec. 3.4 and 3.5). The module for the cooling power recalculation has to be finalized in coordination with the cryogenics team. This will put an uncertainty estimation for these heat loads in place, so they can be compared to simulation results.

The heat load dictionary presented in Sec. 4 has been very helpful in estimating the electron cloud mitigated scrubbing for the previous two years. It was shown that there are several types of cryogenic cells, according to the amount of heat loads measured. It cannot be expected that the differences between these cells decrease as the scrubbing continues in 2017 and beyond. This could have implications for the HL-LHC upgrade. Furthermore, heat loads from three fills with different bunch intensities have been analyzed, in order to find out about the dependence in the current regime of operations at the LHC (see Sec. 4.3).

The LHC will continue its operation in the following months. In the beginning, the heat loads are expected to be higher than towards the end of 2016. This is because the surface properties usually reset to a certain extend and lead to higher secondary emission yields when they are exposed to the beam again after a pause of several months. Therefore, dedicated "Scrubbing runs" [30] will be performed. These are fills which are designed to create strong electron cloud effects, so that the surfaces quickly recondition and allow operation with the nominal beam parameters. The data that is going to be accumulated will be analyzed, especially for the arc that has been warmed up to exchange a dipole in the last shutdown. Because the beam screens in this arc have been exposed to air, it will be very interesting to see the change in heat loads.

6.1 Heat load calculation template

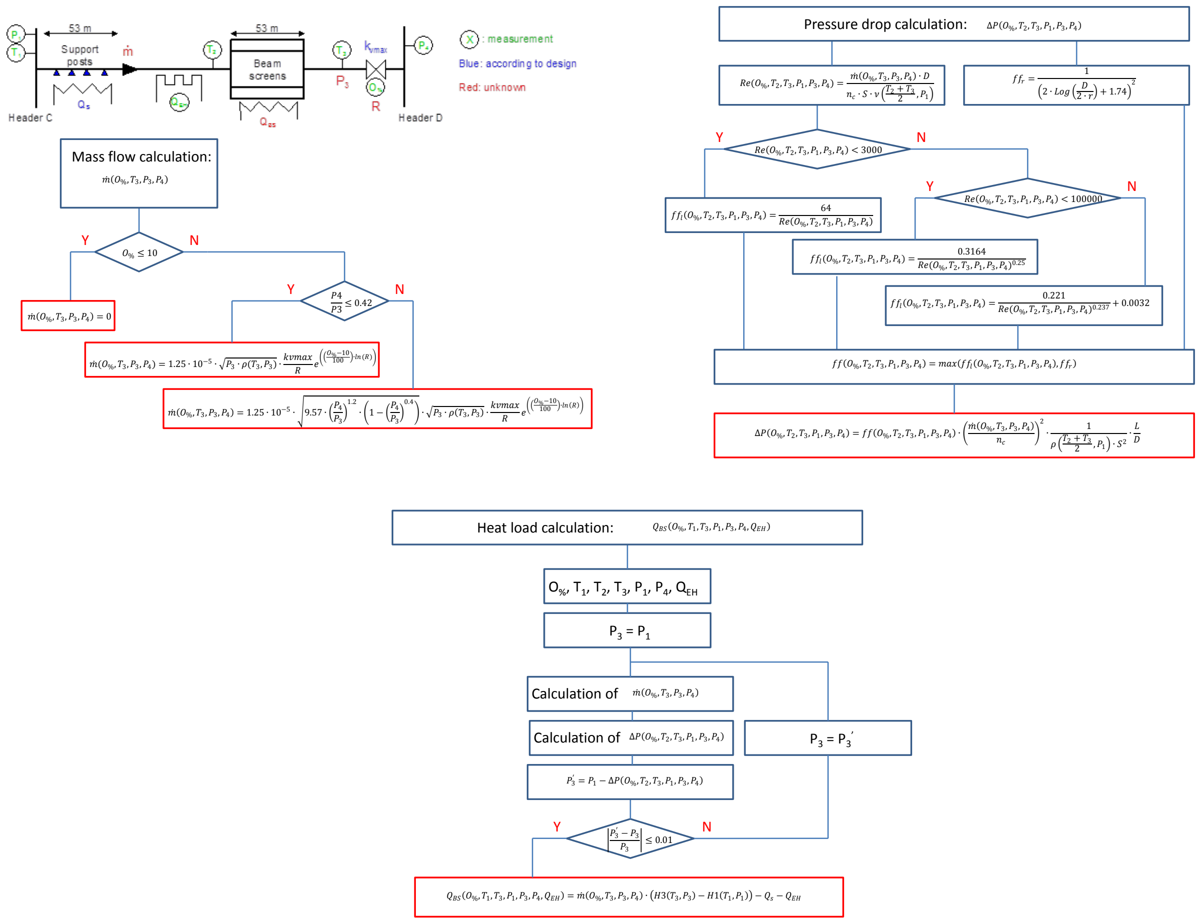

Figure 6.1: The CERN cryogenics team based the heat load computation on these slides by Laurent Tavian [31].

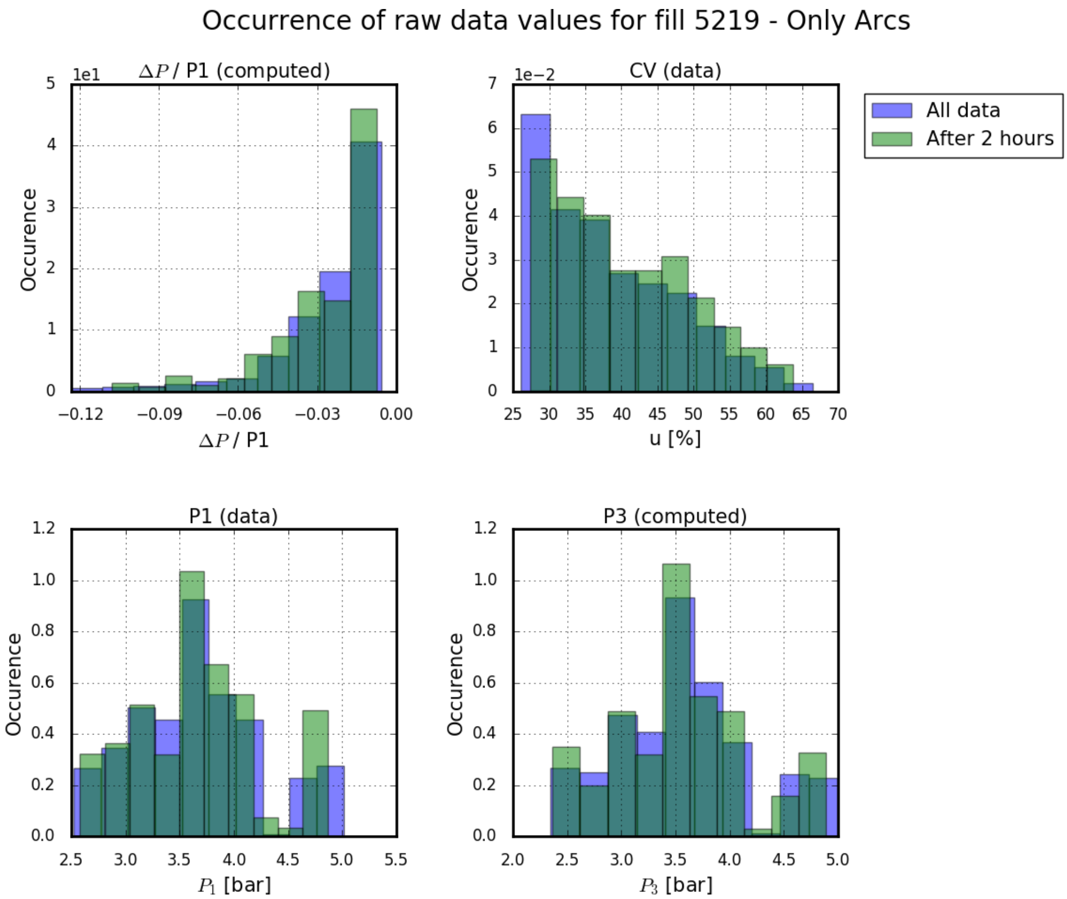

Figure 6.2: How often do certain values relevant for the heat load calculations appear for a typical fill? The data for the blue histograms consists of all points (every 60 s) from the heat load calculation of the arc cells of a typical fill. The green histogram shows only the values for one time point 2 h after the begin of the fill, and is therefore a subset of the blue one. If (data) is appended to the title of a plot, it means that is is a value directly from the logging data base. Otherwise it has been an intermediate or final step of the heat load calculation.

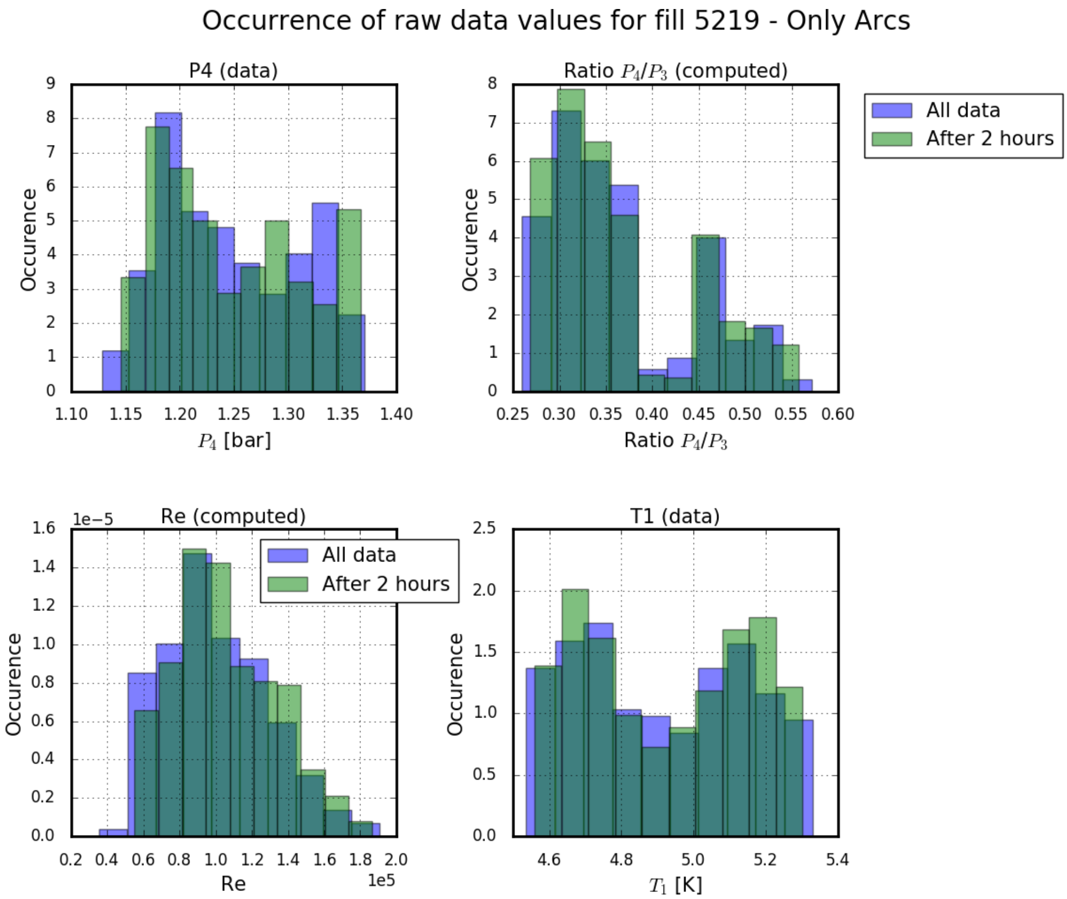

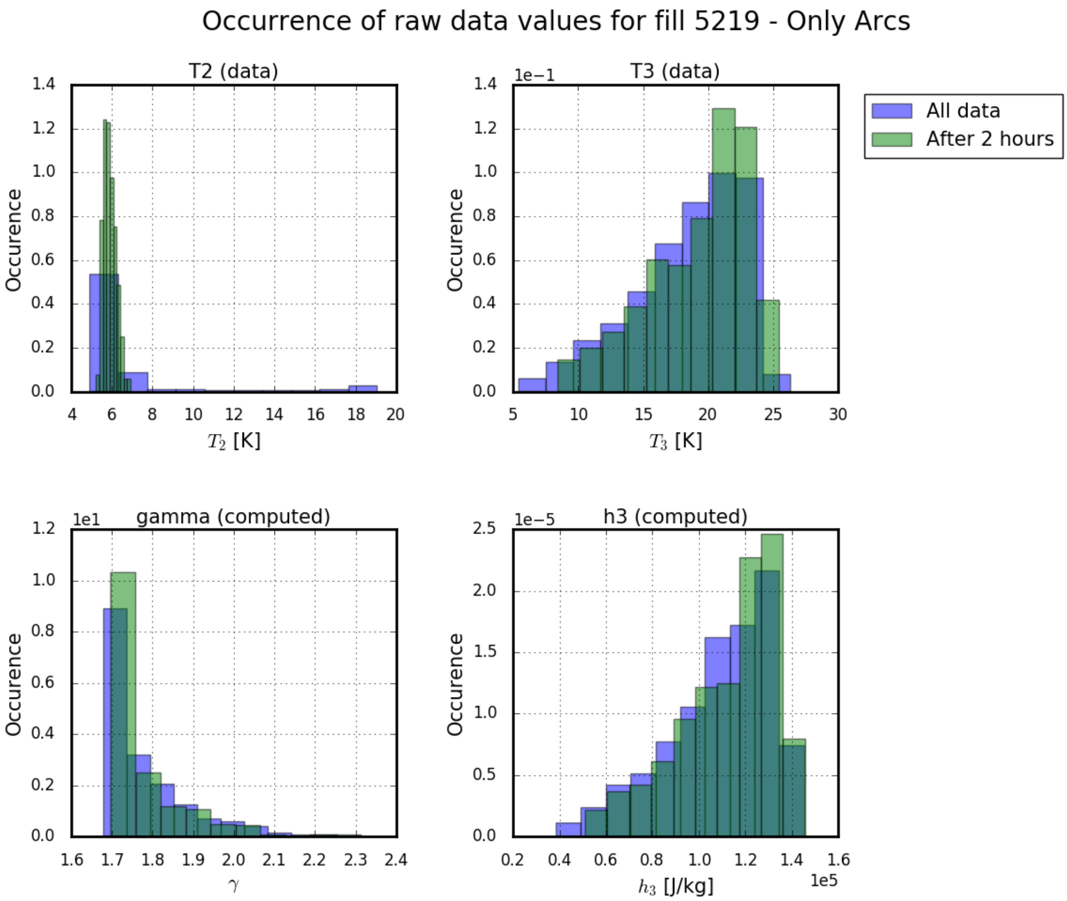

Figure 6.3: See Fig. 6.2.

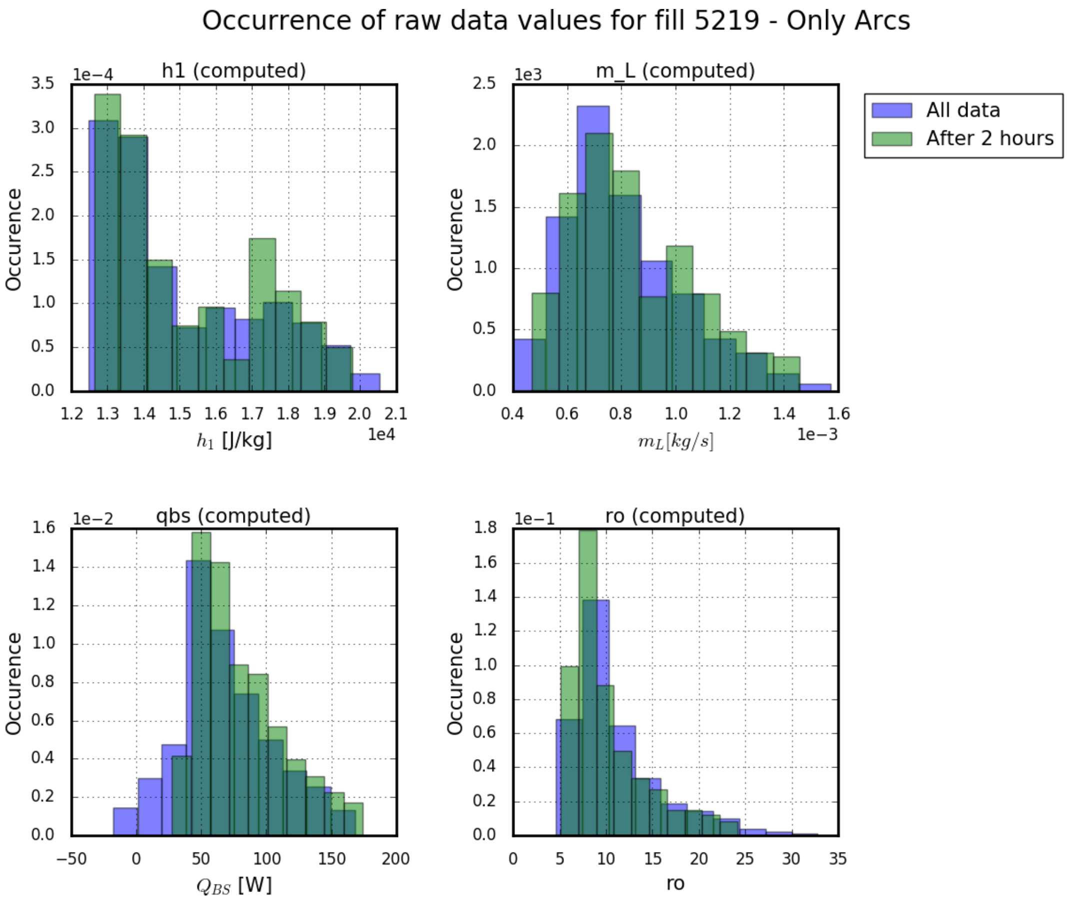

Figure 6.4: See Fig. 6.2.

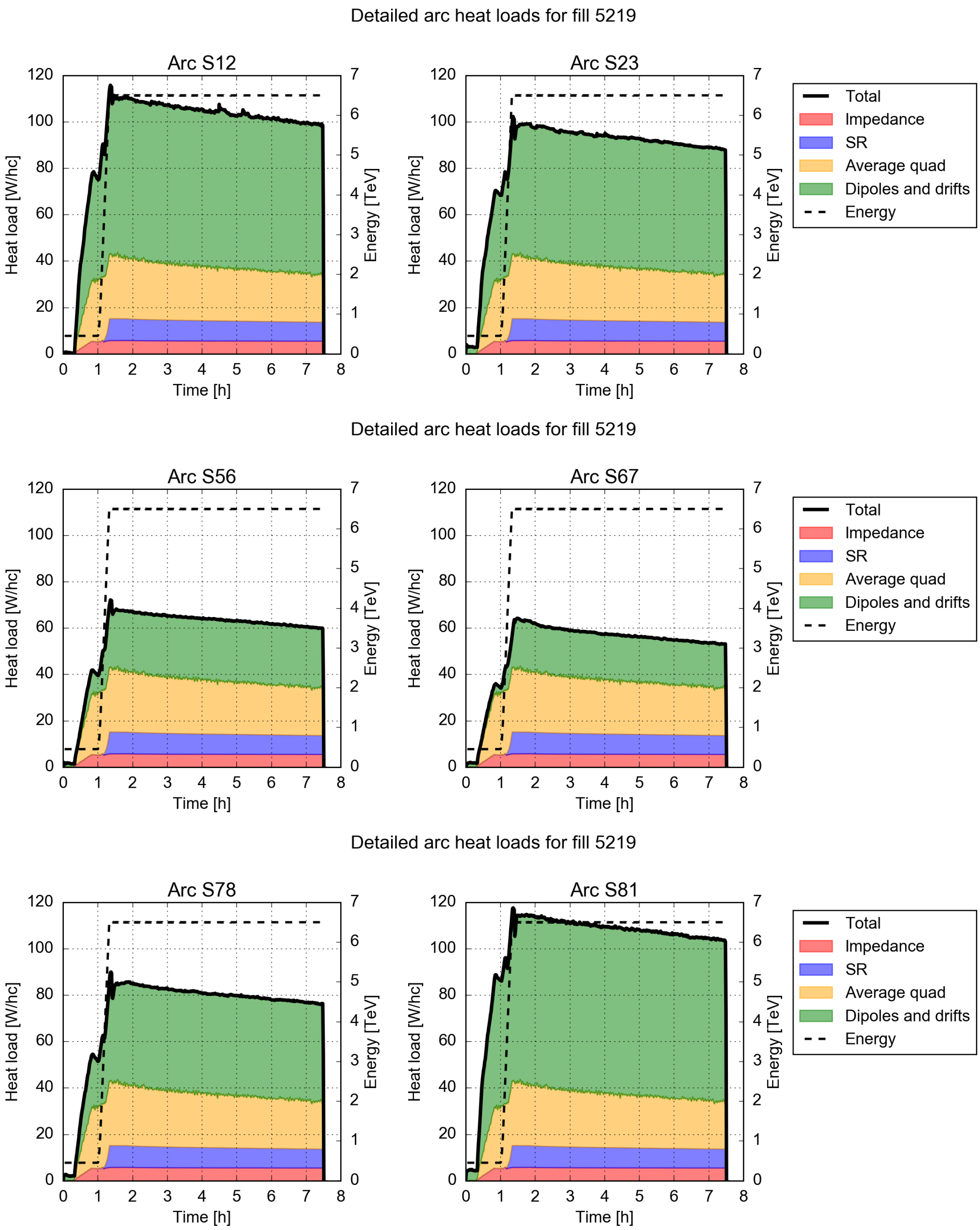

Figure 6.5: If the 3.1 m long quadrupoles in the arc cells were causing the same heat load per meter as the standalone Q6 quadrupoles, how would the measured heat loads be shared for an average cell in each arc? The corresponding plots for the remaining two arcs are given in Fig. 3.11.

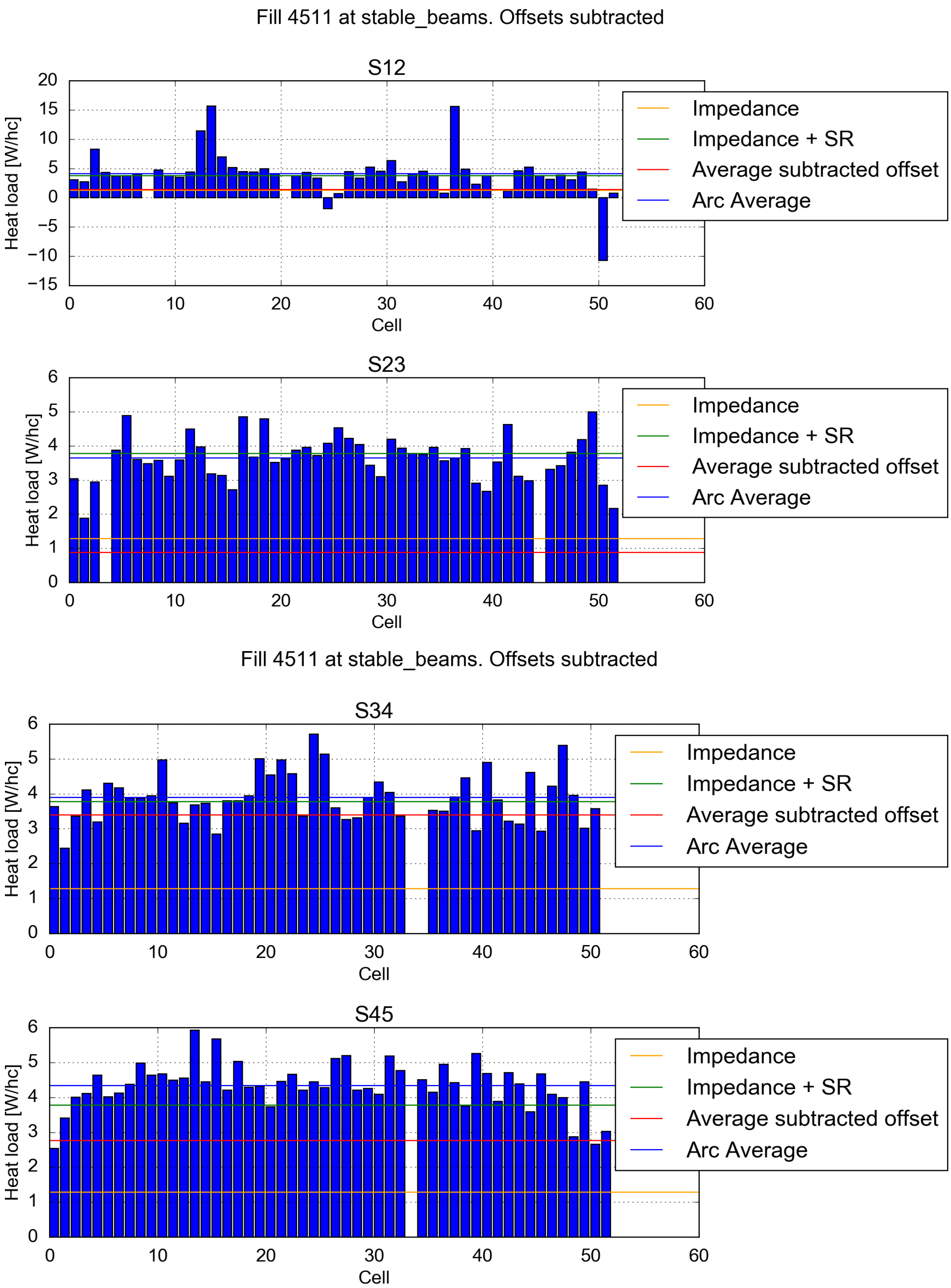

Figure 6.6: This figure corresponds to Fig. 3.15. For a fill where no substantial electron cloud effects are expected, the calculated and expected cooling powers are compared.

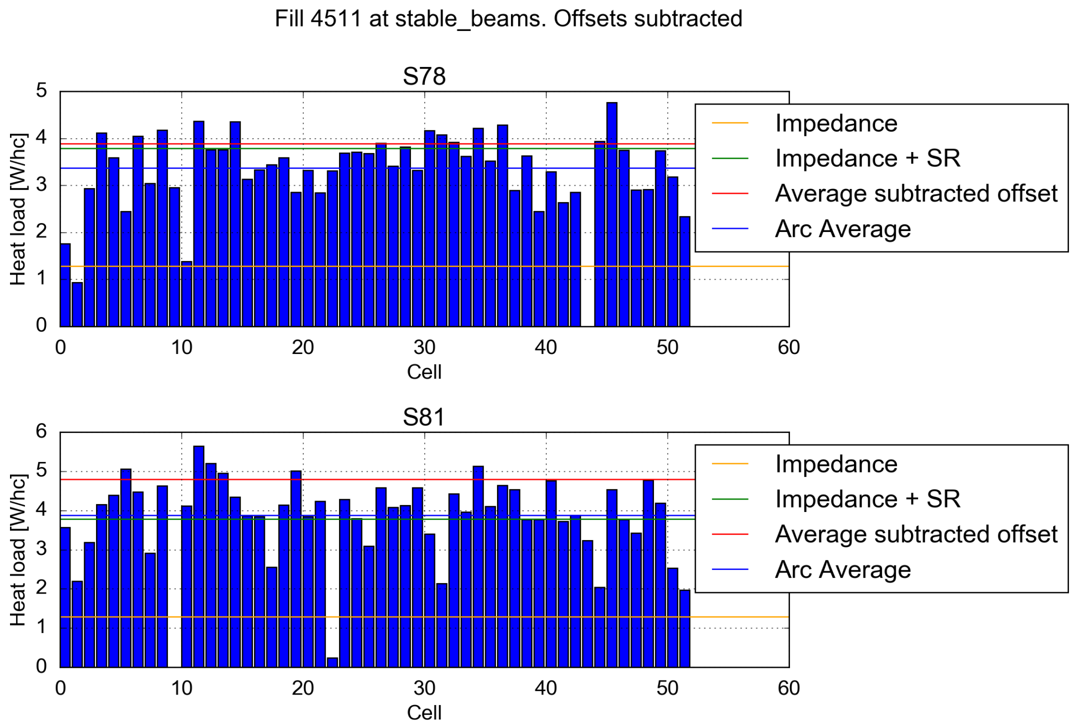

Figure 6.7: This figure corresponds to Fig. 3.15.

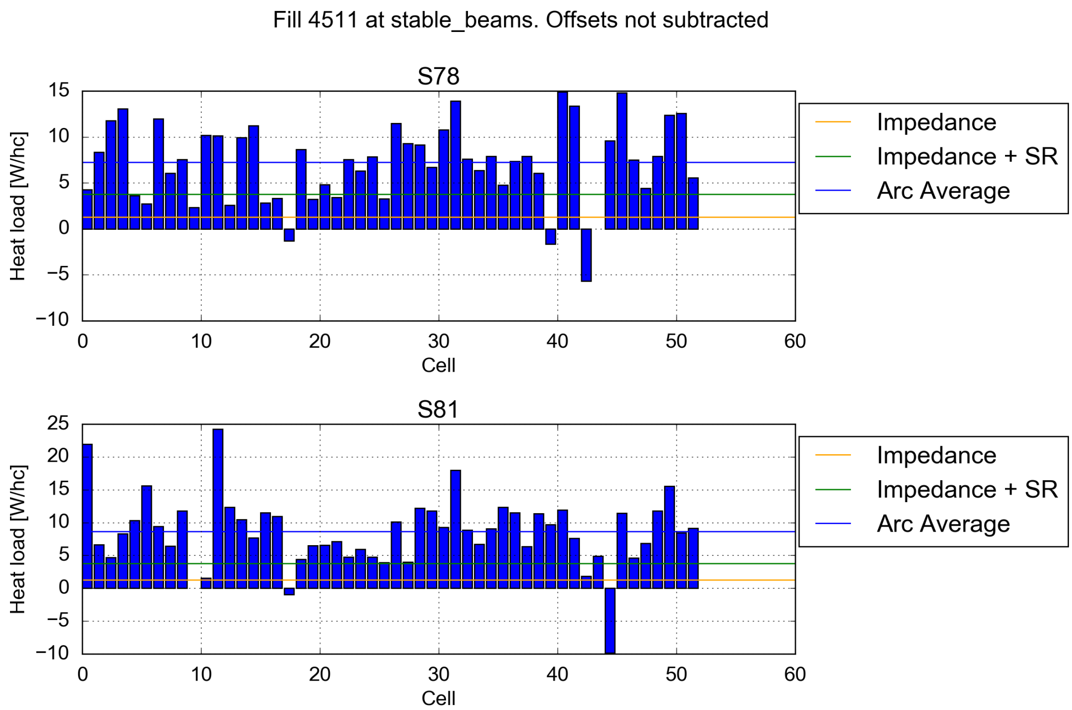

Figure 6.8: This figure corresponds to Fig. 6.7, however the offsets have not been subtracted for the individual cells. Consequently, the measured and expected cooling powers do not match to a similar extend, but differ by several Watts.

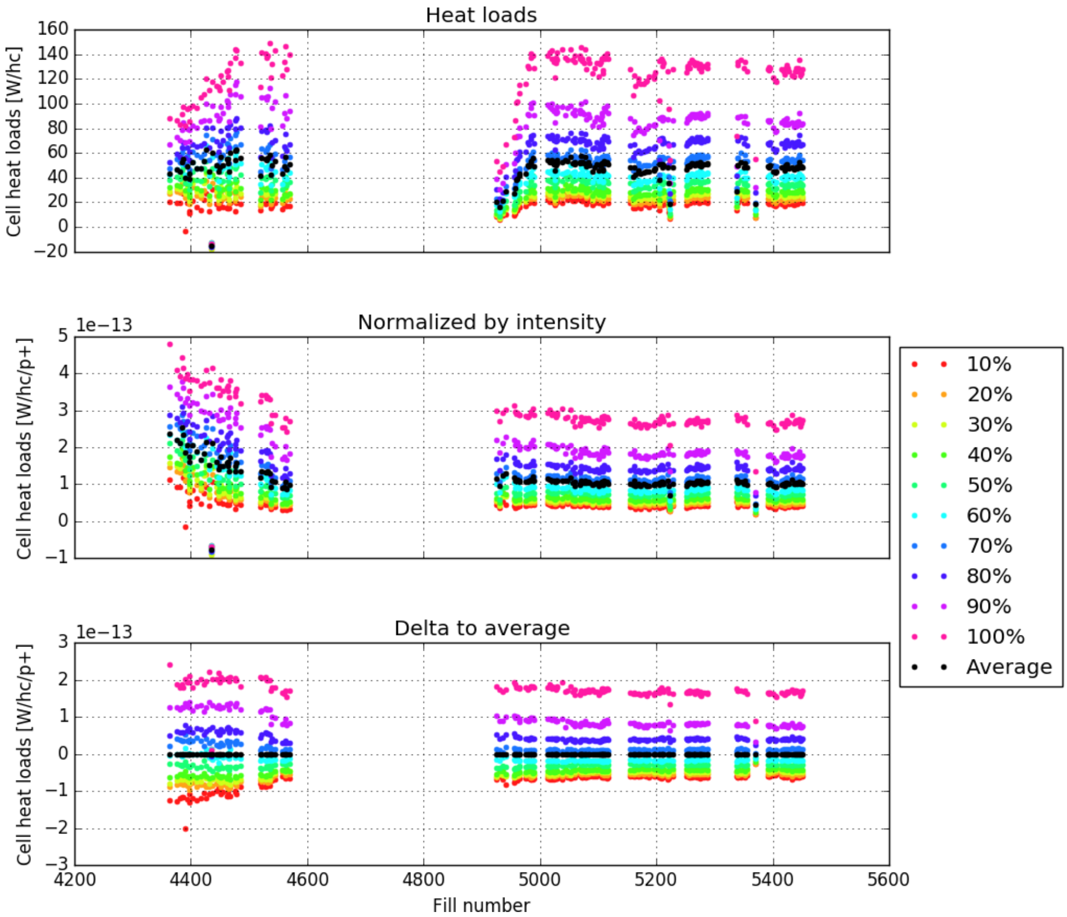

Figure 6.9: These plots show that the differences between the cells as discussed in Sec. 4.2 are already present at injection energy.

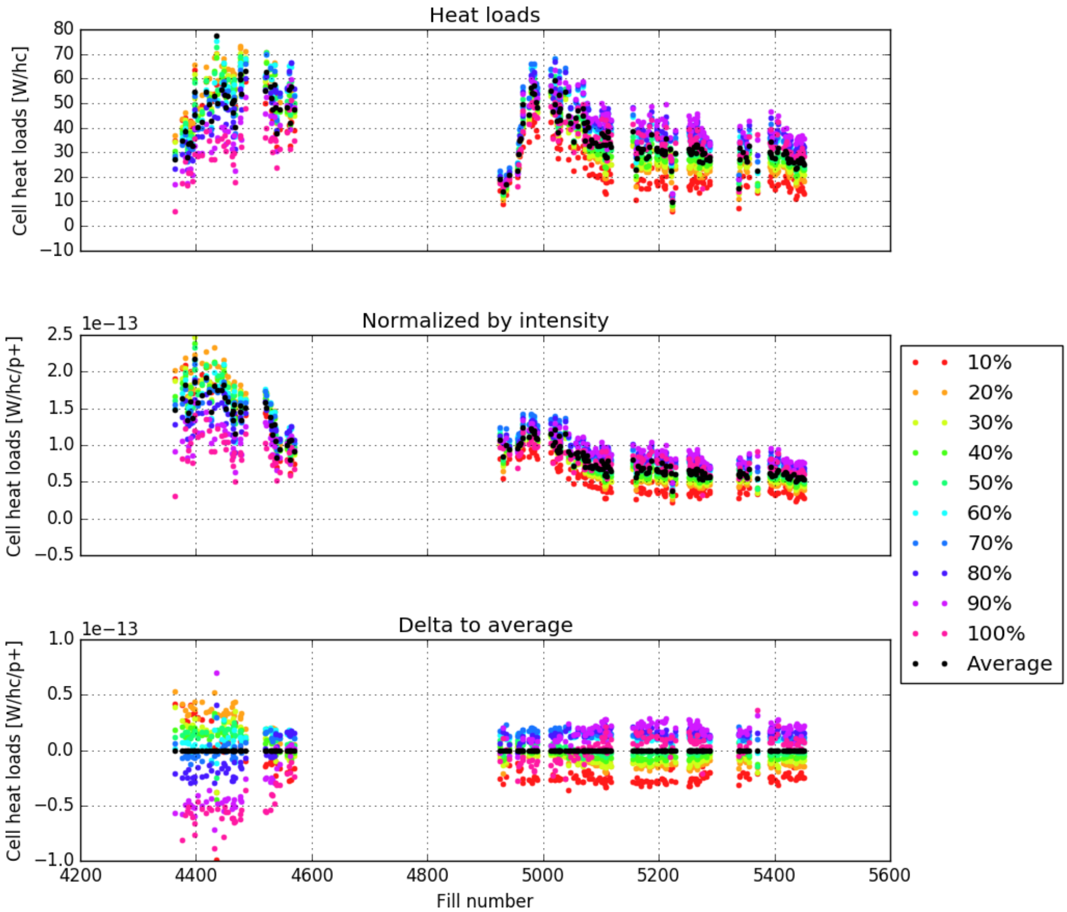

Figure 6.10: These plots show the difference in heat loads before and after the energy ramp up from 450 GeV to 6.5 TeV. The clear distinction between the groups of cells does not hold any longer.

[1] G. Aad et al., Combined Measurement of the Higgs Boson Mass in pp Collisions at $\sqrt{s} = 7$ and 8 TeV with the ATLAS and CMS Experiments, Physical Review Letters 114 (19).

[2] F. Bordry, Chamonix 2016 conclusions, presentation at Chamonix workshop 2016.

[3] CERN, Accélérateurs du CERN, `http://project-integration-accelerateurs.web.cern.ch` (figure).

[4] G. Apollinari, I. B. Alonso, O. Brüning, M. Lamont, L. Rossi, High-Luminosity Large Hadron Collider (HL-LHC), CERN, Geneva, 2015, Preliminary Design Report.

[5] G. Iadarola, Electron Cloud studies for CERN particle accelerators and simulation code development, Ph.D. thesis, University of Naples Federico II (2014).

[6] K. Ohmi, L. Mether, D. Schulte, F. Zimmermann, Study of Electron Cloud Instabilities in FCC-hh, in: Proceedings, 6th International Particle Accelerator Conference (IPAC 2015): Richmond, Virginia, USA, May 3-8, 2015, 2015.

[7] B. Henrist, N. Hilleret, M. Jiménez, C. Scheuerlein, M. Taborelli and G. Vorlaufer, Secondary electron emission data for the simulation of electron cloud, in: ECLOUD'02: Mini-workshop on electron-cloud simulations for proton and positron beams, CERN, Geneva, Switzerland, 15-18 Apr 2001: Proceedings, 2002.

[8] V. Baglin, I. Collins, B. Henrist, N. Hilleret and G. Vorlaufer, A Summary of main experimental results concerning the secondary electron emission of copper, LHC Project Report 472.

[9] R. Cimino, I. R. Collins, M. A. Furman, M. Pivi, F. Ruggiero, G. Rumolo, F. Zimmermann, Can low-energy electrons affect high-energy physics accelerators?, Phys. Rev. Lett. 93.

[10] R. Cimino, I. Collins, Vacuum chamber surface electronic properties influencing electron cloud phenomena, LHC Project Report 669.

[11] M. T. A. Kuzucan, H. Neupert, H. Störi, Secondary Electron Yield on Cryogenic Surfaces as a Function of Physisorbed Gases, in: Proceedings of the IPAC11 International Particle Accelerator Conference, San Sebastian, Spain, 2011.

[12] R. Cimino, L. A. Gonzalez, R. Larciprete, A. Di Gaspare, G. Iadarola, G. Rumolo, Detailed investigation of the low energy secondary electron yield of technical cu and its relevance for the lhc, Phys. Rev. ST Accel. Beams 18.

[13] Proceedings of the ECLOUD '12 Workshop on Electron-Cloud Effects, CERN, Geneva, 2013, comments: 39 lectures, 286 pages, published as CERN Yellow Report https://cds.cern.ch/record/1529710?ln=en.

[14] E. Hatchadourian, P. Lebrun, L. Tavian, Supercritical Helium Cooling of the LHC Beam Screens, LHC Project Report 212.

[15] E. Ödlund, Virtual Instrumentation: Introduction of virtual flow meters in the LHC cryogenics control system, Ph.D. thesis, Linköping University (2007).

[16] O. S. Brüning, P. Collier, P. Lebrun, S. Myers, R. Ostojic, J. Poole, P. Proudlock, LHC Design Report, CERN, Geneva, 2004.

[17] K. Brodzinski, L. Tavian, First Measurements of Beam-Induced Heating on the LHC Cryogenic System, Tech. Rep. CERN-ATS-2013-009, CERN, Geneva (Jan 2013).

[18] Cryodata INC, Users Guide to HEPAK, Louisville, Colorado, 1999.

[19] B. Bradu, Private message, 01.02.2017.

[20] Steven W. Van Sciver, Helium Cryogenics, 2nd Edition, Springer, New York, 2012.

[21] Wikipedia, Reynolds number, `https://en.wikipedia.org/wiki/Reynolds_number`, accessed 13.02.2017 (2017).

[22] B. Bradu, LHC Beam Screen Heat Loads, `https://indico.cern.ch/event/592369/`, presentation at Electron Cloud Meeting 36, 12.12.2016 (figure).

[23] E. Métral, Beam Screen Issues, Presentation at EuCARD - AccNet mini workshop on a "High Energy LHC" (2010).

[24] G. Iadarola, E. Metral, G. Rumolo, Beam induced heat loads on the beam-screens of the twin-bore magnets in the IRs of the HL-LHC, Tech. rep., CERN, Geneva, internal CERN note (Sep 2016).

[25] K. Wille, Physik der Teilchenbeschleuniger und Synchrotronstrahlungsquellen, 2nd Edition, Teubner, Stuttgart, 1996, English title: The Physics of Particle Accelerators: An Introduction.

[26] J. M. Jimenez, G. Arduini, P. Collier, G. Ferioli, B. Henrist, N. Hilleret, L. Jensen, K. Weiss, F. Zimmermann, Electron cloud with LHC-type beams in the SPS: A review of three years of measurements, in: ECLOUD'02: Mini-workshop on electron-cloud simulations for proton and positron beams, CERN, Geneva, Switzerland, 15-18 Apr 2001: Proceedings, 2002.

[27] G. Iadarola, P. Dijkstal, LHC Heat Loads: Observations with different bunch spacings, Presentation at HSC section meeting https://indico.cern.ch/event/612111/ 20.02.2017.

[28] B. Salvant, Beam spectrum computations, Presentation at HSC section meeting https://indico.cern.ch/event/612111/ 20.02.2017.

[29] V. Baglin, I. R. Collins, O. Gröbner, Photoelectron Yield and Photon Reflectivity from Candidate LHC Vacuum Chamber Materials with Implications to the Vacuum Chamber Design (LHC-Project-Report-206. CERN-LHC-Project-Report-206).

[30] H. Bartosik, G. Iadarola, K. Li, L. Mether, A. Romano, G. Rumolo, M. Schenk, Beam dynamics observation of the 2015 high intensity scrubbing runs at the CERN SPS, in: Proceedings of the IPAC16 International Particle Accelerator Conference, Busan, Korea, 2016.

[31] B. Bradu, Private message, 10.02.2017.